ICESat (GLAS) Science Processing Software Document Series

The GLAS Algorithm Theoretical Basis Document for Precision Orbit Determination (POD)

Hyung Jin Rim, S. P. Yoon, and Bob E. Schutz

March 2013

NASA STI Program ... in Profile

Since its founding, NASA has been dedicated to the advancement of aeronautics and space science. The NASA scientific and technical information (STI) program plays a key part in helping NASA maintain this important role.

The NASA STI program operates under the auspices of the Agency Chief Information Officer. It collects, organizes, provides for archiving, and disseminates NASA's STI. The NASA STI program provides access to the NASA Aeronautics and Space Database and its public interface, the NASA Technical Report Server, thus providing one of the largest collections of aeronautical and space science STI in the world. Results are published in both non-NASA channels and by NASA in the NASA STI Report Series, which includes the following report types:

- TECHNICAL PUBLICATION. Reports of completed research or a major significant phase of research that present the results of NASA Programs and include extensive data or theoretical analysis. Includes compilations of significant scientific and technical data and information deemed to be of continuing reference value. NASA counterpart of peer-reviewed formal professional papers but has less stringent limitations on manuscript length and extent of graphic presentations.

- TECHNICAL MEMORANDUM. Scientific and technical findings that are preliminary or of specialized interest, e.g., quick release reports, working papers, and bibliographies that contain minimal annotation. Does not contain extensive analysis.

- CONTRACTOR REPORT. Scientific and technical findings by NASA-sponsored contractors and grantees.

- CONFERENCE PUBLICATION. Collected papers from scientific and technical conferences, symposia, seminars, or other meetings sponsored or co-sponsored by NASA.

- SPECIAL PUBLICATION. Scientific, technical, or historical information from NASA programs, projects, and missions, often concerned with subjects having substantial public interest.

- TECHNICAL TRANSLATION. English-language translations of foreign scientific and technical material pertinent to NASA's mission.

Specialized services also include organizing and publishing research results, distributing specialized research announcements and feeds, providing help desk and personal search support, and enabling data exchange services. For more information about the NASA STI program, see the following:

- Access the NASA STI program home page at http://www.sti.nasa.gov

- E-mail your question via the Internet to help@sti.nasa.gov

- Fax your question to the NASA STI Help Desk at 443-757-5803

- Phone the NASA STI Help Desk at 443-757-5802

- Write to:

  NASA STI Help Desk
  NASA Center for AeroSpace Information
  7115 Standard Drive
  Hanover, MD 21076-1320

ICESat (GLAS) Science Processing Software Document Series

The GLAS Algorithm Theoretical Basis Document for Precision Orbit Determination (POD)

Hyung Jin Rim
Center for Space Research, The University of Texas at Austin

S. P. Yoon
Center for Space Research, The University of Texas at Austin

Bob E. Schutz
Center for Space Research, The University of Texas at Austin

March 2013

TABLE OF CONTENTS

ii

1.0   INTRODUCTION

1.1   Background

The EOS ICESat mission is scheduled for launch on July 2001. Three major science objectives of this mission are: (1) to measure long-term changes in the volumes (and mass) of the Greenland and Antarctic ice sheets with sufficient accuracy to assess their impact on global sea level, and to measure seasonal and interannual variability of the surface elevation, (2) to make topographic measurements of the Earth's land surface to provide ground control points for topographic maps and digital elevation models, and to detect topographic change, and (3) to measure the vertical structure and magnitude of cloud and aerosol parameters that are important for the radiative balance of the Earth-atmosphere system, and directly measure the height of atmospheric transition layers. The spacecraft features the Geoscience Laser Altimeter System (GLAS), which will measure a laser pulse round-trip time of flight, emitted by the spacecraft and reflected by the ice sheet or land surface. This laser altimeter measurement provides height of the GLAS instrument above the ice sheet. The geocentric height of the ice surface is computed by differencing the altimeter measurement from the satellite height, which is computed from Precision Orbit Determination (POD) using satellite tracking data.

To achieve the science objectives, especially for measuring the ice-sheet topography, the position of the GLAS instrument should be known with an accuracy of 5 and 20 cm in radial and horizontal components, respectively. This knowledge will be acquired from data collected by the on-board GPS receiver and ground GPS receivers and from the ground-based satellite laser ranging (SLR) data. GPS data will

be the primary tracking data for the ICESat/GLAS POD, and SLR data will be used for POD validation.

1.2   The POD Problem

The problem of determining an accurate ephemeris for an orbiting satellite involves estimating the position and velocity of the satellite from a sequence of observations, which are a function of the satellite position, and velocity. This is accomplished by integrating the equations of motion for the satellite from a reference epoch to each observation time to produce predicted observations. The predicted observations are differenced from the true observations to produce observation residuals. The components of the satellite state (satellite position and velocity and the estimated force and measurement model parameters) at the reference epoch are then adjusted to minimize the observation residuals in a least square sense. Thus, to solve the orbit determination problem, one needs the equations of motion describing the forces acting on the satellite, the observation-state relationship describing the relation of the observed parameters to the satellite state, and the least squares estimation algorithm used to obtain the estimate.

1.3   GPS-based POD

Since the earliest concepts, which led to the development of the Global Positioning System (GPS), it has been recognized that this system could be used for tracking low Earth orbiting satellites. Compared to the conventional ground-based tracking systems, such as the satellite laser ranging or Doppler systems, the GPS

tracking system has the advantage of providing continuous tracking of a low satellite with high precision observations of the satellite motion with a minimal number of ground stations. The GPS tracking system for POD consists of a GPS flight receiver, a global GPS tracking network, and a ground data processing and control system.

1.3.1   Historical Perspective

The GPS tracking system has demonstrated its capability of providing high precision POD products through the GPS flight experiment on TOPEX/Poseidon (T/P) [*Melbourne et al.*, 1994]. Precise orbits computed from the GPS tracking data [*Yunck et al.*, 1994; *Christensen et al.*, 1994; *Schutz et al.*, 1994] are estimated to have a radial orbit accuracy comparable to or better than the precise orbit ephemerides (POE) computed from the combined SLR and DORIS tracking data [*Tapley et al.*, 1994] on T/P. When the reduced-dynamic orbit determination technique was employed with the GPS data, which includes process noise accelerations that absorb dynamic model errors after fixing all dynamic model parameters from the fully dynamic approach, there is evidence to suggest that the radial orbit accuracy is better than 3 cm [*Bertiger et al.*, 1994].

While GPS receivers have flown on missions prior to T/P, such as Landsat-4 and -5, and Extreme Ultraviolet Explorer, the receivers were single frequency and had high level of ionospheric effects relative to the dual frequency T/P receiver. In addition, the satellite altitudes were 700 km and 500 km, respectively, and the geopotential models available for POD, as they are today, had large errors for

such altitudes. As a result, sub-decimeter radial orbit accuracy could not be achieved for these satellites.

Through the GPS flight experiment on T/P several important lessons on GPS-based POD have been learned. Those include: 1) GPS Demonstration Receiver (GPS/DR) on T/P provides continuous, global, and high precision GPS observable. 2) GPS-based POD produces T/P radial orbit accuracy similar or better than SLR/DORIS. 3) Gravity tuning using GPS measurement was effective [*Tapley et al.*, 1996]. 4) Both reduced-dynamic technique and dynamic approach with extensive parameterization have been shown to reduce orbit errors caused by mismodeling of satellite forces.

1.3.2 GPS-based POD Strategies

Several different POD approaches are available using GPS measurements. Those include the kinematic or geometric approach, dynamic approach, and the reduced-dynamic approach.

The kinematic or geometric approach does not require the description of the dynamics except for possible interpolation between solution points for the user satellite, and the orbit solution is referenced to the phase center of the on-board GPS antenna instead of the satellite's center of mass. *Yunck and Wu* [1986] proposed a geometric method that uses the continuous record of satellite position changes obtained from the GPS carrier phase to smooth the position measurements made with pseudorange. This approach assumes the accessibility of P-codes at both the L1 and L2 frequencies. *Byun* [1998] developed a kinematic orbit determination algorithm

using double- and triple-differenced GPS carrier phase measurements. Kinematic solutions are more sensitive to geometrical factors, such as the direction of the GPS satellites and the GPS orbit accuracy, and they require the resolution of phase ambiguities.

The dynamic orbit determination approach [*Tapley*, 1973] requires precise models of the forces acting on user satellite. This technique has been applied to many successful satellite missions and has become the mainstream POD approach. Dynamic model errors are the limiting factor for this technique, such as the geopotential model errors and atmospheric drag model errors, depending on the dynamic environment of the user satellite. With the continuous, global, and high precision GPS tracking data, dynamic model parameters, such as geopotential parameters, can be tuned effectively to reduce the effects of dynamic model error in the context of dynamic approach. The dense tracking data also allows for the frequent estimation of empirical parameters to absorb the effects of unmodeled or mismodeled dynamic error.

The reduced-dynamic approach [*Wu et al*., 1987] uses both geometric and dynamic information and weighs their relative strength by solving for local geometric position corrections using a process noise model to absorb dynamic model errors.

Note that the adopted approach for ICESat/GLAS POD is the dynamic approach with gravity tuning and the reduced-dynamic solutions will be used for validation of the dynamic solutions.

1.4   Outline

This document describes the algorithms for the precise orbit determination (POD) of ICESat/GLAS. Chapter 2 describes the objective for ICESat/GLAS POD algorithm. Chapter 3 summarizes the dynamic models, and Chapter 4 describes the measurement models for ICESat/GLAS. Chapter 5 describes the least squares estimation algorithm and the problem formulation for multi-satellite orbit determination problem. Chapter 6 summarizes the implementation considerations for ICESat/GLAS POD algorithms. Note that POD ATBD Version 2.2 was written in the pre-launch period, and this version (Version 2.3) includes two Appendices to reflect post-launch and post-mission POD updates. Note also that contents for Chapter 2 through Chapter 6 are the same for Version 2.2 and Version 2.3. Appendix A includes ICESat/GLAS mission summary, and the updated POD standards for generating the operational ("Final") POD. Appendix B describes the 2011 POD reprocessing. Bibliography section was updated to include references for Appendix A and B.

2.0   OBJECTIVE

The objective of the POD algorithm is to determine an accurate position of the center of mass of the spacecraft carrying the GLAS instrument. This position must be expressed in an appropriate Earth-fixed reference frame, such as the International Earth Rotation Service (IERS) Terrestrial Reference Frame (ITRF), but for some applications the position vector must be given in a non-rotating frame, the IERS Celestial Reference Frame (ICRF). Thus, the POD algorithm will provide a data product that consists of time and the (x, y, z) position (ephemeris) of the spacecraft/GLAS center of mass in both the ITRF and the ICRF. The ephemeris will be provided at an appropriate time interval, e.g., 30 sec and interpolation algorithms will enable determination of the position at any time to an accuracy comparable to the numerical integration accuracy. Furthermore, the transformation matrix between ICRF and ITRF will be provided from the POD, along with interpolation algorithm.

3.0   ALGORITHM DESCRIPTION: Orbit

3.1   ICESat/GLAS Orbit Dynamics Overview

Mathematical models employed in the equations of motion to describe the motion of ICESat/GLAS can be divided into three categories: 1) the gravitational forces acting on ICESat/GLAS consist of Earth's geopotential, solid earth tides, ocean tides, planetary third-body perturbations, and relativistic accelerations; 2) the non-gravitational forces consist of drag, solar radiation pressure, earth radiation pressure, and thermal radiation acceleration; and 3) empirical force models that are employed to accommodate unmodeled or mismodeled forces. In this chapter, the dynamic models are described along with the time and reference coordinate systems.

3.2   Equations of Motion, Time and Coordinate Systems

The equations of motion of a near-Earth satellite can be described in an inertial reference frame as follows:

$$\ddot{\overline{r}} = \overline{a}_g + \overline{a}_{ng} + \overline{a}_{emp} \qquad (3.2.1)$$

where $\overline{r}$ is the position vector of the center of mass of the satellite, $\overline{a}_g$ is the sum of the gravitational forces acting on the satellite, $\overline{a}_{ng}$ is the sum of the non-gravitational forces acting on the surfaces of the satellite, and $\overline{a}_{emp}$ is the unmodeled forces which act on the satellite due to either a functionally incorrect or incomplete description of the various forces acting on the spacecraft or inaccurate values for the constant parameters which appear in the force model.

3.2.1   Time System

Several time systems are required for the orbit determination problem. From the measurement systems, satellite laser ranging measurements are usually time-tagged in UTC (Coordinated Universal Time) and GPS measurements are time-tagged in GPS System Time (referred to here as GPS-ST). Although both UTC and GPS-ST are based on atomic time standards, UTC is loosely tied to the rotation of the Earth through the application of "leap seconds" to keep UT1 and UTC within a second. GPS-ST is continuous to avoid complications associated with a discontinuous time scale [*Milliken and Zoller*, 1978]. Leap seconds are introduced on January 1 or July 1, as required. The relation between GPS-ST and UTC is

$$GPS\text{-}ST = UTC + n \qquad\qquad\qquad (3.2.2)$$

where n is the number of leap seconds since January 6, 1980. For example, the relation between UTC and GPS-ST in mid-July, 1999, was GPS-ST = UTC + 13 sec. The independent variable of the near-Earth satellite equations of motion (Eq. 3.2.1) is typically TDT (Terrestrial Dynamical Time), which is an abstract, uniform time scale implicitly defined by equations of motion. This time scale is related to the TAI (International Atomic Time) by the relation

$$TDT = TAI + 32.184^s. \qquad\qquad\qquad (3.2.3)$$

The planetary ephemerides are usually given in TDB (Barycentric Dynamical Time) scale, which is also an abstract, uniform time scale used as the independent variable for the ephemerides of the Moon, Sun, and planets. The transformation from the TDB time to the TDT time with sufficient accuracy for most application has been

given by *Moyer* [1981]. For a near-Earth application like ICESat/GLAS, it is unnecessary to distinguish between TDT and TDB. New time systems are under discussion by the International Astronomical Union. This document will be updated with these time systems, as appropriate.

3.2.2   Coordinate System

The inertial reference system adopted for Eq. 3.2.1 for the dynamic model is the ICRF geocentric inertial coordinate system, which is defined by the mean equator and vernal equinox at Julian epoch 2000.0. The Jet Propulsion Laboratory (JPL) DE-405 planetary ephemeris [*Standish*, 1998], which is based on the ICRF inertial coordinate system, has been adopted for the positions and velocities of the planets with the coordinate transformation from barycentric inertial to geocentric inertial.

Tracking station coordinates, atmospheric drag perturbations, and gravitational perturbations are usually expressed in the Earth fixed, geocentric, rotating system, which can be transformed into the ICRF reference frame by considering the precession and nutation of the Earth, its polar motion, and UT1 transformation. The 1976 International Astronomical Union (IAU) precession [*Lieske et al.*, 1977; *Lieske*, 1979] and the 1980 IAU nutation formula [*Wahr*, 1981b; *Seidelmann*, 1982] with the correction derived from VLBI analysis [*Herring et al.*, 1991] will be used as the model of precession and nutation of the Earth. Polar motion and UT1-TAI variations were derived from Lageos (Laser Geodynamics Satellite) laser ranging analysis [*Tapley et al.*, 1985; *Schutz et al.*, 1988]. Tectonic plate

motion for the continental mass on which tracking stations are affixed has been modeled based on the AM0-2 model [*Minster and Jordan*, 1978; *DeMets et al.*, 1990; *Watkins*, 1990]. *Yuan* [1991] provides additional detailed discussion of time and coordinate systems in the satellite orbit determination problem.

3.3 Gravitational Forces

The gravitational forces can be expressed as:

$$\bar{a}_g = \overline{P}_{geo} + \overline{P}_{st} + \overline{P}_{ot} + \overline{P}_{rd} + \overline{P}_n + \overline{P}_{rel} \qquad (3.3.1)$$

where

$\overline{P}_{geo}$ = perturbations due to the geopotential of the Earth

$\overline{P}_{st}$ = perturbations due to the solid Earth tides

$\overline{P}_{ot}$ = perturbations due to the ocean tides

$\overline{P}_{rd}$ = perturbations due to the rotational deformation

$\overline{P}_n$ = perturbations due to the Sun, Moon and planets

$\overline{P}_{rel}$ = perturbations due to the general relativity

3.3.1 Geopotential

The perturbing forces of the satellite due to the gravitational attraction of the Earth can be expressed as the gradient of the potential, *U*, which satisfies the Laplace equation, $\nabla^2 U = 0$:

$$\nabla U = \nabla(U_s + \Delta U_{st} + \Delta U_{ot} + \Delta U_{rd}) = \overline{P}_{geo} + \overline{P}_{st} + \overline{P}_{ot} + \overline{P}_{ra} \qquad (3.3.2)$$

where U_s is the potential due to the solid-body mass distribution, ΔU_{st} is the potential change due to solid-body tides, ΔU_{ot} is the potential change due to the ocean tides, and ΔU_{rd} is the potential change due to the rotational deformations.

The perturbing potential function for the solid-body mass distribution of the Earth, U_s, is generally expressed in terms of a spherical harmonic expansion, referred to as the geopotential, in a body-fixed reference frame as [*Kaula,* 1966; *Heiskanen and Moritz,* 1967]:

$$U_s(r,\phi,\lambda) = \frac{GM_e}{r} + \frac{GM_e}{r}\sum_{l=1}^{\infty}\sum_{m=0}^{l}\left(\frac{a_e}{r}\right)^l \overline{P}_{lm}(\sin\phi)\left[\overline{C}_{lm}\cos m\lambda + \overline{S}_{lm}\sin m\lambda\right]$$

$$(3.3.3)$$

where

GM_e	=	the gravitational constant of the Earth
a_e	=	the mean equatorial radius of the Earth
$\overline{C}_{lm}, \overline{S}_{lm}$	=	normalized spherical harmonic coefficients of degree l and order m
$\overline{P}_{lm}(\sin\varphi)$	=	the normalized associated Legendre function of degree l and order m
r, ϕ, λ	=	radial distance from the center of mass of the Earth, the geocentric latitude, and the longitude of the satellite

To ensure that the origin of spherical coordinates coincides with the center of mass of the Earth, we define $\overline{C}_{10} = \overline{C}_{11} = \overline{S}_{11} = 0$.

3.3.2 Solid Earth Tides

Since the Earth is a non-rigid elastic body, its mass distribution and the shape will be changed under the gravitational attraction of the perturbing bodies, especially the Sun and the Moon. The temporal variation of the free space geopotential induced from solid Earth tides can be expressed as a change in the external geopotential by the following expression [*Wahr*, 1981a; *Dow,* 1988; *Casotto,* 1989].

$$
\Delta U_{st} = \frac{GM_e}{a_e^2} \sum_{l=2}^{(3)} \sum_{m=0}^{l} \sum_{k(l,m)} H_k e^{i(\Theta_k + \chi_k)} k_k^0 \left[\left(\frac{a_e}{r} \right)^{l+1} Y_m^l(\phi,\lambda) + k_k^+ \left(\frac{a_e}{r} \right)^{l+3} Y_m^{l+2}(\phi,\lambda) \right]
$$

$$(3.3.4)$$

where

$$
Y_l^m(\phi,\lambda) = (-1)^m \sqrt{\frac{(2l+1)}{4\pi} \frac{(l-m)!}{(l+m)!}} P_{lm}(\sin\phi) e^{im\lambda}
$$

$P_{lm}(\sin\phi)$ = the unnormalized associated Legendre function of degree l and order m

H_k = the frequency dependent tidal amplitude in meters (provided in *Cartwright and Tayler* [1971] and *Cartwright and Edden* [1973])

Θ_k, χ_k = Doodson argument and phase correction for constituent k ($\chi_k = 0$, if l-m is even; $\chi_k = -\frac{\pi}{2}$, if l-m is odd)

k_k^0, k_k^+ = Love numbers for tidal constituent k

r, ϕ, λ = geocentric body-fixed coordinates of the satellite

The summation over $k(l,m)$ means that each different l, m combination has a unique list of tidal frequencies, k, to sum over.

The tidally induced variations in the Earth's external potential can be expressed as variations in the spherical harmonic geopotential coefficients [*Eanes et al.* 1983].

$$\Delta \overline{C}_{lm} = \frac{(-1)^m}{a_e \sqrt{4\pi(2-\delta_{0m})}} \sum_k k_k^0 H_k \begin{cases} \cos\Theta_k, & l-m \quad even \\ \sin\Theta_k, & l-m \quad odd \end{cases}$$

$$\Delta \overline{S}_{lm} = \frac{(-1)^m}{a_e \sqrt{4\pi(2-\delta_{0m})}} \sum_k k_k^0 H_k \begin{cases} -\sin\Theta_k, & l-m \quad even \\ \cos\Theta_k, & l-m \quad odd \end{cases} \tag{3.3.5}$$

where δ_{0m} is the Kronecker delta; $\Delta \overline{C}_{lm}$ and $\Delta \overline{S}_{lm}$ are the time-varying geopotential coefficients providing the spatial description of the luni-solar tidal effect.

3.3.3   Ocean Tides

The oceanic tidal perturbations due to the attraction of the Sun and the Moon can be expressed as variations in the spherical harmonic geopotential coefficients. The temporal variation of the free space geopotential induced from the ocean tide deformation, ΔU_{ot}, can be expressed as [*Eanes et al.*, 1983]

$$\Delta U_{ot} = 4\pi G \rho_w a_e \sum_k \sum_{l=0}^{\infty} \sum_{m=0}^{l} \sum_{+}^{-} \frac{1+k_l'}{2l+1} \left(\frac{a_e}{r}\right)^{l+1}$$

$$\times \left[C_{klm}^{\pm} \cos(\Theta_k \pm m\lambda) + S_{klm}^{\pm} \sin(\Theta_k \pm m\lambda) \right] P_{lm}(\sin\phi) \tag{3.3.6}$$

where ρ_w is the mean density of sea water, k is the ocean tide constituent index, k'_l is the load Love number of degree l, $C^{\pm}_{klm}$ and $S^{\pm}_{klm}$ are the unnormalized prograde and retrograde tide coefficients, and Θ_k is the Doodson argument for constituent k.

The above variations in the Earth's external potential due to the ocean tide can be expressed as variations in the spherical harmonic geopotential coefficients as follows [*Eanes et al.* 1983].

$$\Delta\overline{C}_{lm} = F_{lm}\sum_k A_{klm}$$

$$\Delta\overline{S}_{lm} = F_{lm}\sum_k B_{klm} \tag{3.3.7}$$

where F_{lm}, A_{klm}, and B_{klm} are defined as

$$F_{lm} = \frac{4\pi a_e^2 \rho_w}{M_e}\sqrt{\frac{(l+m)!}{(l-m)!(2l+1)(2-\delta_{0m})}}\left(\frac{1+k'_l}{2l+1}\right) \tag{3.3.8}$$

and

$$\begin{bmatrix} A_{klm} \\ B_{klm} \end{bmatrix} = \begin{bmatrix} (C^+_{klm} + C^-_{klm}) \\ (S^+_{klm} - S^-_{klm}) \end{bmatrix}\cos\Theta_k + \begin{bmatrix} (S^+_{klm} + S^-_{klm}) \\ (C^-_{klm} - C^+_{klm}) \end{bmatrix}\sin\Theta_k \tag{3.3.9}$$

3.3.4 Rotational Deformation

Since the Earth is elastic and includes a significant fluid component, changes in the angular velocity vector will produce a variable centrifugal force, which consequently deforms the Earth. This deformation, which is called "rotational deformation", can be expressed as the change of the centrifugal potential, U_c [*Lambeck*, 1980] given by

$$U_c = \frac{1}{3}\omega^2 r^2 + \Delta U_c \tag{3.3.10}$$

where

$$\Delta U_c = \frac{r^2}{6}(\omega_1^2 + \omega_2^2 - 2\omega_3^2)\, P_{20}(\sin\phi)$$

$$-\frac{r^2}{3}(\omega_1\omega_3\cos\lambda + \omega_2\omega_3\sin\lambda)\, P_{21}(\sin\phi)$$

$$+\frac{r^2}{12}\Big[(\omega_2^2-\omega_1^2)\cos2\lambda - 2\omega_1\omega_2\sin2\lambda\Big]\, P_{22}(\sin\phi) \tag{3.3.11}$$

and $\omega_1 = \Omega m_1$, $\omega_2 = \Omega m_2$, $\omega_3 = \Omega(1+m_3)$, and $\omega^2 = (\omega_1^2+\omega_2^2+\omega_3^2)$. Ω is the mean angular velocity of the Earth, m_i are small dimensionless quantities which are related to the polar motion and the Earth rotation parameters by the following expressions:

$$m_1 = x_p$$

$$m_2 = -y_p \tag{3.3.12}$$

$$m_3 = \frac{d\,(UT1\text{-}TAI)}{d\,(TAI)}$$

The first term of Eq. (3.3.10) is negligible in the variation of the geopotential, thereby the variation of the free space geopotential outside of the Earth due to the rotational deformation can be written as

$$\Delta U_{rd} = \left(\frac{a_e}{r}\right)^3 k_2\, \Delta U_c(a_e) \tag{3.3.13}$$

The above variations in the Earth's external potential due to the rotational deformation can be expressed as variations in the spherical harmonic geopotential coefficients as follows.

$$\Delta C_{20} = \frac{a_e^3}{6GM_e}\Big[m_1^2+m_2^2-2(1+m_3)^2\Big]\Omega^2 k_2 \approx \frac{-a_e^3}{3GM_e}(1+2m_3)\Omega^2 k_2$$

$$\Delta C_{21} = \frac{-a_e^3}{3GM_e} m_1(1+m_3)\Omega^2 k_2 \approx \frac{-a_e^3}{3GM_e} m_1\Omega^2 k_2$$

$$\Delta S_{21} = \frac{-a_e^3}{3GM_e} m_2(1+m_3)\Omega^2 k_2 \approx \frac{-a_e^3}{3GM_e} m_2\Omega^2 k_2 \tag{3.3.14}$$

$$\Delta C_{22} = \frac{a_e^3}{12GM_e} (m_2{}^2 - m_1{}^2)\Omega^2 k_2 \approx 0$$

$$\Delta S_{22} = \frac{-a_e^3}{6GM_e} (m_2 m_1)\Omega^2 k_2 \approx 0$$

As a consequence of Eqs. (3.3.2), (3.3.3), (3.3.4), (3.3.6), and (3.3.13), the resultant gravitational potential for the Earth can be expressed as

$$U(r,\phi,\lambda) = \frac{GM_e}{r} + \frac{GM_e}{r}\sum_{l=1}^{\infty}\sum_{m=0}^{l}\left(\frac{a_e}{r}\right)^l \overline{P}_{lm}\left(\sin\phi\right)$$

$$\times \left[\left(\overline{C}_{lm}+\Delta\overline{C}_{lm}\right)\cos m\lambda + \left(\overline{S}_{lm}+\Delta\overline{S}_{lm}\right)\sin m\lambda\right] \tag{3.3.15}$$

where both the solid Earth and oceans contribute to the periodic variations $\Delta\overline{C}_{lm}$ and $\Delta\overline{S}_{lm}$.

3.3.5   N-Body Perturbation

The gravitational perturbations of the Sun, Moon and other planets can be modeled with sufficient accuracy using point mass approximations. In the geocentric inertial coordinate system, the N-body accelerations can be expressed as:

$$\overline{P}_n = \sum_i GM_i\left[\frac{\overline{r}_i}{r_i^3} - \frac{\overline{\Delta}_i}{\Delta_i^3}\right] \tag{3.3.16}$$

where

G = the universal gravitational constant

M_i = mass of the *i*-th perturbing body

$\bar{r}_i$ = position vector of the *i*-th perturbing body in geocentric inertial coordinates

$\bar{\Delta}_i$ = position vector of the *i*-th perturbing body with respect to the satellite

The values of $\bar{r}_i$ can be obtained from the Jet Propulsion Laboratory Development Ephemeris-405 (JPL DE-405) [*Standish*, 1998].

3.3.6 General Relativity

The general relativistic perturbations on the near-Earth satellite can be modeled as [*Huang et al.*, 1990; *Ries et al.*, 1988],

$$\bar{P}_{rel} = \frac{GM_e}{c^2 r^3} \left\{ \left[(2\beta + 2\gamma) \frac{GM_e}{r} - \gamma(\bar{r} \cdot \bar{r}) \right] \bar{r} + (2 + 2\gamma)(\bar{r} \cdot \dot{\bar{r}}) \dot{\bar{r}} \right\}$$

$$+ 2\,(\bar{\Omega} \times \dot{\bar{r}}) \qquad\qquad (3.3.17)$$

$$+ L\,(1+\gamma) \frac{GM_e}{c^2 r^3} \left[\frac{3}{r^2} (\bar{r} \times \dot{\bar{r}})(\bar{r} \cdot \bar{J}) + (\dot{\bar{r}} \times \bar{J}) \right]$$

where

$$\bar{\Omega} \approx \left(\frac{1+2\gamma}{2} \right) \dot{\bar{R}}_{ES} \times \left[\frac{-GM_s \bar{R}_{ES}}{c^2 R_{ES}^3} \right]$$

c   = the speed of light in the geocentric frame

$\bar{r}, \dot{\bar{r}}$ = the geocentric satellite position and velocity vectors

$\bar{R}_{ES}$ = the position of the Earth with respect to the Sun

GM_e, GM_s = the gravitational constants for the Earth and the Sun, respectively

$\bar{J}$ = the Earth's angular momentum per unit mass

($|\bar{J}| = 9.8 \times 10^8$ m²/sec)

L = the Lense-Thirring parameter

β, γ = the parameterized post-Newtonian (PPN) parameters

The first term of Eq. (3.3.17) is the Schwarzschild motion [*Huang et al.*, 1990] and describes the main effect on the satellite orbit with the precession of perigee. The second term of Eq. (3.3.17) is the effect of geodesic (or de Sitter) precession, which results in a precession of the orbit plane [*Huang and Ries*, 1987]. The last term of Eq. (3.3.17) is the Lense-Thirring precession, which is due to the angular momentum of the rotating Earth and results in, for example, a 31 mas/yr precession in the node of the Lageos orbit [*Ciufolini*, 1986].

3.4   Nongravitational Forces

The non-gravitational forces acting on the satellite can be expressed as:

$$\bar{a}_{ng} = \bar{P}_{drag} + \bar{P}_{solar} + \bar{P}_{earth} + \bar{P}_{thermal} \tag{3.4.1}$$

where

$\bar{P}_{drag}$ = perturbations due to the atmospheric drag

$\bar{P}_{solar}$ = perturbations due to the solar radiation pressure

$\bar{P}_{earth}$ = perturbations due to the Earth radiation pressure

$\bar{P}_{thermal}$ = perturbations due to the thermal radiation

Since the surface forces depend on the shape and orientation of the satellite, the models are satellite dependent. In this section, however, general models are described.

3.4.1 Atmospheric Drag

A near-Earth satellite of arbitrary shape moving with some velocity $\bar{v}$ in an atmosphere of density ρ will experience both lift and drag forces. The lift forces are small compared to the drag forces, which can be modeled as [*Schutz and Tapley*, 1980b]

$$\bar{P}_{drag} = -\frac{1}{2}\rho\left(\frac{C_d A}{m}\right)v_r\bar{v}_r \tag{3.4.2}$$

where

$$
\begin{array}{ll}
\rho & = \text{the atmospheric density} \\
\bar{v}_r & = \text{the satellite velocity relative to the atmosphere} \\
v_r & = \text{the magnitude of } \bar{v}_r \\
m & = \text{mass of the satellite} \\
C_d & = \text{the drag coefficient for the satellite} \\
A & = \text{the cross-sectional area of the main body perpendicular to } \bar{v}_r
\end{array}
$$

The parameter $\dfrac{C_d A}{m}$ is sometimes referred to as the ballistic coefficient. When more detailed modeling is needed, the drag force on any specific spacecraft surface, for example, the solar panel, can be modeled as

$$\bar{P}_{paneld} = -\frac{1}{2}\rho\left(\frac{C_{dp}\left|A_p\cos\gamma\right|}{m}\right)v_r\bar{v}_r \tag{3.4.3}$$

where

C_{dp} = the drag coefficient for the solar panel

A_p = the solar panel's area

γ = the angle between the solar panel surface normal unit vector, $\hat{n}$, and satellite velocity vector, $\overline{v}_r$ (i.e. $\cos\gamma = \hat{n} \cdot \left(\dfrac{\overline{v}_r}{v_r}\right)$)

$|A_p\cos\gamma|$ = the effective solar panel cross sectional area perpendicular to $\overline{v}_r$

There are a number of empirical atmospheric density models used for computing the atmospheric density. These include the Jacchia 71 [*Jacchia*, 1971], Jacchia 77 [*Jacchia*, 1977], the Drag Temperature Model (DTM) [*Barlier et al.*, 1977], DTM-2000 [*Bruinsma and Thuillier*, 2000], MSIS-90 [*Hedin*, 1991] and NRLMSISE-00 [*Hedin et al.*, 1996]. The density computed by using any of these models could be in error anywhere from 10% to over 200% depending on solar activity [*Shum et al.*, 1986]. To account for the deviations in the computed values of density from the true density, the computed values of density, ρ_c, can be modified by using empirical parameters which are adjusted in the orbit solution. Once-per-revolution density correction parameters [*Elyasberg et al.*, 1972; *Shum et al.*, 1986] have been shown to be especially effective for these purposes such that

$$\rho = \rho_c[1 + C_1 \cos(M+\omega) + C_2 \sin(M+\omega)] \qquad (3.4.4)$$

where

C_1, C_2 = the once-per-revolution density correction coefficients

M = mean anomaly of the satellite

ω = argument of perigee of the satellite

3.4.2   Solar Radiation Pressure

The Sun emits a nearly constant amount of photons per unit of time. At a mean distance of 1 A.U. from the Sun, this radiation pressure is characterized as a momentum flux having an average value of 4.56×10^{-6} N/m^2.   The direct solar radiation pressure from the Sun on a satellite is modeled as [*Tapley and Ries*, 1987]

$$\overline{P}_{solar} = -P \, (1 + \eta) \frac{A}{m} \, \nu \, \widehat{u} \tag{3.4.5}$$

where

P	= the momentum flux due to the Sun
η	= reflectivity coefficient of the satellite
A	= the cross-sectional area of the satellite normal to the Sun
m	= mass of the satellite
ν	= the eclipse factor ($\nu = 0$ if the satellite is in full shadow, $\nu = 1$ if the satellite is in full Sun, and $0 < \nu < 1$ if the satellite is in partial shadow)
$\widehat{u}$	= the unit vector pointing from the satellite to the Sun

Similarly, the solar radiation pressure perturbation on an individual satellite surface, like the satellite's solar panel, can be modeled as

$$\overline{P}_{panels} = -P \, \nu \frac{\left|A_p \cos\gamma\right|}{m} \left(\widehat{u} + \eta_p \, \widehat{n}\right) \tag{3.4.6}$$

where

A_p	= the solar panel area
$\widehat{n}$	= the surface normal unit vector of the solar panel

γ = the angle between the solar panel surface normal unit vector, $\hat{n}$, and satellite-Sun unit vector, $\hat{u}$ (i.e. $\cos\gamma = \hat{u} \cdot \hat{n}$)

$|A_p\cos\gamma|$ = the effective solar panel cross sectional area perpendicular to $\hat{u}$

The reflectivity coefficient, η, represents the averaged effect over the whole satellite rather than the actual surface reflectivity. Conical or cylindrical shadow models for the Earth and the lunar shadow are used to determine the eclipse factor, v. Since there are discontinuities in the solar radiation perturbation across the shadow boundary, numerical integration errors occur for satellites, which are in the shadowing region. The modified back differences (MBD) method [*Anderle*, 1973] can be implemented to account for these errors [*Lundberg*, 1985; *Feulner*, 1990].

3.4.3 Earth Radiation Pressure

Not only the direct solar radiation pressure, but also the radiation pressure imparted by the energy flux of the Earth should be modeled for the precise orbit determination of any near-Earth satellite. The Earth radiation pressure model can be summarized as follows [*Knocke and Ries*, 1987; *Knocke*, 1989].

$$\overline{P}_{earth} = (1+\eta_e)A'\frac{A_c}{mc}\sum_{j=1}^{N}\left[\left(\tau a E_s \cos\theta_s + eM_B\right)\hat{r}\right]_j \qquad (3.4.7)$$

where

η_e = satellite reflectivity for the Earth radiation pressure

A' = the projected, attenuated area of a surface element of the Earth

A_c = the cross sectional area of the satellite

m = the mass of the satellite

$$c \qquad = \text{the speed of light}$$

$$\tau \qquad = 0 \text{ if the center of the element } j \text{ is in darkness}$$

$$\qquad \qquad 1 \text{ if the center of the element } j \text{ is in daylight}$$

$$a, e \qquad = \text{albedo and emissivity of the element } j$$

$$E_s \qquad = \text{the solar momentum flux density at 1 A.U.}$$

$$\theta_s \qquad = \text{the solar zenith angle}$$

$$M_B \qquad = \text{the exitance of the Earth}$$

$$\hat{r} \qquad = \text{the unit vector from the center of the element } j \text{ to the satellite}$$

$$N \qquad = \text{the total number of segments}$$

This model is based on *McCarthy and Martin* [1977].

The nominal albedo and emissivity models can be represented as

$$a = a_0 + a_1 P_{10}(\sin\phi) + a_2 P_{20}(\sin\phi) \tag{3.4.8}$$

$$e = e_0 + e_1 P_{10}(\sin\phi) + e_2 P_{20}(\sin\phi) \tag{3.4.9}$$

where

$$a_1 = c_0 + c_1 \cos\omega(t\text{-}t_0) + c_2 \sin\omega(t\text{-}t_0) \tag{3.4.10}$$

$$e_1 = k_0 + k_1 \cos\omega(t\text{-}t_0) + k_2 \sin\omega(t\text{-}t_0) \tag{3.4.11}$$

and

$$P_{10}, P_{20} \quad = \text{the first and second degree Legendre polynomial}$$

$$\phi \qquad = \text{the latitude of the center of the element on the Earth's surface}$$

$$\omega \qquad = \text{frequency of the periodic terms (period = 365.25 days)}$$

$$t\text{-}t_0 \qquad = \text{time from the epoch of the periodic term}$$

This model, based on analyses of Earth radiation budgets by *Stephens et al*. [1981], characterizes both the latitudinal variation in Earth radiation and the seasonally dependent latitudinal asymmetry.

3.4.4   Thermal Radiation Perturbation

Since the temperatures of the satellite's surface are not uniform due to the internal and external heat fluxes, there exists a force due to a net thermal radiation imbalance. This perturbation depends on the shape, the thermal property, the pattern of thermal dumping, the orbit characteristics, and the thermal environment of the satellite as a whole. This modeling can be quite complex. For example, if a satellite has active louvers for heat dissipation, the thermal force can have specular characteristics whereas the heat loss to space from a flat plat is normally diffusive. Even a clean, perfect spherical satellite like Lageos [*Ries*, 1989] has been found to have a range of detectable thermally induced forces. It is observed for GPS satellites that there are unexplained forces in the body-fixed +*Y* or -*Y* direction, that is along solar panel rotation axis, which causes unmodeled accelerations [*Fliegel et al.,* 1992] believed to be of thermal origin. This acceleration is referred to as the "Y-bias". Possible causes of the Y-bias are solar panel axis misalignment, solar sensor misalignment, and the heat generated in the GPS satellite body, which is radiated preferentially from louvers on the +*Y* side. Since this Y-bias perturbation is not predictable, it can be modeled as

$$\overline{P}_{ybias} \; = \; \alpha \cdot \; \widehat{u}_Y \tag{3.4.12}$$

where $\widehat{u}_Y$ is a unit vector in the *Y*-direction, and the scale factor, α, is estimated for each GPS satellite. Models, which are satellite-specific, are required to properly account for these effects depending on the orbit accuracy needed within a given application.

3.4.5   GPS Solar Radiation Pressure Models

At the 20,000-km altitude of GPS satellite, solar radiation is the dominant non-gravitational force acting on the spacecraft. Several GPS solar radiation pressure models are currently available, and two of those models are summarized in this section.

Rockwell International Corporation, which was the spacecraft contractor for the Block I and II GPS satellites, developed GPS satellite solar radiation pressure models, known as ROCK4 for Block I, and ROCK42 for Block II [*Fliegel et al*., 1992]. These models treat a spacecraft as a set of flat or cylindrical surfaces. Diffusive and specular forces acting on each surface are computed and summed in the spacecraft body-fixed coordinate system. The +*Z* direction is toward the satellite-Earth vector. The +*Y* direction is along one of the solar panel center beams. The satellite is maneuvered so that the *X*-axis will be kept in the plane defined by the Earth, the Sun and the satellite. As a result, the solar radiation pressure forces are confined in the *X*-*Z* plane, since the *Y*-axis is perpendicular to the Earth, Sun and the satellite plane. The ROCK4 model also provides solar radiation formulas for the *X*- and *Z*- acceleration components as a function of the angle between the Sun and the +*Z*-axis, e.g. T10 for Block I, and T20 for Block II GPS satellites [*Fliegel et al*., 1992].

Recently the Center of Orbit Determination in Europe (CODE) developed a solar radiation pressure (RPR) model by analyzing 5.5 years of GPS orbit solutions [*Springer et al.*, 1998]. The RPR model is represented by eighteen orbit parameters in two different coordinate systems. Those are satellite body-fixed coordinate system described above, and the Sun-oriented reference system, which consists of the *D*-, *Y*-, and *B*-axis [*Beutler et al.*, 1994]. The *D*-axis is the satellite-Sun direction positive towards the Sun, *Y*-axis is identical to the ROCK4 *Y*-axis, and *B*-axis completes a right-handed system. The orbit parameters include three constant terms in the *D*-, *Y*-, and *B*-direction, a once-per-revolution term in the *Z*-direction, and once- and three times-per-revolution terms in the *X*-direction. The solar radiation acceleration is expressed as

$$a_D = D_0 + D_{C2}\,cos(2\beta) + D_{C4}\,cos(4\beta)$$

$$a_Y = Y_0 + Y_C\,cos(2\beta)$$

$$a_B = B_0 + B_C\,cos(2\beta) \tag{3.4.13}$$

$$a_Z = \{Z_0 + Z_{C2}\,cos(2\beta) + Z_{S2}\,sin(2\beta)$$

$$+ Z_{C4}\,cos(4\beta) + Z_{S4}\,sin(4\beta)\}sin(u - u_0)$$

$$a_X = \{X_{10} + X_{1C}\,cos(2\beta) + X_{1S}\,sin(2\beta)\}sin(u - u_0)$$

$$+\{X_{30} + X_{3C}\,cos(2\beta) + X_{3S}\,sin(2\beta)\}sin(3u - u_0)$$

where u is the argument of latitude of satellite in the orbit plane, u_0 is the latitude of the Sun in the orbit plane, and β is the angular distance between the orbit plane and the Sun.

3.4.6   ICESat/GLAS "Box-Wing" Model

For modeling of non-gravitational perturbations on T/P, the "box-wing" model or the so-called macro-model [*Marshall et al.*, 1992] was developed based on a thermal analysis of the spacecraft [*Antreasian and Rosborough*, 1992]. In the macro-model, the spacecraft main body and the solar panel are represented by a simple geometric model, a box and a wing, and the solar radiation and the thermal forces are computed for each surface and summed over the surfaces. For example, the solar radiation acceleration for the macro-model is computed using the following equation [*Milani et al.*, 1987].

$$\overline{P}_{solar} = -P\frac{\alpha \cdot \nu}{m}\sum_{i=1}^{nface} A_i \cos\theta_i \left[2(\frac{\delta_i}{3} + \rho_i \cos\theta_i)\hat{n}_i + (1-\rho_i)\hat{s} \right] \qquad (3.4.14)$$

where

$\overline{P}_{solar}$ = the solar radiation pressure acceleration

P = the momentum flux due to the Sun

α = the scale factor of the acceleration

ν = the eclipse factor (0 for full shadow, 1 for full Sun)

m = mass of the satellite

A_i = surface area of the i-th plate

θ_i = angle between surface normal and satellite-Sun vector for i-th plate

$\widehat{n}_i$ = surface normal unit vector for *i*-th plate

$\widehat{s}$ = satellite-Sun unit vector

ρ_i = specular reflectivity for *i*-th plate

δ_i = diffusive reflectivity for *i*-th plate

nface   = total number of plates in the model

A similar model is being developed for the ICESat/GLAS satellite, and the model parameters, including the specular and diffusive reflectivity coefficients, will be tuned using the tracking data.

3.5   Empirical Forces

To account for the unmodeled forces, which act on the satellite or for incorrect force models, some empirical parameters are customarily introduced in the orbit solution. These include the empirical tangential perturbation and the one-cycle-per-orbital-revolution (1cpr) force in the radial, transverse, and normal directions [*Colombo*, 1986; *Colombo*, 1989]. Especially for satellites like ICESat/GLAS which are tracked continuously with high precision data, introduction of these parameters can significantly reduce orbit errors occurring at the 1cpr frequency and in the along track direction [*Rim et al.*, 1996].

3.5.1   *Empirical Tangential Perturbation*

Unmodeled forces in the tangential direction, either along the inertial velocity or along the body-fixed velocity, may be estimated by using empirical

models during the orbit determination process. This tangential perturbation can be modeled empirically as

$$\overline{P}_{tangen} = C_t \, \widehat{u}_t \tag{3.5.1}$$

where

C_t = empirical tangential parameter

$\widehat{u}_t$ = the unit vector in the tangential direction (along inertial velocity or body-fixed velocity)

Such forces are estimated when it is believed that there are mismodeled or unmodeled non-conservative forces in the tangential direction. A set of piecewise constants, C_t, can be estimated to account for these unmodeled tangential perturbations.

3.5.2   Once-per Revolution RTN Perturbation

Unmodeled perturbations in the radial, transverse, and normal directions can be modeled as

$$\overline{P}_{rtn} = \begin{bmatrix} P_r \\ P_t \\ P_n \end{bmatrix} = \begin{bmatrix} C_r \cos u + S_r \sin u \\ C_t \cos u + S_t \sin u \\ C_n \cos u + S_n \sin u \end{bmatrix} \tag{3.5.2}$$

where

P_r = one-cycle-per-revolution radial perturbation

P_t = one-cycle-per-revolution transverse perturbation

P_n = one-cycle-per-revolution normal perturbation

u = the argument of latitude of the satellite

C_r, S_r = the one-cycle-per-revolution radial parameters

C_t, S_t = the one-cycle-per-revolution transverse parameters

C_n, S_n = the one-cycle-per-revolution normal parameters

These empirical perturbations, which are computed in the radial, transverse, and normal components, are transformed into the geocentric inertial components. These parameters are introduced as needed with complete or subsets of empirical terms being used.

4.0   ALGORITHM DESCRIPTION: Measurements

4.1   ICESat/GLAS Measurements Overview

The GPS measurements will be the primary measurement type for the ICESat/GLAS POD, while the laser range measurement will serve as a secondary source of verification and evaluation of the GPS-based ICESat/GLAS POD product. In this chapter, the mathematical models of the GPS and laser range measurements are discussed.

4.2   GPS Measurement Model

The GPS measurements are ranges, which are computed from measured time or phase differences between received signals and receiver generated signals. Since these ranges are biased by satellite and receiver clock errors, they are called pseudoranges.   In this section, code pseudorange (PR) measurements, phase pseudorange measurements (PPR), double-differenced high-low phase pseudorange measurements (DDHL) which involve one ground station, two GPS satellites, and one low Earth orbiting satellite, are discussed.   Consult *Hofmann-Wellenhof et al.* [1992] and *Remondi* [1984] for more discussion of GPS measurement models.

4.2.1   Code Pseudorange Measurement

The PR measurement, $\rho^c{}_{PR}$, can be modeled as follows,

$$\rho^c{}_{PR} = \rho - c \cdot \delta t_t + c \cdot \delta t_r + \delta\rho_{trop} + \delta\rho_{iono} + \delta\rho_{rel} \qquad (4.2.1)$$

where ρ is the slant range between the GPS satellite and the receiver receiving the GPS signal, c is the speed of light, δt_t is the GPS satellite's clock error, δt_r is the receiver's clock error, $\delta\rho_{trop}$ is the tropospheric path delay, $\delta\rho_{iono}$ is the ionospheric path delay, and $\delta\rho_{rel}$ is the correction for relativistic effects.

4.2.2 Phase Pseudorange Measurement

The carrier phase measurement between a GPS satellite and a ground station can be modeled as follows,

$$\phi^{c\,j}_i(t_{R_i}) \;=\; \phi^j(t_{T_i}) - \phi_i(t_{R_i}) + N_i^j(t_{0_i}) \tag{4.2.2a}$$

where t_{R_i} is the receive time at the i-th ground receiver, t_{T_i} is the transmit time of the j-th satellite's phase being received by the i-th receiver at t_{R_i}, $\phi^{c\,j}_i(t_{R_i})$ is the computed phase difference between the j-th GPS satellite and i-th ground receiver at t_{R_i}, $\phi^j(t_{T_i})$ is the phase of j-th GPS satellite signal received by i-th receiver, $\phi_i(t_{R_i})$ is the phase of i-th ground receiver at t_{R_i}, t_{0_i} is the initial epoch of the i-th receiver, and $N_i^j(t_{0_i})$ is the integer bias which is unknown and is often referred to as an "ambiguity bias". Similarly, the carrier phase measurement between a GPS satellite and a low satellite can be modeled as follows,

$$\phi^{c\,j}_u(t_{R_u}) \;=\; \phi^j(t_{T_u}) - \phi_u(t_{R_u}) + N_u^j(t_{0_u}) \tag{4.2.2b}$$

where t_{R_u} is the received time of the on-board receiver of the user satellite, t_{T_u} is the transmit time of the j-th satellite's phase being received by the user satellite at t_{R_u}, $\phi^{c\,j}_u(t_{R_u})$ is the computed phase difference between j-th GPS satellite and the user satellite at t_{R_u}, $\phi^j(t_{T_u})$ is the phase of j-th GPS satellite signal received by the user

satellite, $\phi_u(t_{R_u})$ is the phase of the user satellite at t_{R_u}, t_{0_u} is the initial epoch of the user satellite, and $N_u^j(t_{0_u})$ is the unknown integer bias.

The signal transmit time of the j-th GPS satellite can be related to the signal receive time by

$$t_{T_i}^j \; = \; t_{R_i} \; - \; (\rho_i^j(t_{R_i})/c) \; - \; \delta t_{\phi_i}^j \tag{4.2.3a}$$

$$t_{T_u}^j \; = \; t_{R_u} \; - \; (\rho_u^j(t_{R_u})/c) \; - \; \delta t_{\phi_u}^j \tag{4.2.3b}$$

where ρ_i^j is the geometric line of sight range between j-th GPS satellite and i-th ground receiver, ρ_u^j is the slant range between j-th GPS satellite and the on-board receiver of the user satellite, $\delta t_{\phi_i}^j$ is the sum of ionospheric delay, tropospheric delay, and relativistic effect on the signal traveling from j-th GPS satellite to i-th ground receiver, $\delta t_{\phi_u}^j$ is the sum of ionospheric path delay, tropospheric path delay, and relativistic effect on the signal traveling from j-th satellite to the on-board receiver of the user satellite. Since the time tag, t_i or t_u, of the measurement is in the receiver time scale which has some clock error, the true receive times are

$$t_{R_i} \; = \; t_i \; - \; \delta t_{c_i} \tag{4.2.4a}$$

$$t_{R_u} \; = \; t_u \; - \; \delta t_{c_u} \tag{4.2.4b}$$

where δt_{c_i} is the clock error of the i-th ground receiver at t_{R_i} and δt_{c_u} is the clock error of the on-board receiver of the user satellite at t_{R_u}. Since the satellite oscillators and the receiver oscillators are highly stable clocks, the (1σ) change of the frequency over the specified period, $\frac{\Delta f}{f}$, is on the order of 10^{-12}. With such high stability, the linear approximation of $\phi(t + \delta t) \; = \; \phi(t) \; + \; f \cdot \delta t$ can be used for δt which is usually

less than 1 second. By substituting Eqs. (4.2.3a) and (4.2.4a) into Eq. (4.2.2a), and neglecting higher order terms, Eq. (4.2.2a) becomes

$$\phi^{c\,j}_i(t_{R_i}) = \phi^j(t_i) - f^j \cdot [\ \delta t_{c_i} + \rho^j_i(t_{R_i})/c + \delta t^j_{\phi_i} \ ]$$

$$- \phi_i(t_i) + f_i \ \delta t_{c_i} + N^j_i(t_{0_i}) \tag{4.2.5a}$$

Similarly, the phase measurement between the j-th GPS satellite and the user satellite can be modeled as follows,

$$\phi^{c\,j}_u(t_{R_u}) = \phi^j(t_u) - f^j \cdot [\ \delta t_{c_u} + \rho^j_u(t_{R_u})/c + \delta t^j_{\phi_u} \ ]$$

$$- \phi_u(t_u) + f_u \ \delta t_{c_u} + N^j_u(t_{0_u}) \tag{4.2.5b}$$

By multiplying a negative nominal wavelength, $-\lambda = -c \, / f_0$, where f_0 is the nominal value for both the transmit frequency of the GPS signal and the receiver mixing frequency, Eq. (4.2.5a) becomes the phase pseudorange measurement,

$$PPR^{c\,j}_i = \frac{f^j}{f_0} \rho^j_i(t_{R_i}) + \frac{f^j}{f_0} \delta\rho^j_{\phi_i} + \frac{f^j}{f_0} c \ \delta t_{c_i} - \frac{f_i}{f_0} c \ \delta t_{c_i}$$

$$- \frac{c}{f_0} \cdot \left[\phi^j(t_i) - \phi_i(t_i) \right] + C^j_i \tag{4.2.6}$$

where $\delta\rho^j_{\phi_i} = c \ \delta t^j_{\phi_i}$ and $C^j_i = -\left(\frac{c}{f_0}\right) \cdot N^j_i$.

The first term of second line of Eq. (4.2.6) can be expanded using the following relations:

$$\phi^j(t_i) - \phi_i(t_i) = \phi^j(t_0) - \phi_i(t_0) + \int_{t0}^{ti} \left(f^j - f_i \right) dt \tag{4.2.7}$$

However, $\phi^j(t_0) - \phi_i(t_0) = f^j \ \delta t^j_c(t_0) - f_i \ \delta t_{c_i}(t_0)$, which is the time difference between the satellite and the receiver clocks at the first data epoch, t_0. And

$\int_{t_0}^{t_i} \left(f^j - f_i \right) dt$ is the total number of cycles the two oscillators have drifted apart over the interval from t_0 to t_i. According to *Remondi* [1984], this is equivalent to the statement that the two clocks have drifted apart, timewise, by amount $\left[\delta t_c^{\,j}(t_i) - \delta t_{c_i}(t_i) \right] - \left[\delta t_c^{\,j}(t_0) - \delta t_{c_i}(t_0) \right]$. Thus,

$$\phi^j(t_i) - \phi_i(t_i) = f^j \cdot \delta t_c^{\,j} - f_i \cdot \delta t_{c_i} \tag{4.2.8}$$

After substituting Eq. (4.2.8), Eq. (4.2.6) becomes,

$$PPR^c{}_i^j = \frac{f^j}{f_0}\, \rho_i^j(t_{R_i}) + \frac{f^j}{f_0}\, \delta\rho_{\phi_i}^{\,j} - \frac{f^j}{f_0}\, c\; \delta t_c^{\,j} + \frac{f^j}{f_0}\, c\; \delta t_{c_i} + C_i^j \tag{4.2.9a}$$

Similarly, the phase pseudorange between *j*-th satellite and a user satellite can be written as,

$$PPR^c{}_u^j = \frac{f^j}{f_0}\, \rho_u^j(t_{R_u}) + \frac{f^j}{f_0}\, \delta\rho_{\phi_u}^{\,j} - \frac{f^j}{f_0}\, c\; \delta t_c^{\,j} + \frac{f^j}{f_0}\, c\; \delta t_{c_u} + C_u^j \tag{4.2.9b}$$

Since the GPS satellites have highly stable oscillators, which have 10^{-11} or 10^{-12} clock drift rate, the frequencies of those clocks usually stay close to the nominal frequency, f_0. If the frequencies are expressed as $f^j = f_0 + \Delta f^j$, where Δf is clock frequency offset from the nominal value, Eqs. (4.2.9a) and (4.2.9b) become as follows after ignoring negligible terms:

$$PPR^c{}_i^j = \rho_i^j(t_{R_i}) + \delta\rho_{\phi_i}^{\,j} - c\; \delta t_c^{\,j} + c\; \delta t_{c_i} + C_i^j \tag{4.2.10a}$$

$$PPR^c{}_u^j = \rho_u^j(t_{R_u}) + \delta\rho_{\phi_u}^{\,j} - c\; \delta t_c^{\,j} + c\; \delta t_{c_u} + C_u^j \tag{4.2.10b}$$

Note that $\rho_i^j(t_{R_i})$ and $\rho_u^j(t_{R_u})$ could be expanded as

$$\rho_i^j(t_{R_i}) = \rho_i^j(t_i) - \dot{\rho}_i^j\; \delta t_{c_i} \tag{4.2.11a}$$

$$\rho_u^j(t_{R_u}) = \rho_u^j(t_u) - \dot{\rho}_u^j \, \delta t_{c_u}$$ (4.2.11b)

Thus, Eqs. (4.2.10a) and (4.2.10b) become

$$PPR^c{}_i^j = \rho_i^j(t_i) + \delta\rho_{\phi_i}^j - c \, \delta t_c^j + c \, \delta t_{c_i} - \dot{\rho}_i^j \, \delta t_{c_i} + C_i^j$$ (4.2.12a)

$$PPR^c{}_u^j = \rho_u^j(t_u) + \delta\rho_{\phi_u}^j - c \, \delta t_c^j + c \, \delta t_{c_u} - \dot{\rho}_u^j \, \delta t_{c_u} + C_u^j$$ (4.2.12b)

Eq. (4.2.12a) is the phase pseudorange measurement between a ground receiver and a GPS satellite, and Eq. (4.2.12b) is the phase pseudorange measurement between a GPS satellite and a user satellite. Note that the clock errors would be estimated for each observation epoch.

4.2.3   Double-Differenced High-Low Phase Pseudorange Measurement

By subtracting Eq. (4.2.2b) from Eq. (4.2.2a), a single-differenced high-low phase measurement can be formed as follows,

$$SDHLP^c{}_i{}^j{}_u = \phi^c{}_i^j(t_{R_i}) - \phi^c{}_u^j(t_{R_u})$$ (4.2.13)

If another single-differenced high-low phase measurement can be obtained between i-th ground receiver, k-th GPS satellite, and the user satellite, a double-differenced high-low phase measurement can be formed by subtracting those two single-differenced high-low phase measurements.

$$DDHLP^c{}_{iu}^{jk} = -f^j \cdot \left[\delta t_{ci} + \rho_i^j(t_{R_i})/c + \delta t_{\phi_i}{}^j \right]$$

$$+ f^j \cdot \left[\, \delta t_{c_u} + \rho_u^j(t_{R_u})/c + \delta t_{\phi_u}{}^j \, \right]$$

$$+ f^k \cdot \left[\, \delta t_{c_i} + \rho_i^k(t_{R_i})/c + \delta t_{\phi_i}{}^k \, \right]$$

$$- f^k \cdot \left[\delta t_{c_u} + \rho_u^k(t_{R_u})/c + \delta t_{\phi_u}^{k} \right]$$

$$+ \phi^j(t_i) - \phi^k(t_i) - \phi^j(t_u) + \phi^k(t_u)$$

$$+ N_{iu}^{jk} \qquad\qquad (4.2.14)$$

where $N_{iu}^{jk} = N_i^j(t_{0i}) - N_u^j(t_{0u}) - N_i^k(t_{0i}) + N_u^k(t_{0u})$. In Eq. (4.2.14), all the phase terms associated with the ground station and user satellite receivers are canceled out.

By multiplying a negative nominal wave length, $-\lambda = -c/f_0$, Eq. (4.2.14) becomes the double-differenced high-low phase pseudorange measurement,

$$DDHL_{iu}^{c\,jk} = \left(\frac{f^j}{f_0}\right) \cdot \left(\rho_i^j(t_{R_i}) - \rho_u^j(t_{R_u})\right) - \left(\frac{f^k}{f_0}\right) \cdot \left(\rho_i^k(t_{R_i}) - \rho_u^k(t_{R_u})\right)$$

$$- \left(\frac{c}{f_0}\right) \cdot \left(\phi^j(t_i) - \phi^k(t_i) - \phi^j(t_u) + \phi^k(t_u)\right)$$

$$+ c \cdot \left(\frac{f^j - f^k}{f_0}\right) \cdot (\delta t_{c_i} - \delta t_{c_u})$$

$$+ \left(\frac{f^j}{f_0}\right) \cdot (\delta\rho_{\phi_i}^j - \delta\rho_{\phi_u}^j) - \left(\frac{f^k}{f_0}\right) \cdot (\delta\rho_{\phi_i}^k - \delta\rho_{\phi_u}^k)$$

$$+ C_{iu}^{jk} \qquad\qquad (4.2.15)$$

where $\delta\rho_\phi = -c \cdot \delta t_\phi$, and $C_{iu}^{jk} = -\lambda \cdot N_{iu}^{jk}$. Note that Eq. (4.2.15) contains two different time tags, t_i and t_u. If the ground station receiver clock and the on-board receiver clock are synchronized, then the second line can be canceled out. Since both the ICESat/GLAS on-board receiver clock and the ground station receiver clock will

be synchronized within 1 microsecond with the GPS System Time, the second line can be canceled out.

Since the GPS satellites have highly stable oscillators, which have 10^{-11} or 10^{-12} clock drift rate, the frequencies of those clocks usually stay close to the nominal frequency, f_0. If the frequencies are expressed as $f^j = f_0 + \Delta f^j$ and $f^k = f_0 + \Delta f^k$, Eq. (4.2.15) becomes

$$DDHL_{iu}^{c\,jk} = \rho_i^j(t_{R_i}) - \rho_u^j(t_{R_u}) - \rho_i^k(t_{R_i}) + \rho_u^k(t_{R_u})$$

$$+ \left(\frac{\Delta f^j}{f_0}\right) \cdot (\rho_i^j(t_{R_i}) - \rho_u^j(t_{R_u})) - \left(\frac{\Delta f^k}{f_0}\right) \cdot (\rho_i^k(t_{R_i}) - \rho_u^k(t_{R_u}))$$

$$+ c \cdot \left(\frac{\Delta f^j - \Delta f^k}{f_0}\right) \cdot (\delta t_{c_i} - \delta t_{c_u})$$

$$+ \delta \rho_{\phi_i}^j - \delta \rho_{\phi_u}^j - \delta \rho_{\phi_i}^k + \delta \rho_{\phi_u}^k$$

$$+ \left(\frac{\Delta f^j}{f_0}\right) \cdot (\delta \rho_{\phi_i}^j - \delta \rho_{\phi_u}^j) - \left(\frac{\Delta f^k}{f_0}\right) \cdot (\delta \rho_{\phi_i}^k - \delta \rho_{\phi_u}^k)$$

$$+ C_{iu}^{jk} \qquad\qquad\qquad (4.2.16)$$

For the ICESat/GLAS-GPS case, the single differenced range can be 600 km to 6200 km. If we assume 10^{-11} clock drift rate for GPS satellite clocks, the second line contributes an effect, which is at the sub-millimeter level to the double differenced range measurement. This effect is less than the noise level, and as a consequence, the contribution from the second line can be ignored. Since the performance specification of the time-tag errors of the flight and ground receivers for ICESat/GLAS mission is required to be less than 1 microsecond with respect to the

GPS System Time, the third line also is negligible. The fifth line is totally negligible, because even for the propagation delay of 100 m, the contribution from this line is less than 10^{-9} meters. The first line in Eq. (4.2.16) can be expanded by the linear approximation after substituting Eqs. (4.2.4a) and (4.2.4b), to obtain:

$$DDHL^{c\,jk}_{iu} = \rho^{j}_{i}(t_{i}) - \rho^{j}_{u}(t_{u}) - \rho^{k}_{i}(t_{i}) + \rho^{k}_{u}(t_{u})$$

$$- \left[\dot{\rho}^{j}_{i}(t_{i}) - \dot{\rho}^{k}_{i}(t_{i})\right] \cdot \ \delta t_{c_{i}} + \left[\dot{\rho}^{j}_{u}(t_{u}) - \dot{\rho}^{k}_{u}(t_{u})\right] \cdot \ \delta t_{c_{u}}$$

$$+ \ \delta\rho^{j}_{\phi_{i}} - \delta\rho^{j}_{\phi_{u}} - \delta\rho^{k}_{\phi_{i}} + \delta\rho^{k}_{\phi_{u}}$$

$$+ \ C^{jk}_{iu} \tag{4.2.17}$$

This equation is implemented for the double-differenced high-low phase pseudorange measurement. The second line does not need to be computed if the ground stations and the ICESat/GLAS on-board receiver's time-tags are corrected in the preprocessing stage by using independent clock information from the pseudo-range measurement. If such clock information is not available, then the receiver clock errors, $\delta t_{c_{i}}$ and $\delta t_{c_{u}}$, can be modeled as linear functions,

$$\delta t_{c_{i}} = a_{i} + b_{i}\,(t_{i} - t_{i0}) \tag{4.2.18a}$$

$$\delta t_{c_{u}} = a_{u} + b_{u}\,(t_{u} - t_{u0}) \tag{4.2.18b}$$

where (a_{i}, b_{i}) and (a_{u}, b_{u}) are pairs of clock bias and clock drift for i-th ground station receiver clock and the user satellite clock, respectively, and t_{i0} and t_{u0} are the reference time for clock parameters for i-th ground station receiver clock and the user satellite clock.

The third line of Eq. (4.2.17) includes the propagation delay and the relativistic effects for the high-low phase converted measurement. These effects are discussed in more detail in the following sections.

4.2.4   Corrections

4.2.4.1   Propagation Delay

When a radio wave is traveling through the atmosphere of the Earth, it experiences a delay due to the propagation refraction. Atmospheric scientists usually divide the atmosphere into four layers: the troposphere, the stratosphere, the mesosphere, and the thermosphere. The troposphere, the lowest layer of the Earth's atmosphere, contains 99% of the atmosphere's water vapor and 90% of the air mass. The tropospheric bending is therefore treated using both dry and wet components. The dry path delay is caused by the atmosphere gas content along the propagated path through the troposphere while the wet path delay is caused by the water vapor content along the same path. Since the tropospheric path delay of a radio wave is frequency independent, this path delay cannot be isolated using multiple frequencies. The tropospheric path delays caused by the dry portion, which accounts for 80% or more of the delay, can be modeled with an accuracy of two to five percent for L-band frequencies [*Atlshuler & Kalaghan*, 1974]. Although the contribution from the wet component is relatively small, it is more difficult to model because surface measurements of water vapor cannot be applied to completely describe the regional variations in the water vapor distribution, especially with respect to horizontal

variation, of the water vapor field. There are several approaches to model the wet component of the tropospheric path delay. One approach is to use one of the empirical atmospheric models based on the measurement of meteorological parameters at the Earth's surface or the altitude profile with radisondes and apply regional modeling. The other approach is to map the water vapor content in various directions directly using devices like water vapor radiometer (WVR). List of references for these approaches can be found in *Tralli et al.* [1988]. A third approach is to solve for tropospheric path delay parameters. Chao's model [*Chao*, 1974], modified Hopfield model [*Goad and Goodman*, 1974; *Remondi*, 1984], or MTT model [*Herring*, 1992] are among several candidates which can be implemented for the tropospheric correction.

The ionosphere is a region of the Earth's upper atmosphere, approximately 100 km to 1000 km above the Earth's surface, where electrons and ions are present in quantities sufficient to affect the propagation of radio waves. The path delay will be proportional to the number of electrons along the slant path between the satellite and the receiver, and the electron density distribution varies with altitude, time of day time of year, solar and geomagnetic activity, and the time within the solar sunspot cycle. The ionospheric path delay depends on the frequency of the radio signal. The ionospheric bending on L1 GPS measurement will vary from about 0.15 m to 50 m [*Clynch and Coco*, 1986]. Some of this delay can be eliminated by ionospheric modeling [for example, *Finn and Matthewman*, 1989]. However, more accurate corrections can be made by using the dual frequency measurements routinely acquired by the GPS receivers. The correction method for the dual frequency GPS

measurements can be found in Section 6.5.2. *Hofmann-Wellenhof et al.* [1992] provides more detailed description of the propagation delay for GPS measurements.

4.2.4.2 Relativistic Effect

The relativistic effects on GPS measurements can be summarized as follows. Due to the difference in the gravitational potential, the satellite clock tends to run faster than the ground station's [*Spilker*, 1978; *Gibson*, 1983]. These effects can be divided into two parts: a constant drift and a periodic effect. The constant drift can be removed by off-setting the GPS clock frequency low before launch to account for that constant drift. The periodic relativistic effects can be modeled for a high-low measurement as

$$\Delta \rho_{srel} = \frac{2}{c} (\bar{r}_l \cdot \bar{v}_l - \bar{r}_h \cdot \bar{v}_h) \qquad (4.2.20)$$

where

$\Delta \rho_{srel}$ = correction for the special relativity

c = speed of light

$\bar{r}_l, \bar{v}_l$ = the position and velocity of the low satellite or tracking stations

$\bar{r}_h, \bar{v}_h$ = the position and velocity of the high satellite

The coordinate speed of light is reduced when light passes near a massive body causing a time delay, which can be modeled as [*Holdridge*, 1967]

$$\Delta \rho_{grel} = (1 + \gamma) \frac{GM_e}{c^2} \ln \left(\frac{r_{tr} + r_{rec} + \rho}{r_{tr} + r_{rec} - \rho} \right) \qquad (4.2.21)$$

where

$\Delta \rho_{grel}$ = correction for the general relativity

γ = the parameterized post-Newtonian (PPN) parameter (γ = 1 for general relativity)

GM_e = gravitational constant for the Earth

ρ = the relativistically uncorrected range between the transmitter and the receiver

r_{tr} = the geocentric radial distance of the transmitter

r_{rec} = the geocentric radial distance of the receiver

4.2.4.3   Phase Center Offset

The geometric offset between the transmitter and receiver phase centers and the effective satellite body-fixed reference point can be modeled depending on the satellite orientation (attitude) and spacecraft geometry. The ICESat/GLAS antenna location will be known and implemented when the fabrication of the satellite is complete. However, the location of the antenna phase center with respect to the spacecraft center of mass will also be required. This position vector will be essentially constant in spacecraft fixed axes, but this correction is necessary since the equations of motion refer to the spacecraft center of mass.

4.2.4.4   Ground Station Related Effects

In computing the double-differenced phase-converted high-low pseudo-range measurement, it is necessary to consider the effects of the displacement of the ground station location caused by the crustal motions. Among these effects, tidal effects and tectonic plate motion effects are most prominent.

Station displacements arising from tidal effects can be divided into three parts,

$$\Delta_{tide} \;=\; \Delta_{dtide} + \Delta_{ocean} + \Delta_{rotate} \tag{4.2.22}$$

where

Δ_{tide}	= the total displacement due to the tidal effects
Δ_{dtide}	= the displacement due to the solid Earth tide
Δ_{ocean}	= the displacement due to the ocean loading
Δ_{rotate}	= the displacement due to the rotational deformation

The approach of the IERS Conventions [*McCarthy*, 1996] have been implemented for the solid Earth tide correction. Ocean loading effects are due to the elastic response of the Earth's crust to loading induced by the ocean tides. The displacement due to the rotational deformation is the displacement of the ground station by the elastic response of the Earth's crust to shifts in the spin axis orientation [*Goad*, 1980] which occur at both tidal and non-tidal periods. Detailed models for the effects of solid Earth tide, the ocean loading, and the rotational deformation, can be found in *Yuan* [1991].

The effect of the tectonic plate motion, which is based on the relative plate motion model AM0-2 of *Minster and Jordan* [1978], is modeled as

$$\overline{\Delta}_{tect} = (\overline{\omega}_p \times \overline{R}_{s_0})(t_i - t_0) \tag{4.2.23}$$

where

$\overline{\Delta}_{tect}$	= the displacement due to the tectonic motion
$\overline{\omega}_p$	= the angular velocity of the tectonic plate
$\overline{R}_{s_0}$	= the Earth-fixed coordinates of the station at t_i

t_0 = a reference epoch

4.2.5   Measurement Model Partial Derivatives

The partial derivatives of Eq. (4.2.18) with respect to various model parameters are given in this section.   The considered parameters include the ground station positions, GPS satellite's positions, ICESat's positions, clock parameters, ambiguity parameters, and tropospheric refraction parameters.

The partial derivatives of Eq. (4.2.18) with respect to the i-th ground station positions, (x_{1i}, x_{2i}, x_{3i}), are

$$\frac{\partial DDHL^{c\,jk}_{iu}}{\partial x_{mi}} = \frac{(x_{mi} - x_m^{\,j})}{\rho_i^{\,j}} - \frac{(x_{mi} - x_m^{\,k})}{\rho_i^{\,k}}, \qquad \text{for } m=1,2,3 \qquad (4.2.24)$$

where $\rho_i^{\,j}$ is the range between i-th ground station receiver and j-th transmitter, and $\rho_i^{\,k}$ is the range between i-th ground station receiver and k-th transmitter such that

$$\rho_i^{\,j} = \sqrt{(x_{1i} - x_1^{\,j})^2 + (x_{2i} - x_2^{\,j})^2 + (x_{3i} - x_3^{\,j})^2} \qquad (4.2.25)$$

$$\rho_i^{\,k} = \sqrt{(x_{1i} - x_1^{\,k})^2 + (x_{2i} - x_2^{\,k})^2 + (x_{3i} - x_3^{\,k})^2} \qquad (4.2.26)$$

and $(x_1^{\,j}, x_2^{\,j}, x_3^{\,j})$ and $(x_1^{\,k}, x_2^{\,k}, x_3^{\,k})$ are the j-th and k-th transmitter Cartesian positions, respectively.

The partial derivatives of Eq. (4.2.18) with respect to the j-th and k-th transmitter positions are

$$\frac{\partial DDHL_{iu}^{c\,jk}}{\partial x_m{}^j} = \frac{(x_{mi} - x_m{}^j)}{\rho_i^j} + \frac{(x_{mu} - x_m{}^j)}{\rho_u^j}, \qquad \text{for } m\text{=1,2,3} \qquad (4.2.27)$$

$$\frac{\partial DDHL_{iu}^{c\,jk}}{\partial x_m{}^k} = \frac{(x_{mi} - x_m{}^k)}{\rho_i^k} - \frac{(x_{mu} - x_m{}^k)}{\rho_u^k}, \qquad \text{for } m\text{=1,2,3} \qquad (4.2.28)$$

where ρ_u^j is the range between j-th transmitter and the user satellite, and ρ_u^k is the range between k-th transmitter and the user satellite such that

$$\rho_u^j = \sqrt{(x_{1u} - x_1{}^j)^2 + (x_{2u} - x_2{}^j)^2 + (x_{3u} - x_3{}^j)^2} \qquad (4.2.29)$$

$$\rho_u^k = \sqrt{(x_{1u} - x_1{}^k)^2 + (x_{2u} - x_2{}^k)^2 + (x_{3u} - x_3{}^k)^2} \qquad (4.2.30)$$

and (x_{1u}, x_{2u}, x_{3u}) are the user satellite's Cartesian positions.

The partial derivatives of Eq. (4.2.18) with respect to the user satellite positions are

$$\frac{\partial DDHL_{iu}^{c\,jk}}{\partial x_{mu}} = -\frac{(x_{mu} - x_m{}^j)}{\rho_u^j} + \frac{(x_{mu} - x_m{}^k)}{\rho_u^k}, \qquad \text{for } m\text{=1,2,3} \qquad (4.2.31)$$

The partial derivatives of Eq. (4.2.18) with respect to the clock parameters of Eqs. (4.2.19a) and (4.2.19b) are

$$\frac{\partial DDHL_{iu}^{c\,jk}}{\partial a_i} = -(\dot{\rho}_i^j - \dot{\rho}_i^k) \qquad (4.2.32)$$

$$\frac{\partial DDHL_{iu}^{c\,jk}}{\partial b_i} = -(\dot{\rho}_i^j - \dot{\rho}_i^k) \cdot (t_i - t_{i0}) \qquad (4.2.33)$$

and

$$\frac{\partial DDHL_{iu}^{c\,jk}}{\partial a_u} = (\dot{\rho}_u^j - \dot{\rho}_u^k) \tag{4.2.34}$$

$$\frac{\partial DDHL_{iu}^{c\,jk}}{\partial b_u} = (\dot{\rho}_u^j - \dot{\rho}_u^k) \cdot (t_u - t_{u0}) \tag{4.2.35}$$

The partial derivative of Eq. (4.2.18) for the double-differenced ambiguity parameter, C_{iu}^{jk}, is

$$\frac{\partial DDHL_{iu}^{c\,jk}}{\partial C_{iu}^{jk}} = 1 \tag{4.2.36}$$

When Chao's model is used, the partial derivative of Eq. (4.2.18) with respect to the i-th ground station's zenith delay parameter, Z_i, is

$$\frac{\partial DDHL_{iu}^{c\,jk}}{\partial Z_i} = \left(\frac{1}{\sin E_i^{\ j} + \dfrac{0.00143}{\tan E_i^{\ j} + 0.0445}} + \frac{1}{\sin E_i^{\ j} + \dfrac{0.00035}{\tan E_i^{\ j} + 0.017}} \right)$$

$$- \left(\frac{1}{\sin E_i^{\ k} + \dfrac{0.00143}{\tan E_i^{\ k} + 0.0445}} + \frac{1}{\sin E_i^{\ k} + \dfrac{0.00035}{\tan E_i^{\ k} + 0.017}} \right)$$

$$\tag{4.2.37}$$

where $E_i^{\ j}$ and $E_i^{\ k}$ are the elevation angles of the j-th and k-th GPS satellite transmitters from i-th ground station, respectively.

4.3   SLR Measurement Model

4.3.1   Range Model and Corrections

Laser tracking instruments record the travel time of a short laser pulse from the reference point (opticalaxis) to the satellite retroreflector and back. The one-way range from the reference point of the ranging instrument to the retroreflector of the satellite, ρ^o, can be expressed in terms of the round trip light time, $\Delta\tau$ as

$$\rho^o = \frac{1}{2}c\Delta\tau + \varepsilon \tag{4.3.1}$$

where

c = the speed of light

ε = measurement error.

The computed one-way signal path between the reference point on the satellite and the ground station, ρ^c, can be expressed as

$$\rho^c = |\bar{r} - \bar{r}_s| + \Delta\rho_{trop} + \Delta\rho_{grel} + \Delta\rho_{c.m.} \tag{4.3.2}$$

where

$\bar{r}$ = the satellite position in geocentric coordinates

$\bar{r}_s$ = the position of the tracking station in geocentric coordinates

$\Delta\rho_{trop}$ = correction for tropospheric delay

$\Delta\rho_{grel}$ = correction for the general relativity

$\Delta\rho_{c.m.}$ = correction for the offset of the satellite's center-of-mass and the

              laser retroreflector

The tropospheric refraction correction is computed using the model of *Marini and Murray* [1973]. The correction for the general relativity in SLR measurements is the

same as for GPS measurement, which is expressed in Eq. (4.2.21). The effects of the displacement of the ground station location caused by the crustal motions should be considered. These crustal motions include tidal effects and tectonic plate motion effects, which are described in Eqs. (4.2.22) and (4.2.23), respectively.

4.3.2 Measurement Model Partial Derivatives

The partial derivatives of Eq. (4.3.2) with respect to various model parameters are derived in this section. The considered parameters include the ground station positions, satellite's positions.

The partial derivatives of Eq. (4.3.2) with respect to the ground station positions, (r_{s1}, r_{s2}, r_{s3}), are

$$\frac{\partial \rho^c}{\partial r_{si}} = \frac{(r_{si} - r_i)}{\rho}, \qquad \text{for } i=1,2,3 \qquad (4.3.3)$$

where (r_1, r_2, r_3) are the satellite's positions, and ρ is the range between the ground station and the satellite such that

$$\rho = \sqrt{(r_1 - r_{s1})^2 + (r_2 - r_{s2})^2 + (r_3 - r_{s3})^2} \qquad (4.3.4)$$

The partial derivatives of Eq. (4.3.2) with respect to the satellite's positions, (r_1, r_2, r_3), are

$$\frac{\partial \rho^c}{\partial r_i} = \frac{(r_i - r_{si})}{\rho}, \qquad \text{for } i=1,2,3 \qquad (4.3.5)$$

5.0   ALGORITHM DESCRIPTION: Estimation

A least squares batch filter [*Tapley*, 1973] is our adopted approach for the estimation procedure.   Since multi-satellite orbit determination problems require extensive usage of computer memory for computation, it is essential to consider the computational efficiency in the problem formulation.   This section describes the estimation procedures for ICESat/GLAS POD, including the problem formulation for multi-satellite orbit determination.

5.1   Least Squares Estimation

The equations of motion for the satellite can be expressed as

$$\dot{X}(t) = F(X,t), \qquad\qquad X(t_0) = X_0 \qquad\qquad (5.1.1)$$

where X is the n-dimensional state vector, F is a non-linear n-dimensional vector function of the state, and X_0 is the value of the state at the initial time t_0, which is not known perfectly.   The tracking observations can be expressed as discrete measurements of quantities, which are a function of the state. Thus the observation-state relationship can be written as

$$Y_i = G(X_i, t_i) + \varepsilon_i \qquad\qquad i = 1, \ldots, l \qquad\qquad (5.1.2)$$

where Y_i is a p vector of the observations made at time t_i, (X_i, t_i) is a non-linear vector function relating the state to the observations, and ε_i is the measurement noise.

If a reference trajectory is available and if X, the true trajectory, and X^*, the reference trajectory, remain sufficiently close throughout the time interval of interest, the trajectory for the actual motion can be expanded in a Taylor series about

the reference trajectory to obtain a set of differential equations with time dependent coefficients. Using a similar procedure to expand the nonlinear observation-state relation, a linear relation between the observation deviation and the state deviation can be obtained. Then, the nonlinear orbit determination problem can be replaced by a linear orbit determination problem in which the deviation from the reference trajectory is to be determined. In practice, this linearization of the problem requires an iterative adjustment which yields successively smaller adjustments to the state parameters to optimally fit the observations.

Let

$$x(t) = X(t) - X^*(t) \qquad\qquad y(t) = Y(t) - Y^*(t) \qquad\qquad (5.1.3)$$

where $X^*(t)$ is a specified reference trajectory and $Y^*(t)$ is the value of the observation calculated by using $X^*(t)$. Then, substituting Eq. (5.1.3) into Eqs. (5.1.1) and (5.1.2), expanding in a Taylor's series, and neglecting higher order terms leads to the relations

$$\dot{x} = A(t)x, \qquad\qquad x(t_0) = x_0$$

$$y_i = \widetilde{H}_i x_i + \varepsilon_i \qquad\qquad i = 1,\dots,l \qquad\qquad (5.1.4)$$

where

$$A(t) = \frac{\partial F}{\partial X}(X^*, t) \qquad\qquad \widetilde{H} = \frac{\partial G}{\partial X}(X^*, t) \qquad\qquad (5.1.5)$$

The general solution to Eq. (5.1.4) can be expressed as

$$x(t) = \Phi(t,t_0)x_0 \qquad\qquad (5.1.6)$$

where the state transition matrix $\Phi(t,t_0)$ satisfies the differential equation:

$$\dot{\Phi}(t,t_0) = A(t)\Phi(t,t_0), \qquad \Phi(t_0,t_0) = I \qquad\qquad (5.1.7)$$

where I is the $n \times n$ identity matrix.

Using Eq. (5.1.5), the second of Eq. (5.1.3) may be written in terms of the state at t_0 as

$$y_i = \tilde{H}_i\Phi(t_i,t_0)x_0 + \varepsilon_i, \qquad i = 1,\ldots,l \qquad\qquad (5.1.8)$$

Using the solution for the linearized state equation (Eq. (5.1.6)), Eq. (5.1.8) may be rewritten as

$$y = Hx_0 + \varepsilon \qquad\qquad (5.1.9)$$

where

$$y = \begin{bmatrix} y_1 \\ \vdots \\ y_l \end{bmatrix} \qquad H = \begin{bmatrix} \tilde{H}_1\Phi(t_1,t_0) \\ \vdots \\ \tilde{H}_l\Phi(t_l,t_0) \end{bmatrix} \qquad \varepsilon = \begin{bmatrix} \varepsilon_1 \\ \vdots \\ \varepsilon_l \end{bmatrix} \qquad\qquad (5.1.10)$$

where y and ε are m vectors ($m = l \times p$) and H is an $m \times n$ matrix. Equation (5.1.9) is a system of m equations in n unknowns. In practical orbit determination problems, there are more observations than estimated parameters ($m > n$), which means that Eq. (5.1.9) is overdetermined. It is usually assumed that the observation error vector, ε, satisfies the a priori statistics, $E[\varepsilon] = 0$ and $E[\varepsilon\varepsilon^T] = W^{-1}$. By scaling each term in Eq. (5.1.9) by $W^{1/2}$, the condition

$$W^{1/2}[\varepsilon\varepsilon^T]W^{T/2} = W^{1/2}W^{-1}W^{T/2} = I \qquad\qquad (5.1.11)$$

is obtained.

An approach to obtain the best estimate of $\widehat{x}$, given the linear observation-state relations (Eq. (5.1.9)) is described in the following discussions. The method obtains the solution by applying successive orthogonal transformations to the linear equations given in Eq. (5.1.9). Consider the quadratic performance index

$$J = \frac{1}{2}\left| W^{1/2}(Hx - y) \right|^2 = \frac{1}{2}(Hx - y)^T W(Hx - y) \tag{5.1.12}$$

The solution to the weighted least-squares estimation problem (which is equivalent to the minimum variance and the maximum likelihood estimation problem, under certain restrictions) is obtained by finding the value $\widehat{x}$ which minimizes Eq. (5.1.12). To achieve the minimum value of Eq. (5.1.12) let Q be an m×m orthogonal matrix. Hence, it follows that Eq. (5.1.12) can be expressed as

$$J = \frac{1}{2}\left| QW^{1/2}(Hx - y) \right|^2 \tag{5.1.13}$$

Now, if Q is selected such that

$$QW^{1/2}H = \begin{bmatrix} R \\ 0 \end{bmatrix} \qquad QW^{1/2}y = \begin{bmatrix} b \\ e \end{bmatrix} \tag{5.1.14}$$

where R is n×n upper-triangular, 0 is an (m-n)×n null matrix, b is n×1 vector, and e is an (m-n)×1 vector. Equation (5.1.13) can be written then as

$$J(x) = \frac{1}{2}\left| Rx - b \right|^2 + \frac{1}{2}\left| e \right|^2 \tag{5.1.15}$$

The value of x, which minimizes Eq. (5.1.12), is obtained by the solution

$$R\widehat{x} = b \tag{5.1.16}$$

and the minimum value of the performance index becomes

$$J(\widehat{x}) = \frac{1}{2}\left| e \right|^2 = \frac{1}{2}\left| y - H\widehat{x} \right|^2 \tag{5.1.17}$$

That is, e provides an estimate of the residual error vector.

The procedures are direct and for implementation requires only that a convenient computational procedure for computing $QW^{1/2}H$ and $QW^{1/2}y$ be available. The two most frequently applied methods are the Givens method, based on a sequence of orthogonal rotations, and the Householder method, based on a series of orthogonal reflections [*Lawson and Hanson*, 1974].

In addition to the expression for computing the estimate, the statistical properties of the error in the estimate, R, are required. If the error in the estimate, η, is defined as

$$\eta = \hat{x} - x \tag{5.1.18}$$

it follows that

$$E[\eta] = E[\hat{x} - x] = E[R^{-1}b - x] \tag{5.1.19}$$

Since

$$QW^{1/2}y = QW^{1/2}Hx + QW^{1/2}\varepsilon$$

leads to

$$b = Rx + \tilde{\varepsilon} \tag{5.1.20}$$

it follows that

$$E[\eta] = E[R^{-1}(Rx + \tilde{\varepsilon}) - x] = E[R^{-1}\tilde{\varepsilon}] \tag{5.1.21}$$

As noted in Eq. (5.1.11), if the observation error, ε, is unbiased, $\tilde{\varepsilon} = QW^{1/2}\varepsilon$ will be unbiased and

$$E[\eta] = 0 \tag{5.1.22}$$

Hence, $\hat{x}$ will be an unbiased estimate of x. Similarly, the covariance matrix for the error in x can be expressed as

$$P = E[\eta \eta^T]$$

$$= E[R^{-1}\widetilde{\varepsilon}\widetilde{\varepsilon}^T R^{-T}] = R^{-1}E[\widetilde{\varepsilon}\widetilde{\varepsilon}^T]R^{-T} \qquad (5.1.23)$$

If the observation error, ε, has a statistical covariance defined as $E[\varepsilon\varepsilon^T] = W^{-1}$, the estimation error covariance matrix is given by $E[\widetilde{\varepsilon}\widetilde{\varepsilon}^T] = W^{1/2}E[\varepsilon\varepsilon^T]W^{T/2} = W^{1/2}W^{-1}W^{T/2} = I$. Consequently, relation (5.1.23) leads to

$$P = R^{-1}R^{-T} \qquad (5.1.24)$$

It follows then that the estimate of the state and the associated error covariance matrix are given by the expressions

$$\hat{x} = R^{-1}b \qquad (5.1.25)$$

$$P = R^{-1}R^{-T} \qquad (5.1.26)$$

5.2   Problem Formulation for Multi-Satellite Orbit Determination

Proper categorization of the parameters will help to clarify the problem formulation. Parameters can be divided into two groups: dynamic parameters and kinematic parameters. Dynamic parameters need to be mapped into other states by using the state transition matrix, which is usually computed by numerical integration, while kinematic parameters are treated as constant throughout the computation. Dynamic parameters can be grouped again into two parts as the local dynamic

parameters and global dynamic parameters. Local dynamic parameters are satellite-specific. Global dynamic parameters are parameters, which influence every satellite, such as those defining gravitational forces.

Following the categorization described above, the estimation state vector is defined as

$$
X \equiv \begin{bmatrix} X_{KP} \\ X_{SS} \\ X_{LDP} \\ X_{GDP} \end{bmatrix} \tag{5.2.1}
$$

where

X_{KP} = the kinematic parameters (n_{kp})

X_{SS} = the satellite states (n_{ss})

X_{LDP} = the local dynamic parameters (n_{ldp})

X_{GDP} = the global dynamic parameters (n_{gdp})

and X_{SS} consists of satellites' positions and velocities, i.e. $X_{SS} \equiv [X_{POS}, X_{VEL}]^T$. For ns-satellites, where ns is the total number of satellites which will be estimated, X_{SS} becomes

$$
X_{ss} = \begin{bmatrix} \bar{r}_1 \\ \vdots \\ \bar{r}_{ns} \\ \cdots \\ \bar{v}_1 \\ \vdots \\ \bar{v}_{ns} \end{bmatrix}
$$

where $\bar{r}_i$ and $\bar{v}_i$ are the 3×1 position and velocity vectors of the i-th satellite, respectively.

The differential equations of state, Eq. (5.1.1), becomes

$$\dot{X}(t) = F(X,t) = \begin{bmatrix} 0 \\ \dot{X}_{SS} \\ 0 \\ 0 \end{bmatrix}, \qquad X(t_0) = X_0 \tag{5.2.2}$$

where

$$\dot{X}_{ss} = \begin{bmatrix} \bar{v}_1 \\ \vdots \\ \bar{v}_{ns} \\ \cdots \\ \bar{f}_1 \\ \vdots \\ \bar{f}_{ns} \end{bmatrix} \tag{5.2.3}$$

and $\bar{f}_i = \bar{a}_{g_i} + \bar{a}_{ng_i}$ for i-th satellite. Eq. (5.2.2) represent a system of n nonlinear first order differential equations which includes $n_{ss} = 6 \times ns$ of Eq. (5.2.3). After the linearization process described in section 5.1, Eq. (5.2.2) becomes Eqs. (5.1.6) and (5.1.7).

Since Eq. (5.1.7) represents n^2 coupled first order ordinary differential equations, the dimension of the integration vector becomes $n_{ss} + n^2$. However, $A(t)$ matrix is a sparse matrix, because of the nature of the parameters. And $A(t)$ matrix becomes

even sparser, since each satellite's state is independent of the others, i.e. $(\bar{r}_i, \bar{v}_i)$ is independent of $(\bar{r}_j, \bar{v}_j)$ for $i \neq j$. Using the partitioning of Eq. (5.2.1), $A(t)$ becomes

$$A = \begin{bmatrix} 0 & 0 & 0 & 0 & 0 \\ 0 & 0 & I & 0 & 0 \\ 0 & A_{32} & A_{33} & A_{34} & A_{35} \\ 0 & 0 & 0 & 0 & 0 \\ 0 & 0 & 0 & 0 & 0 \end{bmatrix} \tag{5.2.4}$$

where

$$A_{32} = \begin{bmatrix} \dfrac{\partial \bar{f}_1}{\partial \bar{r}_1} & \cdots 0 \cdots & \cdots 0 \\ \vdots & & \vdots \\ 0 & \ddots & 0 \\ \vdots & & \vdots \\ 0 & \cdots 0 \cdots & \dfrac{\partial \bar{f}_{ns}}{\partial \bar{r}_{ns}} \end{bmatrix} \qquad A_{33} = \begin{bmatrix} \dfrac{\partial \bar{f}_1}{\partial \bar{v}_1} & \cdots 0 \cdots & \cdots 0 \\ \vdots & & \vdots \\ 0 & \ddots & 0 \\ \vdots & & \vdots \\ 0 & \cdots 0 \cdots & \dfrac{\partial \bar{f}_{ns}}{\partial \bar{v}_{ns}} \end{bmatrix}$$

$$A_{34} = \begin{bmatrix} \dfrac{\partial \bar{f}_1}{\partial X_{LDP_1}} & \cdots 0 \cdots & \cdots 0 \\ \vdots & & \vdots \\ 0 & \ddots & 0 \\ \vdots & & \vdots \\ 0 & \cdots 0 \cdots & \dfrac{\partial \bar{f}_{ns}}{\partial X_{LDP_{ns}}} \end{bmatrix} \qquad A_{35} = \begin{bmatrix} \dfrac{\partial \bar{f}_1}{\partial X_{GDP_1}} \\ \vdots \\ \dfrac{\partial \bar{f}_{ns}}{\partial X_{GDP_{ns}}} \end{bmatrix}$$

Note that A_{32}, A_{33}, and A_{34} are all block diagonal matrix, and A_{33} would be zero if the perturbations do not depend on satellites' velocity. Atmospheric drag is one example of perturbations, which depend on the satellite's velocity.

If $\Phi = [\phi_{ij}]$, for $i, j = 1, \cdots, 5$, Eq. (5.1.7) becomes

$$\dot{\Phi} = \begin{bmatrix} 0 & 0 & 0 & 0 & 0 \\ \phi_{31} & \phi_{32} & \phi_{33} & \phi_{34} & \phi_{35} \\ B_{11} & B_{12} & B_{13} & B_{14} & B_{15} \\ 0 & 0 & 0 & 0 & 0 \\ 0 & 0 & 0 & 0 & 0 \end{bmatrix} \tag{5.2.5}$$

where $\quad B_{1j} = A_{32}\phi_{2j} + A_{33}\phi_{3j} + A_{34}\phi_{4j} + A_{35}\phi_{5j} \quad$ for $j = 1,\cdots, 5$.

Integrating the first row and last two rows of Eq. (5.2.4) with the initial conditions, $\Phi(t_0,t_0) = I$ yields the results that $\phi_{11}=\phi_{44}=\phi_{55}=I$ and $\phi_{12}=\phi_{13}=\phi_{14}=\phi_{15}=\phi_{41}=\phi_{42}=\phi_{43}=\phi_{45}=\phi_{51}=\phi_{52}=\phi_{53}=\phi_{54}=0$. After substituting these results to $B_{1j}, j=1,\cdots,5$, we have

$$B_{11} = A_{32}\phi_{21} + A_{33}\phi_{31}$$

$$B_{12} = A_{32}\phi_{22} + A_{33}\phi_{32}$$

$$B_{13} = A_{32}\phi_{23} + A_{33}\phi_{33} \tag{5.2.6}$$

$$B_{14} = A_{32}\phi_{24} + A_{33}\phi_{34} + A_{34}$$

$$B_{15} = A_{32}\phi_{25} + A_{33}\phi_{35} + A_{35}$$

From Eq. (5.2.5) and Eq. (5.2.6), we have

$$\dot{\phi}_{21} = \phi_{31} \tag{5.2.7a}$$

$$\dot{\phi}_{22} = \phi_{32} \tag{5.2.8a}$$

$$\dot{\phi}_{23} = \phi_{33} \tag{5.2.9a}$$

$$\dot{\phi}_{24} = \phi_{34} \tag{5.2.10a}$$

$$\dot{\phi}_{25} = \phi_{35} \tag{5.2.11a}$$

$$\dot{\phi}_{31} = A_{32}\phi_{21} + A_{33}\phi_{31} \tag{5.2.7b}$$

$$\dot{\phi}_{32} = A_{32}\phi_{22} + A_{33}\phi_{32} \tag{5.2.8b}$$

$$\dot{\phi}_{33} = A_{32}\phi_{23} + A_{33}\phi_{33} \tag{5.2.9b}$$

$$\dot{\phi}_{34} = A_{32}\phi_{24} + A_{33}\phi_{34} + A_{34} \tag{5.2.10b}$$

$$\dot{\phi}_{35} = A_{32}\phi_{25} + A_{33}\phi_{35} + A_{35} \tag{5.2.11b}$$

From Eqs. (5.2.7a) and (5.2.7b)

$$\ddot{\phi}_{21} - A_{33}\dot{\phi}_{21} - A_{32}\phi_{21} = 0, \qquad \phi_{21}(0) = 0 \quad \dot{\phi}_{21}(0) = 0 \tag{5.2.12}$$

If we define the partials of accelerations with respect to each group of parameters for the i-th satellite as follows,

$$\frac{\partial \bar{f}_i}{\partial \bar{r}_i} \equiv DADR_i \tag{5.2.13a}$$

$$\frac{\partial \bar{f}_i}{\partial \bar{v}_i} \equiv DADV_i \tag{5.2.13b}$$

$$\frac{\partial \bar{f}_i}{\partial X_{LDP_i}} \equiv DLDP_i \qquad\qquad\qquad (5.2.13c)$$

$$\frac{\partial \bar{f}_i}{\partial X_{GDP_i}} \equiv DGDP_i \qquad\qquad\qquad (5.2.13d)$$

and ϕ_{21} is partitioned as $\phi_{21} = \left[\phi_{21_1}, \cdots, \phi_{21_{ns}}\right]^T$ by $3 \times n_{kp}$ submatrix, ϕ_{21_i}, then, Eq. (5.2.12) become

$$\ddot{\phi}_{21_i} - DADV_i\, \dot{\phi}_{21_i} - DADR_i\, \phi_{21_i} = 0, \qquad i = 1, \cdots, ns \qquad (5.2.14)$$

After applying the initial conditions, $\phi_{21_i}(0) = 0$ and $\dot{\phi}_{21_i}(0) = 0$, to Eq. (5.2.14), we have $\phi_{21} = 0$. And from Eq. (5.2.7a) $\phi_{31} = 0$. From Eqs. (5.2.8a) and (5.2.8b), and Eqs. (5.2.9a) and (5.2.9b), we have similar results as follows.

$$\ddot{\phi}_{22_i} - DADV_i\, \dot{\phi}_{22_i} - DADR_i\, \phi_{22_i} = 0, \qquad i = 1, \cdots, ns \qquad (5.2.15)$$

$$\ddot{\phi}_{23_i} - DADV_i\, \dot{\phi}_{23_i} - DADR_i\, \phi_{23_i} = 0, \qquad i = 1, \cdots, ns \qquad (5.2.16)$$

with the initial conditions $\phi_{22_i}(0) = I$, $\dot{\phi}_{22_i}(0) = 0$, $\phi_{23_i}(0) = 0$, and $\dot{\phi}_{23_i}(0) = I$ for $i = 1, \cdots, ns$.

From Eqs. (5.2.10a) and (5.2.10b), we have

$$\ddot{\phi}_{24} - A_{33}\, \dot{\phi}_{24} - A_{32}\, \phi_{24} = A_{34}, \qquad \phi_{24}(0) = 0 \quad \dot{\phi}_{24}(0) = 0 \qquad (5.2.17)$$

If ϕ_{24} is partitioned as $\phi_{24} = \left[\phi_{24_1}, \cdots, \phi_{24_{ns}} \right]^T$ with $3 \times n_{ldp_i}$ submatrix, where n_{ldp_i} is

the i-th satellite's number of local dynamic parameters, then it can be shown that all

the off-block diagonal terms become zero and the above equation becomes,

$$\ddot{\phi}_{24_i} - DADV_i \; \dot{\phi}_{24_i} - DADR_i \; \phi_{24_i} = DLDP_i, \qquad i = 1, \cdots, ns \qquad (5.2.18)$$

with the initial conditions $\phi_{24_i}(0) = 0$ and $\dot{\phi}_{24_i}(0) = 0$ for $i = 1, \cdots, ns$.

From Eqs. (5.2.11a) and (5.2.11b), we have similar results for ϕ_{25}.

$$\ddot{\phi}_{25_i} - DADV_i \; \dot{\phi}_{25_i} - DADR_i \; \phi_{25_i} = DGDP_i, \qquad i = 1, \cdots, ns \qquad (5.2.19)$$

with the initial conditions $\phi_{25_i}(0) = 0$ and $\dot{\phi}_{25_i}(0) = 0$ for $i = 1, \cdots, ns$.

Combining all these results, we have the state transition matrix for multi-satellite problem as follows:

$$\Phi = \begin{pmatrix} 0 & 0 & 0 & 0 & 0 \\ \phi_{21} & \phi_{22} & \phi_{23} & \phi_{24} & \phi_{25} \\ \dot{\phi}_{21} & \dot{\phi}_{22} & \dot{\phi}_{23} & \dot{\phi}_{24} & \dot{\phi}_{25} \\ 0 & 0 & 0 & 0 & 0 \\ 0 & 0 & 0 & 0 & 0 \end{pmatrix} \qquad (5.2.20)$$

where $\phi_{21} = \dot{\phi}_{21} = 0$ and

$$\phi_{22} = \begin{pmatrix} \phi_{22_1} & \cdots & 0 \\ \vdots & \ddots & \vdots \\ 0 & \cdots & \phi_{22_{ns}} \end{pmatrix} \qquad\qquad \phi_{23} = \begin{pmatrix} \phi_{23_1} & \cdots & 0 \\ \vdots & \ddots & \vdots \\ 0 & \cdots & \phi_{23_{ns}} \end{pmatrix}$$

$$\phi_{24} = \begin{bmatrix} \phi_{24_1} & & 0 \\ & \ddots & \\ 0 & & \phi_{24_{ns}} \end{bmatrix} \qquad \phi_{25} = \begin{bmatrix} \phi_{25_1} \\ \vdots \\ \phi_{25_{ns}} \end{bmatrix}$$

By defining ϕ_{r_i} and ϕ_{v_i} for i-th satellite as follows,

$$\phi_{r_i} \equiv \begin{bmatrix} \phi_{22_i} & \phi_{23_i} & \phi_{24_i} & \phi_{25_i} \end{bmatrix} \tag{5.2.21a}$$

$$\dot{\phi}_{v_i} \equiv \begin{bmatrix} \dot{\phi}_{22_i} & \dot{\phi}_{23_i} & \dot{\phi}_{24_i} & \dot{\phi}_{25_i} \end{bmatrix} \tag{5.2.21b}$$

we can compute $\ddot{\phi}_{v_i} = \begin{bmatrix} \ddot{\phi}_{22_i} & \ddot{\phi}_{23_i} & \ddot{\phi}_{24_i} & \ddot{\phi}_{25_i} \end{bmatrix}$ by substituting Eqs. (5.2.15)-(5.2.16) and Eqs. (5.2.18)-(5.2.19).

$$\ddot{\phi}_{v_i} = \begin{bmatrix} DADV_i\, \dot{\phi}_{22_i} + DADR_i\, \phi_{22_i} \\ DADV_i\, \dot{\phi}_{23_i} + DADR_i\, \phi_{23_i} \\ DADV_i\, \dot{\phi}_{24_i} + DADR_i\, \phi_{24_i} + DLDP_i \\ DADV_i\, \dot{\phi}_{25_i} + DADR_i\, \phi_{25_i} + DGDP_i \end{bmatrix}^T \tag{5.2.22}$$

After rearranging this equation, we get

$$\ddot{\phi}_{v_i} = DADV_i\, \dot{\phi}_{v_i} + DADR_i\, \phi_{r_i} + \begin{bmatrix} 0_{3x3} & 0_{3x3} & DLDP_i & DGDP_i \end{bmatrix} \tag{5.2.23}$$

Eq. (5.2.23) represents $3 \times (6+n_{ldp_i}+n_{gdp_i})$ first order differential equations for the i-th satellite. Therefore, the total number of equations for ns satellites becomes $\sum\limits_{i=1}^{ns} 3 \times (6 + n_{ldp_i} + n_{gdp_i})$.

Since multi-satellite orbit determination problem includes different types of satellites in terms of their perturbations and integration step size, a class of satellite is defined as a group of satellites which will use the same size of geopotential perturbation and the same integration order and step size. For l-classes of satellites, the integration vector, X_{INT}, is defined as

$$X_{INT} \equiv \begin{bmatrix} \bar{r}_{11} \\ \vdots \\ \bar{r}_{1\,ns_1} \\ \hline \phi_{\bar{r}_{11}} \\ \vdots \\ \phi_{\bar{r}_{1\,ns_1}} \\ \hline \bar{v}_{11} \\ \vdots \\ \bar{v}_{1\,ns_1} \\ \hline \phi_{\bar{v}_{11}} \\ \vdots \\ \phi_{\bar{v}_{1\,ns_1}} \\ \hline \vdots \\ \hline \bar{r}_{l1} \\ \vdots \\ \bar{r}_{lns_l} \\ \hline \phi_{\bar{r}_{l1}} \\ \vdots \\ \phi_{\bar{r}_{lns_l}} \\ \hline \bar{v}_{l1} \\ \vdots \\ \bar{v}_{lns_l} \\ \hline \phi_{\bar{v}_{l1}} \\ \vdots \\ \phi_{\bar{v}_{lns_l}} \end{bmatrix} \tag{5.2.24}$$

where ns_i is the number of satellites for i-th class, $\bar{r}_{ij}$ and $\bar{v}_{ij}$ are the position and velocity of the j-th satellite of i-th class, respectively. $\phi_{\bar{r}_{ij}}$ is the state transition

matrix for the j-th satellite's positions of i-th class and $\phi_{\overline{v}_{ij}}$ is the state transition matrix for the j-th satellite's velocities of i-th class.

$$
\dot{X}_{INT} =
\begin{bmatrix}
\overline{v}_{11} \\
\vdots \\
\overline{v}_{1ns_1} \\
\hline
\phi_{\overline{v}_{11}} \\
\vdots \\
\phi_{\overline{v}_{1ns_1}} \\
\hline
\overline{f}_{11} \\
\vdots \\
\overline{f}_{1ns_1} \\
\hline
\dot{\phi}_{\overline{v}_{11}} \\
\vdots \\
\dot{\phi}_{\overline{v}_{1ns_1}} \\
\hline
\vdots \\
\hline
\overline{v}_{l1} \\
\vdots \\
\overline{v}_{lns_l} \\
\hline
\phi_{\overline{v}_{l1}} \\
\vdots \\
\phi_{\overline{v}_{lns_l}} \\
\hline
\overline{f}_{l1} \\
\vdots \\
\overline{f}_{lns_l} \\
\hline
\dot{\phi}_{\overline{v}_{l1}} \\
\vdots \\
\dot{\phi}_{\overline{v}_{lns_l}}
\end{bmatrix}
\tag{5.2.25}
$$

Eq. (5.2.25) is numerically integrated using a procedure such as the Krogh-Shampine-Gordon fixed-step fixed-order formulation for second-order differential equations [*Lundberg*, 1981] for each class of satellites. For the ICESat/GLAS-GPS case, two classes of satellites need to be defined. One is for the high satellites, e.g. GPS, and the other is for the low satellite, e.g. ICESat/GLAS.

5.3   Output

Although a large number of parameters are available from the estimation process as given by Eq. (5.2.24), the primary data product required for the generation of other products is the ephemeris of the ICESat/GLAS spacecraft center of mass. This ephemeris will be generated at a specified interval, e.g., 30-sec and will include the following:

> t in GPS time
>
> 3 position components of the spacecraft center of mass in ICRF and ITRF
>
> T_{ICRF}^{ITRF} the 3×3 transformation matrix between ICRF and the ITRF.

The output quantities will be required at times other than those contained in the generated ephemeris file. Interpolation methods, such as those examined by *Engelkemier* [1992] provide the accuracy comparable to the numerical integration accuracy itself. With these parameters the ITRF position vector can be obtained as well by forming the product of the transformation matrix and the position vector in ICRF.

6.0   IMPLEMENTATION CONSIDERATIONS

In this chapter, some considerations for implementing ICESat/GLAS POD algorithms are discussed. Section 6.1 describes the POD software system in which the POD algorithms are implemented, and the necessary input files for the software are defined. Section 6.2 describes the POD products. Section 6.3 describes the ICESat/GLAS orbit and attitude. Section 6.4 discusses the expected ICESat/GLAS orbit accuracy based on simulations. Section 6.5 summarizes the POD processing strategies. Section 6.6 discusses the plans for pre-launch and post-launch POD activities. Section 6.7 considers computational aspects.

6.1   POD Software System

The POD algorithms described in the previous chapters were implemented in a software system, referred to as MSODP1 (Multi-Satellite Orbit Determination Program 1). This software has been developed by the Center for Space Research (CSR), and shares heritage with UTOPIA [*Schutz and Tapley*, 1980a]. This software can process SLR data and Doppler data in addition to GPS pseudo-range and double-differenced carrier phase data. A version of this POD software will be placed under change control at ICESat/GLAS launch. MSODP1 requires input files, some of which define model parameters, and the following section discusses these necessary input files.

6.1.1   Ancillary Inputs

Some model parameters require continual updating through acquisition of input information hosted on various standard anonymous ftp sites. This includes the Earth orientation parameters, x_p, y_p, and UT1, and solar flux data. Other files, which are considered to be static once "tuned" to ICESat/GLAS requirements include the planetary ephemerides, geopotential parameters, and ocean tides parameters,. In addition, information about the spacecraft attitude is required for the box-wing spacecraft model in the computation of non-gravitational forces and to provide the correction for the GPS phase center location with respect to the spacecraft center of mass. The real-time attitude obtained during flight operations is thought to be adequate for this purpose, but it will be checked against the precise attitude during the Verification Phase. Also, the GPS data from the IGS ground network and the ICESat/GLAS receiver, and SLR data from the International Laser Ranging Service (ILRS) are needed.

6.2   POD Products

Two types of POD products will be generated: the Rapid Reference Orbit (RRO) and the operational POD. The former product will be generated within 12-24 hours for primarily internal use of assessing the operational orbit and verification support for mission planning. The operational POD will be generated within 14 days, possibly within 3 days, after accounting for problems identified in RRO (e.g. GPS satellite problems) and problems reported by IGS. This product will be used in

generating the altimetry standard data products, particularly level 1B and level 2 surface elevation products.

6.3   ICESat/GLAS Orbit and Attitude

During the first 30-150 days after launch, the ICESat/GLAS spacecraft will be operated in a calibration orbit, with an 8-day repeat ground-track interval and 94-degree inclination.   At some point during this period to be determined by calibration results, the orbit will be transitioned to a neighboring mission orbit at the same inclination, with a 183-day repeating ground track.   The ICESat/GLAS operational scenarios and orbit parameters are summarized in Table 6.1.

Table 6.1   ICESat/GLAS Orbit Parameters

Mission Phase	Expected Duration (days)	Mean Altitude (km)	Inclina-tion (deg)	Eccen-tricity	Ground Track Repeat Cycle
S/C Checkout	30	600	94	0.001	No requirement
Calibration/ Validation	31-150	600	94	0.0013	8 days/183 days
Polar Mapping	151-1220	600	94	0.0013	183 days with 25 and 8 day sub-cycles

The ICESat/GLAS spacecraft will operate in two attitude modes depending on the angular distance between the orbit plane and the Sun (β' angle). As shown in Figure 1, for low-β' periods, such as that immediately following launch, the so-called "airplane-mode" is in use, with the solar panels perpendicular to the orbit

plane. When the β′ angle exceeds 32 degrees, however a yaw maneuver places the satellite in the "sailboat-mode", with the axis of solar panels now in the orbit plane. While the two attitudes ensure that the solar arrays produce sufficient power year-round for bus and instrument operations, they introduce significantly different atmospheric drag effects due to the difference in cross-sectional area perpendicular to the velocity vector.

6.4   POD Accuracy Assessment

The predicted radial orbit errors based on recent gravity models (e.g., JGM-3 or EGM-96) are 19-36 cm. To reduce the effect of the geopotential model errors on ICESat/GLAS, which is the major source of orbit error for ICESat/GLAS POD, the gravity model improvement effort will be made through gravity tuning. Solar activity is predicted to peak shortly after launch, and decline significantly during the mission. The level of this activity correlates directly with the magnitude of atmospheric drag effects on the satellite. The combinations of high solar flux and low β′ angle at the start of the mission poses special challenges for POD and gravity tuning.

A previous simulation study [*Rim et al.,* 1996] indicated that the ICESat/GLAS POD requirements could be met at 700-km altitude by either the gravity tuning or employing frequent estimation of empirical parameters, such as adjusting one-cycle-per-revolution parameters for every orbital revolution, within the context of a fully dynamic approach. This approach is referred to as a highly parameterized dynamic approach. Because the mission orbit altitude was lowered to

600-km, and the satellite design has been changed since this earlier study, a new in-depth simulation study [*Rim et al*., 1999] was conducted. It also indicates that even at 600-km altitude with maximum solar activity, the 5-cm and 20-cm radial and horizontal ICESat/GLAS orbit determination requirement can be met using this aforementioned gravity tuning and fully dynamical reduction strategy. Table 6.2 summarizes the ICESat/GLAS orbit accuracy based on two geopotential models, pre-tune and post-tune models. The results are based on eight 1-day arcs with three different parameterizations. Those are (A) 1-rev C_d, 6-hour 1cpr TN, (B) 1-rev C_d, 3-hour 1cpr TN, and (C) 1-rev C_d, 1-rev 1cpr TN, where 1-rev C_d indicates solving for drag coefficient for every orbital revolution, and 1cpr TN means solving for one-cycle-per-revolution Transverse and Normal parameters. Note that even the case (C) could not meet the radial orbit determination requirement using the pre-tune geopotential model. This indicates that gravity tuning is necessary to achieve the orbit determination requirement. A factor of three improvement in radial orbit accuracy was achieved for case (A), and a factor of two improvement occurred for case (C) by the post-tune gravity field.

Table 6.2 ICESat/GLAS Orbit Errors (cm)

Case	Pre-Tune				Post-Tune			
	Data	RMS Orbit Errors			Data	RMS Orbit Errors		
	RMS	R	T	N	RMS	R	T	N
A	5.0	15.5	35.2	14.1	1.9	5.2	11.2	5.6
B	3.6	10.3	22.4	11.2	1.7	3.6	10.7	5.4
C	2.3	6.5	12.2	5.9	1.6	3.3	10.1	5.2

6.5   POD Processing Strategy

6.5.1   Assumptions and Issues

Several assumptions were made for the POD processing. We assume: 1) continued operation of IGS GPS network and the SLR network, 2) IGS GPS data is available in RINEX (Receiver Independent Exchange) format, 3) ICESat/GLAS GPS receiver has performance characteristics comparable to the flight TurboRogue, and ICESat/GLAS GPS data are available in RINEX format, and 4) most relevant IGS, SLR and ICESat/GLAS data are available within 24-36 hours. There are several issues for POD processing which include: 1) identification of problem GPS satellites, 2) identification of problems with ground station data, 3) processing arc length, 4) accommodation for orbit maneuvers, and 5) problems associated with expected out-gassing during early mission phase. For a July 2001 launch and the early phases of the mission, orbit maneuvers are expected to occur as frequently as 5 days because of high level of solar activity [*Demarest and Schutz*, 1999]. These maneuvers will not be modeled, but the maneuver times will be utilized to reinitialize the orbit arc length.

6.5.2   GPS Data Preprocessing

The GPS data processing procedure consists of two major steps: data preprocessing and data reduction. The data preprocessing step includes data acquisition, correcting measurement time tags, generating double-differenced observables, and data editing. The GPS data preprocessing system is collectively

75

called TEXGAP (university of TEXas Gps Analysis Program) and implemented on the HP workstation.

The International GPS Service for Geodynamics (IGS) provides GPS data collected from globally distributed GPS tracking sites, which include more than 200 ground stations at present [*IGS*, 1998]. The daily IGS data files are archived in the IGS global data centers in the RINEX format, and the data from selected ground station network will be downloaded to CSR's data archive system. Also, the GPS data from the ICESat/GLAS GPS receiver will be provided by the ICESat Science Investigator Processing System.

The GPS receiver time tag is in error due to the receiver clock error, and the time tag correction, t_r, can be obtained by

$$t_r = \rho/C - \rho_c/C + t_s \tag{6.1}$$

where C is the speed of light, ρ is the pseudorange measurement, ρ_c is the computed range from GPS ephemerides and receiver position, and t_s is the broadcast GPS satellite clock correction.

Double-differencing eliminates common errors, such as the GPS satellite and receiver clock errors, including the Selective Availability (SA) effect. As described in Section 4.2.3, a double-differenced high-low observation consists of a ground station, two GPS satellites, and ICESat/GLAS satellite. A careful selection of double-differenced combination is required to avoid generating dependent data set.

To eliminate the first-order ionospheric effects, the double-differenced carrier phase observables DD_{L1} at L_1 and DD_{L2} at L_2 frequency are combined to form the ionosphere-free observable, DD_{Lc}, as follows:

$$DD_{Lc} = \frac{f_{L1}^2}{f_{L1}^2 - f_{L2}^2} DD_{L1} - \frac{f_{L1}f_{L2}}{f_{L1}^2 - f_{L2}^2} DD_{L2} \tag{6.2}$$

where f_{L1} = 1575.42 MHz and f_{L2} = 1227.60 MHz.

Data editing involves the detection and fixing of the cycle-slips of the carrier phase data, and the editing of data outliers. For editing outliers, a 3σ editing criterion is applied to the double-differenced residual. Cycle-slips are detected by examining the differences between the consecutive data points in the double-differenced residuals and identifying discontinuity. The identified cycle-slips are fixed by using linear extrapolations.

6.5.3 GPS Orbit Determination

ICESat/GLAS POD requires precise GPS ephemerides, and there are two approaches to obtain the precise GPS ephemerides. The first approach is to solve the GPS orbit simultaneously with the ICESat/GLAS orbit, and the second approach is to fix the GPS ephemeris to an independent determination, such as the IGS solutions. For the first approach, standard models described in Table 6.3 will be used for the reference frame and gravitational perturbations for GPS. For the non-gravitational perturbations on GPS, the models described in Section 3.4.5 will be employed. It has been shown for the Topex POD case that adjusting GPS orbits usually resulted better Topex orbit solutions [*Rim et al.*, 1995]. A simulation study [*Rim et al.*, 2000b] indicates that fixing GPS orbits to high accuracy solutions would generate reasonably well-tuned gravity field, thereby, the POD accuracy requirement could be met with fixing GPS approach. As the accuracy of IGS solutions improved significantly [*Kouba et al.*, 1998], fixing GPS ephemeris to IGS solutions would be a preferred approach for ICESat/GLAS POD. These two approaches will be evaluated using available tracking data during the pre-launch period, such as CHAMP and JASON,

and ICESat/GLAS tracking data during the verification/validation period. CHAMP POD accuracy was assessed when the GPS ephemeris is fixed to IGS solutions, such as the ultra-rapid, rapid, and final solutions [*Rim et al*., 2002a]

6.5.4   Estimation Strategy

The adopted estimation strategy for ICESat/GLAS POD is the dynamic approach with tuning of model parameters, especially the geopotential parameters. Simulation studies indicate that frequent estimation of empirical parameters is an effective way of reducing orbit errors. The solutions from the sequential filter with process-noise will be investigated as a validation tool for the highly parameterized dynamic solutions. Results of *Davis* [1996] and *Rim et al*. [2000a] show that both highly parameterized dynamic approach with gravity tuning and the reduced-dynamic approach yield comparable results in high fidelity simulations. This comparison will continue with the flight data.

6.6   POD Plans

This section describes planned POD activities during the pre-launch and the post-launch periods.

6.6.1   Pre-Launch POD Activities

During the pre-launch period, POD activities will be focused on the following areas: 1) selection of POD standards, 2) model improvement efforts, 3) preparation for operational POD, and 4) POD accuracy assessment. In this section, pre-launch POD activities in these areas are summarized.

6.6.1.1   Standards

The standard models for the reference system, the force models and the measurement models to be used for the ICESat/GLAS POD are described in Table 6.3. These standards are based on the International Earth Rotation Service (IERS) Conventions [*McCarthy,* 1996], and the T/P standards [*Tapley et al.,* 1994]. These standards will be updated as the models improve, and "best" available models at launch will be selected as the initial standard models.

Table 6.3 Precision Orbit Determination Standards for ICESat/GLAS

Model	ICESat/GLAS Standard	Reference
	Reference Frame	
Conventional inertial system	ICRF	IERS
Precession	1976 IAU	IERS
Nutation	1980 IAU	IERS
Planetary ephemerides	JPL DE-405	Standish [1998]
Polar Motion	IERS	
UT1-TAI	IERS	
Station Coordinates	ITRF	
Plate motion	Nuvel (NNR)	IERS
Reference ellipsoid	a_e = 6378136.3 m	Wakker [1990]
	1/f = 298.257	
	Force Models	
GM	398600.4415 km^3/s^2	Ries et al. [1992a]
Geopotential	JGM-3	Tapley et al. [1996]
	or EGM-96	Lemoine et al. [1996]
	or TEG-4	Tapley et al. [2001]
$\overline{C}_{21}, \overline{S}_{21}$ – mean values	$\overline{C}_{21}$ = -0.187×10⁻⁹	
	$\overline{S}_{21}$ = +1.195×10⁻⁹	
$\overline{C}_{21}, \overline{S}_{21}$ – rates	$\dot{\overline{C}}_{21}$ = -1.3×10⁻¹¹/yr	(see rotational deformation)
	$\dot{\overline{S}}_{21}$ = +1.1×10⁻¹¹/yr	
	epoch 1986.0	
Zonal rates	$\dot{J}_2$ = -2.6×10⁻¹¹/yr	Nerem et al. [1993]
	epoch 1986.0	
N body	JPL DE-405	Standish [1998]
Indirect oblateness	point mass Moon on Earth J_2	
Solid Earth tides		IERS–Wahr [1981]
Frequency independent	k_2 = 0.3, k_3 = 0.093	
Frequency dependent	Wahr's theory	
Ocean tides	CSR TOPEX_3.0	Eanes and Bettadpur [1995]
Rotational deformation	$\Delta\overline{C}_{21} = -1.3\times10^{-9}(x_p - \overline{x}_p)$	Nerem et al. [1994]
	$\Delta\overline{S}_{21} = +1.3\times10^{-9}(y_p - \overline{y}_p)$	
	based on k_2/k_0 = 0.319	
	$\overline{x}_p$ = 0".046, $\overline{y}_p$ = 0".294	
	$\dot{\overline{x}}_p$ = 0".0033/yr	
	$\dot{\overline{y}}_p$ = 0".0026/yr, epoch 1986.0	
Relativity	all geocentric effects	Ries et al. [1991]
Solar radiation	solar constant = 4.560×10⁻⁶ N/m^2 at 1 AU, conical shadow model for Earth and Moon R_e = 6402 km, R_m = 1738 km,	

	R_s = 696,000 km	
Atmospheric drag	density temperature model	Barlier et al. [1977]
	or MSIS90	Hedin [1991]
	or NRLMSISE-00	Hedin et al. [1996]
	daily flux and 3-hour	
	constant k_p,	
	3-hour lag for k_p;	
	1-day lag for $f_{10.7}$,	
	$\bar{f}_{10.7}$ average of previous 81 days	
Earth radiation pressure	Albedo and infrared second-degree	Knocke et al. [1989]
	zonal model, R_e = 6378136.3 m	
Satellite parameters	ICESat/GLAS models	
	Box-wing model	

Measurement Models

Laser range		
Troposphere	Marini & Murray [1973]	IERS
Relativity correction	applied	IERS
Center of Mass/phase center	ICESat/GLAS model	
GPS		
Troposphere	MTT	Herring [1992]
Ionosphere	dual frequency correction	
Center of Mass/phase center	ICESat/GLAS model	
Relativity correction	applied	
Site displacement		
Induced permanent tide	IERS	
Geometric tides		
Frequency independent	$h_2 = 0.6090$,	IERS
	$l_2 = 0.0852$,	
	$\delta = 0°$	
Frequency dependent	K_1 only	IERS
Ocean loading	IERS	
Rotational deformation	$h_2 = 0.6090$, $l_2 = 0.0852$ with	IERS
	$\bar{x}_p = 0".046$, $\bar{y}_p = 0".294$	
	$\dot{\bar{x}}_p = 0".0033/\mathrm{yr}$	
	$\dot{\bar{y}}_p = 0".0026/\mathrm{yr}$, epoch 1986.0	

Figures 2 and 3 show the ground station network for ICESat/GLAS POD for GPS and SLR, respectively. Details of the adopted network may change prior to launch but will remain quite robust. Station coordinates will be adopted from the "best" available ITRF model, expected to be ITRF-99 or ITRF-2000. The ITRF model includes station velocities measured by space geodetic methods.

6.6.1.2   *Gravity Model Improvements*

The gravity model to be used in the immediate post-launch period will be "best" available at launch, such as JGM-3 [*Tapley et al*., 1996], EGM-96 [*Lemoine et al*., 1996], or TEG-4 [*Tapley et al*., 2001]. As further gravity model improvements are made from other projects, such as GRACE, they will be incorporated for ICESat/GLAS POD. At this writing, further study is required for the selection of the at-launch gravity model. However, current state-of-the-art models are sufficiently close that geopotential tuning with ICESat/GLAS data should yield comparable POD performance which is largely unaffected by this initial selection. The "best" available ocean tide model at launch will be adopted as the standard ocean tide model for ICESat/GLAS POD.

6.6.1.3   *Non-Gravitational Model Improvements*

Since the ICESat/GLAS launch coincides with the predicted solar maximum, the atmospheric drag perturbation will be the largest non-gravitational force acting on the satellite. Some drag-related models were evaluated for CHAMP POD, as part of drag model improvement efforts for reducing the effect of drag model errors on ICESat/GLAS POD [*Rim et al*., 2002b]. Those include the thermospheric

wind model, HWM93, NRLMSISE-00 [*Hedin et al.*, 1996], and DTM-2000 [*Bruinsma and Thuillier*, 2000]. Estimation strategies to minimize the effects of drag model errors on POD and gravity tuning will also be investigated.

In order of decreasing magnitude, the remaining non-gravitational perturbations consist of solar radiation pressure, Earth radiation pressure, and on-board thermal emission. For POD, a 'box-wing' model, described in Section 3.4.6, represents the spacecraft as a simple combination of a six-sided box and two attached panels, or 'wings'. This macro-model will use effective specular and diffuse reflectivity coefficients to compute the induced forces acting on each surface. The pre-flight values of these coefficients will be estimated during a tuning process, in which the forces computed with the macro-model are fit to those obtained using a separate micro-model [*Webb*, private communication, 2000]. This latter model employs considerable detail that makes it impractical for use directly in POD. Once ICESat/GLAS is in orbit, the reflectivity coefficients will be adjusted during POD, using the GPS tracking data.

The macro-model tuning effort will compute the radiation from various sources incident on the satellite's surfaces. By using a comprehensive thermal model, the propagation of this energy throughout the spacecraft will be calculated. The resulting temperature distribution will be evaluated to determine whether any on-board thermal gradients may induce net forces. Any such forces would then be modeled analytically during POD.

The non-gravitational forces acting on each surface due to atmospheric drag, solar radiation pressure, Earth radiation pressure, and thermal emission are

computed individually and then summed to obtain the total non-gravitational force acting on the satellite.

6.6.1.4 Measurement Model Developments

One of the sources of measurement model errors is the multipath effect. Colorado Center for Astrodynamics Research (CCAR) multipath study [*Axelrad et al.*, 1999] indicates that the multipath effect alone results in 1-2 cm radial orbit error, while this effect in the presence of other errors, such as drag and gravitational model errors, results in a few mm error. This study was based on a preliminary design location for the antennas and most of the multipath effect was caused by the solar arrays. It also indicates that the effect becomes even smaller with proper editing scheme, such as blocking certain regions. The capability of screening out GPS measurements from blocked regions was implemented in MSODP1. Strategies for detecting and mitigating the multipath effect on CHAMP POD were investigated [*Yoon et al.*, 2002b], and similar approach will be adopted for ICESat/GLAS POD. The final spacecraft design has the GPS antennas positioned above the solar array and bus star cameras. In this location, there is no expected impingement above the ground plane so multipath will be mitigated.

ICESat/GLAS satellite's center of mass location with respect to a reference point on the spacecraft will be measured in the pre-launch period, and the location of the GPS antenna and the laser reflector will also be measured. GPS antenna phase center variations as a function of azimuth and elevation will be determined in pre-launch testing. Effect of GPS antenna phase center variation on

POD was investigated using CHAMP data [*Yoon et al*., 2002a]. Expenditure of fuel and corresponding changes in center of mass location will be monitored during flight.

6.6.1.5   *Preparation for Operational POD*

To generate the POD products operationally when large volumes of data are required, it is essential to make the POD processing as automatic as possible. The POD processing procedures will be examined end-to-end to identify/update the procedures for possible improvement and to minimize the human intervention, and computational and human resources will be allocated optimally for POD processing. The adopted operational POD processing procedures/scripts will be tested by processing upcoming satellites, such as JASON and CHAMP, during the pre-launch period for further improvement.

6.6.1.6   *Software Comparison*

Since the POD products from different software will be compared for POD validation, it is important to compare different software packages in the pre-launch period to identify model differences and to quantify the level of agreement among different POD software systems, such as UT-CSR's MSODP1, GSFC's GEODYN, and JPL's GOA II.   This comparison becomes easier for the ICESat/GLAS POD due to the extensive POD software comparison activity between UT-CSR and GSFC for Topex POD [*Ries*, 1992b].   Also, Topex-GPS POD experiments between UT-CSR and JPL [*Bertiger et al*., 1994] gave the opportunity for both groups to compare their software systems. This comparison will continue for the ICESat/GLAS POD models to ensure the validity of the POD verification by comparing with POD products from different software systems.

6.6.1.7   POD Accuracy Assessment

During the pre-launch period, simulation studies will continue to assess the POD accuracy. Comparison of highly parameterized dynamic approach and the reduced-dynamic approach will be continued. For the GPS orbit modeling, standard models for GPS orbit determination will be updated as the models progress, and the resulting orbit will be compared to the IGS solutions. Also, the effect of fixing GPS orbits to independently determined ephemerides, such as IGS solutions, on the POD and the gravity tuning will be evaluated.

6.6.2   Post-Launch POD Activities

During the first 30-150 days after launch, which is the Calibration/Validation period, POD processing will tune the model parameters, including the gravity, and define adopted parameter set for processing the first 183-day cycle. During the 183 days of the Cycle 1, the POD processing will assess and possibly further improve or refine parameters, such as assess the gravity field from the gravity mission GRACE, if available, and adopt a new parameter set for the processing of Cycle 2 data. POD processing will continue assessment of POD quality after Cycle 1, and new parameter adoptions should be minimized and timed to occur at cycle boundaries.

6.6.2.1   Verification/Validation Period

During the calibration/validation period, several important POD activities will be undertaken simultaneously. These include tuning model parameters, POD calibration/validation, evaluation of out-gassing effect, evaluation of estimation

strategies and GPS orbit modeling procedure, evaluation of multipath effect and construction of editing scheme.

Some model parameters, such as geopotential parameters and the "box-wing" model parameters, will be tuned using the tracking data. About 30-40 days of GPS data will be processed for gravity tuning, and the arc length will be dictated by the maneuver spacing and the ability of POD to mitigate the effect of the non-gravitational model errors, especially the drag model errors, to certain level. The tuned gravity field will be determined by combining the pre-tune gravity coefficients and the solution covariance with the new information equations from the GPS tracking data.

Internal and external POD calibration/validation activities are planned for POD quality assessment, and those are summarized in the following section.

During the early phase of the mission, the satellite might experience significant out-gassing, and this poses serious challenges for POD. However, this effect will subside as time goes by, and every effort will be made to insure that this effect does not corrupt the parameter tuning process during this validation/verification period.

Estimation strategies described in Section 6.5.4 will be evaluated, and the GPS orbit modeling procedures described in Section 6.5.3 will also be evaluated during this period.

The multipath effect will be evaluated to characterize the extent of signal corruption due to diffraction and reflection using the flight data. Proper editing scheme will be developed if there is any evidence that such an editing reduces the multipath effect on POD.

6.6.2.2   POD Product Validation

To validate the accuracy of ICESat/GLAS POD products, several methods would be employed. For the internal evaluation of the orbit consistency, orbit overlap statistics will be analyzed. Also, the data fit RMS value is an effective indicator of orbit quality. Comparisons between the orbits from different software, such as MSODP1, GEODYN, and GIPSY-OASIS II (GOA II), would serve as a valuable tool to assess the orbit accuracy. Since the ICESat/GLAS will carry the laser reflector on board, the SLR data can be used as an independent data set to determine the ICESat/GLAS orbit. However, this approach assumes reasonably good tracking of the ICESat/GLAS orbit from the SLR stations. Data from the SLR network will also be used to directly evaluate the GPS-determined orbit. Data fits for high elevation SLR passes can be used to evaluate the orbit accuracy of the ICESat/GLAS. The laser altimeter data will be used to assess the validation, however, this assessment can be accomplished only if the calibration and verification of the instrument have been accomplished. Global crossovers from ICESat/GLAS will be used to validate the radial orbit accuracy in a relative sense.

6.6.2.3   POD Reprocessing

To produce improved orbits, reprocessing of data will be performed as often as annually. As the solar activity is expected to decrease in the later mission period, the accuracy of the tuned model parameters will be improved, thereby the POD accuracy will be improved. Any improvement in the model parameters will be adopted for the reprocessing.

6.7   Computational: CPU, Memory and Disk Storage

Table 6.4 compares the computational requirements for processing a typical one-day arc from a 24-ground station network with 30 sec sampling time for both T/P and ICESat/GLAS. These results are based on MSODP1 implemented on the Cray J90 and the HP-735/125.

Current computational plans are to use the HP-class workstation environment for preprocessing GPS data, including generation of double difference files. POD processing will be performed on a Cray J90, or equivalent. This processing on the Cray enables a more efficient resource sharing with other project, such as GRACE.

Table 6.4 Computational Requirements for T/P and ICESat/GLAS POD using MSODP1: One-day Arcs with 24 Ground Stations

Platform	Satellite	CPU (min)	Memory (Mw)	Disk[*] (Mb)
Cray J90	T/P	20	2	35
	ICESat/GLAS	40	2.5	59
HP-735	T/P	30	2	39
	ICESat/GLAS	105	2.5	63

* This includes all the necessary files.
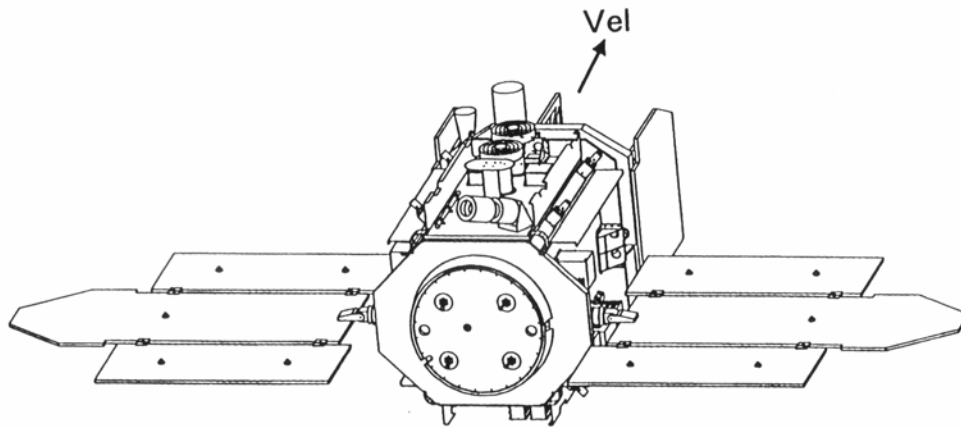
a) "airplane mode" for low β′
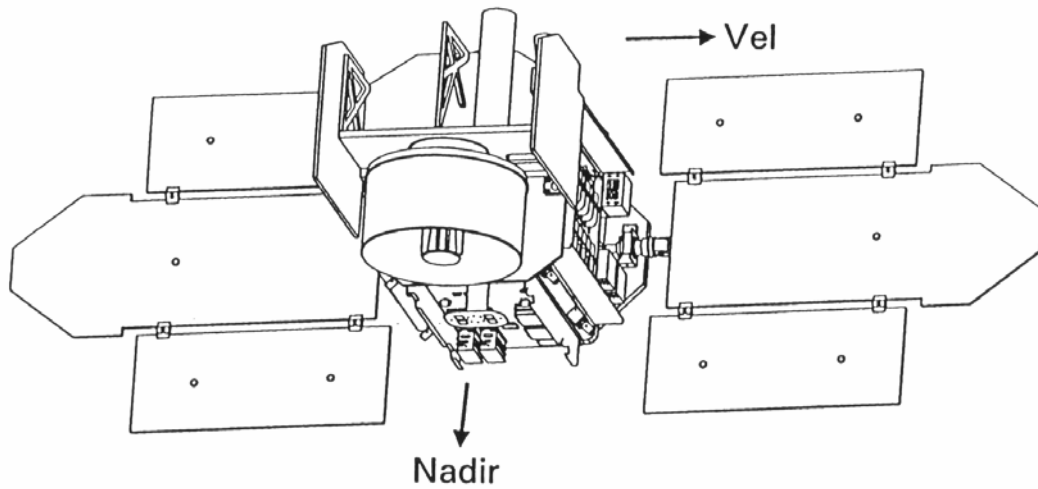
b) "sailboat mode" for high β′

Figure 1. ICESat/GLAS Operational Attitudes
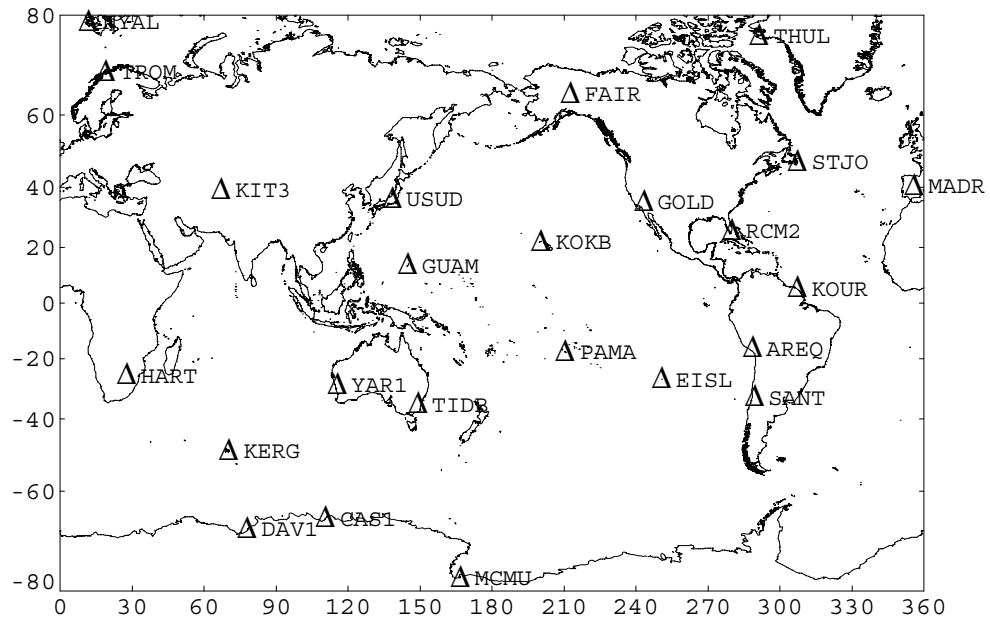
Figure 2. GPS Tracking Stations for ICESat/GLAS POD
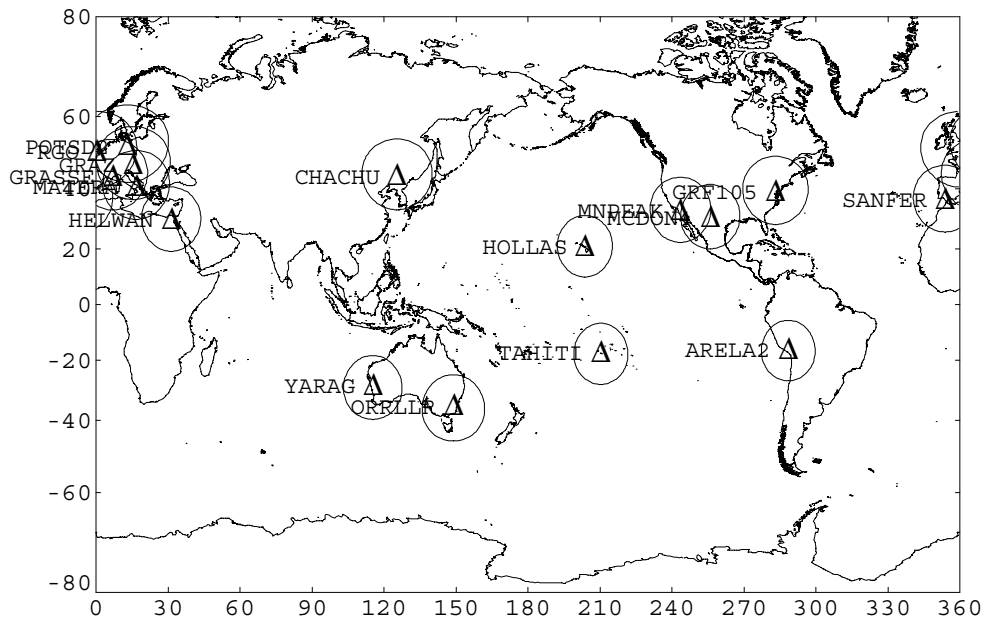
Figure 3. SLR Stations Tracking ICESat/GLAS (20 degree Elevation Masks)

Appendix A: ATBD Update for the Operational ("Final") POD

A.1   ICESat Mission Outline

The Ice, Cloud and land Elevation Satellite (ICESat) was launched on 13 January 2003. The Geoscience Laser Altimeter System (GLAS) instrument onboard ICESat made its first laser elevation measurement of the Earth on 21 February 2003 and its last on 11 October 2009. The three lasers employed by GLAS did not perform as long as expected, and following the failure of Laser 1 on 5 March 2003 the ICESat mission was modified to meet the requirement for capturing a multi-year time series of ice sheet elevations [*Schutz et al.*, 2005]. For the modified mission scenario, the spacecraft entered a 91-day repeat science orbit (compared to a planned 183-day repeat) and the lasers were activated for about 33 days of this 91-day repeat, two or three times per year. This campaign mode operation is summarized in Table A.1, and other significant parameters and events are listed in Table A.2. ICESat laser campaigns are designated by a laser number (L1, L2 or L3), followed by a letter in the sequence of operation. Following campaign L2f, attempts to restart any of the lasers were not successful. The spacecraft was put through a series of engineering tests in early 2010. De-orbit maneuvers were carried out in June and July 2010. The spacecraft was "passivated" on 14 August and reentered the Earth's atmosphere on 30 August 2010 over the Barents Sea northeast of Norway.

Table A.1: ICESat Laser Operation Campaigns

Campaign	Year	Day of year	Calendar Dates	Number of days (d)	Repeat orbit (d)	Repeat tracks[1]
L1a	2003	051-088	20 Feb-29 Mar	37	8	001-072 to 006-023
L2a	2003	268-277/ 277-322	25 Sep-4 Oct/ 4 Oct-18 Nov	54	8/ 91	028-088 to 029-100/ 1098 to 0421
L2b	2004	048-081	17 Feb-21 Mar	33	91	1284 to 0421
L2c	2004	139-173	18 May-21 Jun	34	91	1283 to 0434
L3a	2004	277-313	3 Oct-8 Nov	37	91	1273 to 0452
L3b	2005	048-083	17 Feb-24 Mar	35	91	1258 to 0426
L3c	2005	140-174	20 May-23 Jun	34	91	1275 to 0421
L3d	2005	294-328	21 Oct-24 Nov	34	91	1282 to 0421
L3e	2006	053-087	22 Feb-28 Mar	34	91	1283 to 0424
L3f	2006	144-177	24 May-26 Jun	33	91	1283 to 0421
L3g	2006	298-331	25 Oct-27 Nov	33	91	1283 to 0423
L3h	2007	071-104	12 Mar-14 Apr	33	91	1279 to 0426
L3i	2007	275-309	2 Oct-5 Nov	34	91	1280 to 0421
L3j	2008	048-081	17 Feb-21 Mar	33	91	1282 to 0422
L3k	2008	278-293	4 Oct-19 Oct	15	91	1283 to 0145
L2d	2008	330-352	25 Nov-17 Dec	22	91	0096 to 0423
L2e	2009	068-101	9 Mar-11 Apr	33	91	1286 to 0424
L2f	2009	273-284	30 Sep-11 Oct	11	91	1280 to 0084

[1] There are 119 tracks in the 8-day orbit and 1354 tracks in the 91-day orbit. Cycle numbers are included for the 8-day repeat periods.

Table A.2: Significant ICESat Parameters and Events by Campaign

Cam-paign	Year	Day of year	S/C orient-ation[1]	Start Beta' Angle (°)	End Beta' Angle (°)	Start Laser Infrared Energy (mJ)	End Laser Infrared Energy (mJ)	Mean footprint major axis (m)	Day of year – comments
-	2003	013	-	-	-	-	-	-	013 – launch
L1a	2003	051-088	-Y/+X	-45	-32	72	51	149	080 – yaw flip 085 – safe hold, adjust temperature
L2a	2003	268-277/ 277-322	+Y	51	69	80	55	100	277 – orbit change 286 – laser temperature anomaly 287, 302 – adjust temperature 311 – GPS solar flare anomaly
L2b	2004	048-081	+Y	54	40	57	33	90	
L2c	2004	139-173	-X	13	-4	33	5	88	142-147 – adjust temperature
L3a	2004	277-313	-Y	-48	-58	67	62	56	293 – adjust temperature
L3b	2005	048-083	-Y	-56	-45	68	54	80	054 – suspected amplifier bar drop, begin footprint anomaly[2] 068 – suspected amplifier bar drop
L3c	2005	140-174	+X	-20	-4	49	44	55	
L3d	2005	294-328	+Y	51	63	43	39	52	
L3e	2006	053-087	+Y	62	48	38	30	52	
L3f	2006	144-177	-X	20	4	30	30	51	149 - Energy jump up 2mJ
L3g	2006	298-331	-Y	-44	-54	30	24	53	310 – begin ITRF 2005
L3h	2007	071-104	-Y	-60	-47	24	21	56	
L3i	2007	275-309	+Y	32	46	22	20	57	
L3j	2008	048-081	+Y	74	62	20	16	59	
L3k	2008	278-293	+X	-28	-32	18	12	52	289 – Energy drop 4 mJ
L2d	2008	330-352	-Y	-45	-53	8	4	-	343-344 – adjust temperature, energy up 5 mJ
L2e	2009	068-101	-Y	-71	-59	6	2	-	094-095 – adjust temperature
L2f	2009	273-284	-X	20	25	4	2	-	
-	2010	242	-	-	-	-	-	-	242 – reentry

[1] The spacecraft is said to be in "Sailboat" mode for ±Y orientations and in "Airplane" mode for ±X orientations, where the direction indicates the solar panel orientation with respect to the spacecraft velocity using the GLAS coordinate frame.

[2] The footprint diameter during L3b changed from a mean of 54 m (day of year 048-053) to 84 m (055-068). The reason for the larger footprint size during the latter part of the campaign is unknown, although a suspected amplifier bar dropout occurs near the event.

A.2   Gravitational Models

It had been shown from pre-launch POD studies [*Rim et al.*, 1996; *Rim et al.*, 1999] that the gravity model error was expected to be the dominant source of ICESat orbit errors. The predicted radial orbit errors at the ICESat orbit based on pre-launch gravity models, such as TEG-4 [*Tapley et al.*, 2000] and EGM-96 [*Lemoine et al.*, 1996], were 7-15 cm. As a consequence, gravity improvement using ICESat data (gravity tuning) was expected to be required. However, a gravity model from GRACE, GGM01C [*Tapley et al.*, 2004], was made available at ICESat launch, and the predicted radial orbit errors at the ICESat orbit was significantly reduced to 1.1 cm from this field. Since the gravity model error is no longer the dominant source of ICESat orbit error, the planned gravity tuning was not carried out. Note that GGM01C has been used for ICESat POD throughout the ICESat mission for the consistency of the POD products. Also note that CSR TOPEX_4.0 [*Eanes and Bettadpur*, 1995] was selected as the ocean tide model.

A.3   Macro Model Development

There has been a substantial effort to develop solar and Earth radiation pressure models for ICESat POD [*Webb et al.*, 2001; *Rim et al.*, 2006]. ICESat macro-model [*Webb*, 2007] is the outcome for this endeavor. The model developed to compute solar and Earth radiation forces for ICESat POD consists of a six-sided box and two flat plates, or wings, representing the body of the satellite and its solar arrays, respectively. Illustrated in Fig. A.1 (a), it is intended to capture the primary large

scale effects of incident radiation on satellite motion, and thus, has been designated

the *macro-model*. This implementation requires knowledge of the specular and

diffuse reflectivities, as well as the area, of each of the external surfaces of the box

and both sides of each wing. Many types of geometric figures with varying materials,

often with significantly different reflective properties, make up each face of the

ICESat. Thus, to ensure that the macro-model adequately approximates the radiation

pressure forces on ICESat, its parameters must effectively integrate the contributions

from these disparate surfaces.
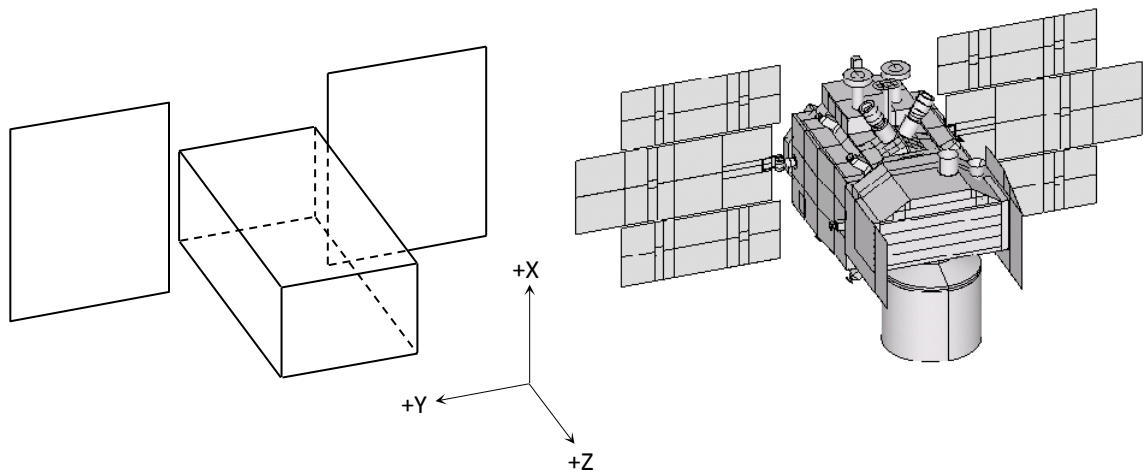
**Figure A.1. ICESat macro-model (a) and micro-model (b), with their common,
body-fixed coordinate frame**

Adapting and extending the approach developed for the TOPEX/Poseidon

mission [*Antreasian and Rosborough*, 1992; *Marshall and Luthcke*, 1992], the forces

induced by solar, Earth albedo and Earth infrared radiation were simulated prior to

the launch of ICESat, using a detailed model of the satellite, shown in Fig. A.1 (b).

Ball Aerospace originally developed this *micro-model* with the Thermal Synthesizer System (TSS) for its thermal analyses of the satellite bus. It consists of 950 surfaces, including flat plates, cones and cylinders. Many of these are further subdivided, yielding 1124 nodes that can receive external radiation. As designed, the TSS software computes the incident and absorbed heat rates at each of these nodes using a sophisticated Monte Carlo Ray Tracing method. In consultation with the Center for Space Research, at the University of Texas at Austin, the TSS vendor, Space Design, Inc., implemented a series of modifications to employ a similar technique in the determination of radiation pressure forces [*Webb et al.*, 2001].

Using this enhanced software, the radiation forces acting at each node in the micro-model were computed at discrete points around the orbit. Once summed to obtain the net force components in the satellite body-fixed frame, they were rotated to an orbit coordinate system and expressed in radial, transverse, and normal (RTN) components. Generated at β' angles every 5° between −90° and +90°, these single-revolution force histories collectively constituted a set of "truth" observations spanning the various orbit-Sun geometries and satellite orientations expected throughout the mission. These data were then fit using a least-squares (LSEI) method [*Hanson and Haskell*, 1982] to find the best set of macro-model parameters for ICESat POD. This particular approach incorporated linear equality and inequality constraints to avoid physically unrealistic estimates. To ensure that no errors would inadvertently be introduced, the orbit, attitude, coordinate-transformation and Sun-position data were read from files output during the micro-model simulation. The

results, which were adopted for POD use during the mission, are shown in Table A.3. Note that the coordinate set (X, Y, Z) in Table A.3 is the Satellite Body-Fixed Coordinate System (SBCS), where X-axis is in the zenith direction and Y-axis is along the solar panel axis. The origin of SBCS is on the center longitudinal axis and 8″ above separation plane. Note also that YSA stands for Solar Array axis of rotation, which is in Y-direction in SBCS.

Table A.3. ICESat Macro-Model Parameters

Macro-Model Face	Surface Area (m^2)	Specular Reflectivity	Diffuse Reflectivity
+X	3.82	0.491	0.000
−X	3.82	0.951	0.000
+Y	5.21	0.426	0.000
−Y	5.21	0.413	0.000
+Z	2.73	0.345	0.170
−Z	2.73	0.736	0.000
+YSA (front)	4.21	0.258	0.000
+YSA (back)	4.21	0.557	0.000
−YSA (front)	4.21	0.258	0.000
−YSA (back)	4.21	0.557	0.000

A.4   GPS antennae and Laser Retro-reflector Array (LRA) location measurement

In the pre-launch period, Ball Aerospace & Technologies Corporation, which built the ICESat spacecraft Bus, measured the location of GPS antennae and LRA [*Iacometti*, 2002]. In Table A.4 the measured locations of GPS antennae are listed. Note that the measured GPS antenna location is the center of choke ring outboard surface. The computed LRA phase center location is also given in the Table A.4.

Note that additional 4.5 cm LRA correction should be applied when SLR data is processed to model LRA phase center location [*Ries,* 2003].

Table A.4. Pre-launch Measurements for GPS Antennae and LRA in Spacecraft Body-Fixed Coordinate System

	X	Y	Z
FM-1 Antenna Reference Point	1.313	0.189	0.586
FM-2 Antenna Reference Point	1.313	-0.189	0.586
LRA	-0.99247	0.0	1.273

All units m

Satellite mass and the location of the Center of Mass (CoM) are changing after each maneuver, and Table A.5 lists the orbit maintenance maneuvers and the mass and the location of CoM during ICESat campaigns.

A.5 Estimated Parameters

Estimated parameters in orbit determination process include ICESat state at the arc epoch, drag scaling parameters (C_D) for every orbital revolution, sinusoidal along-track (AT) and cross-track (CT) forces with a period equal to the orbital period (i.e., one cycle per revolution or 1-cpr) for every orbital revolution, double-differenced ambiguity parameters, piecewise constant zenith delay parameters for every 2.5-hours for ground stations, and the radial-component of center-of-mass offset correction parameter for the operating ICESat GPS antenna.

Table A.5. Orbit Maintenance Maneuvers, Center of Mass Location, and Satellite Mass

Camp-aign	Maneu-ver #	Time (mm/dd/yy hh:mm:sec)	ΔV (m/s)	Δa* (m)	Center of Mass (m)			Mass (kg)
					X	Y	Z	
L1a	–	–	–	–	0.052	0.004	0.984	951.827
	3	02/27/03 17:34:45.2682	0.043901	80.9249	0.052	0.004	0.985	951.807
	4	03/05/03 17:47:33.2300	0.064421	118.7504	0.052	0.004	0.985	951.778
	5	03/14/03 15:17:22.1124	0.071190	131.2296	0.052	0.004	0.985	951.746
	6	03/22/03 23:53:55.3704	0.047863	88.2284	0.052	0.004	0.985	951.724
L2a	–	–	–	–	0.052	0.004	0.987	948.567
	32	09/26/03 13:04:59.2871	0.041459	-76.4243	0.052	0.004	0.987	948.595
	33	10/04/03 12:25:34.3384	0.337591	-622.3018	0.052	0.004	0.987	948.447
	34	10/04/03 13:13:54.5188	0.337591	-622.3018	0.052	0.004	0.987	948.299
	35	10/07/03 03:39:09.7195	0.020607	-37.9862	0.052	0.004	0.988	948.279
	36	10/19/03 01:34:50.7209	0.051738	95.3720	0.052	0.004	0.988	948.240
	37	10/25/03 21:04:55.1758	0.047051	86.7315	0.052	0.004	0.988	948.299
	38	11/01/03 03:41:55.5413	0.103132	190.1093	0.052	0.004	0.988	948.295
	39	11/04/03 00:09:35.5138	0.028300	-52.1671	0.052	0.004	0.988	948.220
	40	11/11/03 02:06:22.3126	0.048364	89.1530	0.052	0.004	0.988	948.220
L2b	–	–	–	–	0.052	0.004	0.988	946.804
	51	02/28/04 23:54:15.3933	0.043696	80.5466	0.052	0.004	0.989	946.739
	52	03/12/04 20:23:05.6900	0.040266	74.2252	0.052	0.004	0.988	946.949
L2c	–	–	–	–	0.052	0.004	0.989	946.633
	59	05/28/04 09:34:17.3027	0.037728	69.5455	0.052	0.004	0.989	946.586
	60	06/10/04 06:03:11.2784	0.037603	69.3159	0.052	0.004	0.988	946.692
L3a	–	–	–	–	0.052	0.004	0.989	945.335
	74	10/12/04 05:37:53.5177	0.032631	60.1504	0.052	0.004	0.990	945.307
	75	10/27/04 20:57:43.0406	0.038153	70.3305	0.052	0.004	0.989	945.398
L3b	–	–	–	–	0.052	0.004	0.990	944.688
	88	02/21/05 07:30:17.4819	0.049142	90.5856	0.052	0.004	0.990	944.668
	89	03/14/05 23:48:47.4269	0.041237	76.0145	0.052	0.004	0.990	944.656
L3c	–	–	–	–	0.052	0.004	0.990	943.805
	96	06/05/05 13:10:18.6167	0.041758	76.9753	0.052	0.004	0.991	943.795
	97	06/20/05 10:47:00.5638	0.027876	51.3854	0.052	0.004	0.990	943.916
L3d	–	–	–	–	0.053	0.004	0.992	941.544
	111	10/24/05 07:45:57.6404	0.026643	49.1131	0.053	0.004	0.992	941.911
	112	11/12/05 18:54:55.8686	0.022183	40.8917	0.053	0.004	0.992	941.977
L3e	–	–	–	–	0.053	0.004	0.993	941.304
	120	03/12/06 03:50:43.5721	0.027713	51.0846	0.053	0.004	0.992	941.286
L3f	–	–	–	–	0.053	0.004	0.993	940.718
	125	06/07/06 21:14:28.2302	0.025539	47.0767	0.053	0.004	0.993	940.749
L3g	–	–	–	–	0.053	0.004	0.994	939.549
	135	11/17/06 19:25:04.9200	0.023362	43.0647	0.053	0.004	0.994	939.602
L3h	–	–	–	–	0.053	0.004	0.994	938.769
	143	03/23/07 15:28:55.9619	0.013268	24.4579	0.053	0.004	0.994	938.915
	144	04/08/07 06:48:46.7778	0.021437	39.5160	0.053	0.004	0.994	938.698
L3i	no maneuvers				0.053	0.004	0.995	937.674
L3j	–	–	–	–	0.053	0.004	0.996	936.567
	166	03/05/08 04:34:33.7579	0.017996	33.1731	0.053	0.004	0.996	936.547
L3k	no maneuvers				0.053	0.004	0.996	936.179
L2d	–	–	–	–	0.053	0.004	0.998	933.910
	181	12/14/08 07:44:48.9590	0.016426	30.2791	0.053	0.004	0.997	935.022
L2e	–	–	–	–	0.053	0.004	0.998	934.104
	188	03/24/09 12:54:57.8440	0.013900	25.6219	0.053	0.004	0.998	934.361
L2f	–	–	–	–	0.053	0.004	0.999	932.724
	198	10/05/09 21:29:10.0982	0.017056	31.4396	0.053	0.004	0.999	933.012

* change in the semi-major axis

A.6   POD Processing Strategy

It was suggested in the POD ATBD (version 2.2) that the reduced dynamic solutions will be investigated as a validation tool for the highly parameterized dynamic solutions. However, no reduced dynamic solutions were generated and compared with the dynamic solutions during ICESat mission. Results of *Davis* [1996] and *Rim et al*. [2000a] show that both highly parameterized dynamic approach with gravity tuning and the reduced-dynamic approach yield comparable results in high fidelity simulations. With the GGM01C field and favorable solar activities throughout ICESat mission, except in 2003, it is expected that the two approaches would generate comparable results.

The GPS orbits were fixed to IGS orbits, and station coordinates were fixed to ITRF2000 solutions [*Altamimi et al*., 2002] up to L3f campaign, and to ITRF2005 solutions [*Altamimi et al*., 2007] starting with the L3g campaign. Note that the IGS switched from ITRF2000 to ITRF2005 during the L3g campaign (Nov 05, 2006) to generate the GPS orbits. ICESat attitude was modeled by PAD solutions, and the on-board solar array orientation information was used.

A.7   POD Accuracy Assessment

A common method for evaluating the POD precision is to compare ephemerides that are adjacent in time and overlap. For ICESat POD, a 30-hour arc is processed, where the middle 24-hour portion is the daily POD product and the additional 6-hours overlaps with the independently determined adjacent arcs before

and after the 24-hour product. Orbit comparison in the overlapping region provides a measure of precision. Such a measure is somewhat representative of internal precision, but it also is indicative of orbit accuracy, although it usually provides an optimistic estimate. Table A.6 summarizes the mean double-differenced RMS for both Rapid and Final POD solutions. The double-differenced RMS for all solutions is about 1 cm.

Table A.6. Mean DD-RMS

Campaign	Rapid POD	Final POD
L1a	1.03	1.01
L2a	1.07	1.02
L2b	1.04	1.01
L2c	1.06	1.04
L3a	1.00	1.00
L3b	1.01	1.00
L3c	1.02	1.01
L3d	1.03	1.02
L3e	1.01	1.01
L3f	1.07	1.07
L3g	1.02	1.02
L3h	1.04	1.03
L3i	1.04	1.03
L3j	1.01	1.01
L3k	1.02	1.01
L2d	1.05	1.05
L2e	1.06	1.05
L2f	1.10	1.10
Mean	1.04	1.03

All units cm

Table A.7 shows the mean orbit overlap statistics for each campaign. The mean of the mean radial orbit overlap for all campaigns is less than 7 mm for both Rapid and Final POD solutions, and the mean of 3D RSS (3-Dimensional Root Sum

Square) is less than 1.4 cm. Note that there is slight improvement in the DD-RMS and

orbit overlaps in the Final solutions comparing with the Rapid solutions.

Table A.7. Mean Overlap Statistics

Campaign	Rapid POD				Final POD			
	R	T	N	3D RSS	R	T	N	3D RSS
L1a	0.70	1.16	0.73	1.56	0.63	1.03	0.68	1.42
L2a	0.82	1.26	0.75	1.72	0.79	1.36	0.67	1.77
L2b	0.80	1.27	0.80	1.74	0.71	1.01	0.69	1.46
L2c	0.71	1.08	0.72	1.50	0.63	1.01	0.70	1.41
L3a	0.68	1.06	0.69	1.47	0.63	1.02	0.69	1.41
L3b	0.60	0.96	0.81	1.42	0.54	0.89	0.76	1.32
L3c	0.74	0.94	0.49	1.32	0.74	0.94	0.48	1.32
L3d	0.60	0.96	0.56	1.28	0.59	0.96	0.57	1.29
L3e	0.59	0.93	0.54	1.24	0.59	0.89	0.54	1.21
L3f	0.67	1.16	0.77	1.57	0.66	1.11	0.78	1.53
L3g	0.52	0.82	0.60	1.16	0.53	0.85	0.60	1.19
L3h	0.56	0.88	0.69	1.28	0.55	0.88	0.73	1.29
L3i	0.66	0.93	0.55	1.29	0.64	0.90	0.54	1.24
L3j	0.51	0.87	0.61	1.20	0.51	0.87	0.62	1.22
L3k	0.52	0.75	0.44	1.04	0.51	0.73	0.45	1.03
L2d	0.64	0.97	0.55	1.31	0.61	0.95	0.56	1.28
L2e	0.66	1.03	0.67	1.41	0.63	0.97	0.64	1.35
L2f	0.57	1.10	0.54	1.38	0.58	1.10	0.51	1.36
Mean	0.64	1.01	0.64	1.38	0.62	0.97	0.62	1.34

All units cm

The ground-based laser ranging measurements provide an independent tool to

assess the accuracy of ICESat POD. By withholding the SLR data from the POD

solution, range residuals can be formed using the adopted tracking station coordinates

and the GPS-determined ICESat ephemeris. Ten SLR stations participate in the

ranging to ICESat: Zimmerwald, McDonald Observatory, Yarragadee, Greenbelt,

Monument Peak, Haleakala, Graz, Herstmonceux, Arequipa, and Hartebeesthoek. To

assure the safety of the detector in the GLAS instrument, a 70-degree maximum elevation pointing restriction has been imposed on those ground stations participating in the ranging. This prevents ground based lasers from sending laser radiation into the GLAS telescope, which could potentially damage the laser detector used by GLAS.

SLR residuals reflect not only the radial component of orbit errors, but also the horizontal component. Usually, the high elevation residuals represent more of the radial component of the orbit accuracy, but unfortunately, there was no tracking over 70-degree due to the restriction mentioned above. To quantify the contribution of the radial orbit errors to the SLR residuals, a "radial" RMS was calculated based on the tracking geometry. Also, high elevation residuals are computed using SLR data above 60 degree elevation. Note that ITRF-2005 SLR station coordinates were used for this analysis.

Table A.8 summarizes the SLR residual statistics for the Final POD. Note that the tracking from the participating stations was increased substantially as the ICESat mission progresses, and average of 6.6 passes were tracked per day for L3f through L3i campaigns. The overall RMS was 1.90 cm. The "radial" RMS was 1.19 cm, and the high elevation (above 60 degree) RMS was 1.65 cm.

Table A.9 summarizes the SLR residual statistics by the tracking stations for the Final POD. Zimmerwald tracks with two laser frequencies, one for infrared (I), and the other for violet (V). Yarragadee has the best tracking with 555 passes total. Hartebeesthoek generated the highest RMS of about 3.7 cm. Haleakala and

Yarragadee performed the best with RMS of about 1.6 cm, and the "radial" RMS of about 1 cm. Among all stations which have more than 100 passes of tracking, Yarragadee performed the best with 1.58 cm RMS and 0.97 cm "radial" RMS.

Table A.8. ICESat SLR Residuals for Final POD

Campaign	Pass #	Data #	RMS	Range Bias	Radial	RMS (data #) > 60°	Range Bias > 60°
L1a	22	330	1.43	1.01	0.87	n/a	n/a
L2a	8	272	1.78	1.03	1.35	1.82(10)	0.53
L2b	3	37	1.76	0.22	0.95	n/a	n/a
L2c	23	250	1.62	0.96	1.03	1.32(2)	n/a
L3a	6	48	1.29	0.78	0.80	n/a	n/a
L3b	37	999	1.68	0.97	0.99	1.50(13)	0.76
L3c	68	1860	2.02	0.90	1.26	1.52(51)	1.16
L3d	191	6278	1.84	1.06	1.10	1.56(142)	1.43
L3e	85	3146	1.74	1.20	1.08	1.60(65)	1.82
L3f	216	7741	2.07	1.15	1.32	1.75(311)	1.52
L3g	241	8803	2.27	1.08	1.43	1.88(346)	1.52
L3h	222	8561	1.69	0.89	1.06	1.45(304)	1.38
L3i	235	8270	1.83	1.01	1.13	1.42(267)	1.09
L3j	115	5103	1.77	1.05	1.12	1.57(225)	1.37
L3k	99	3813	1.38	1.01	0.89	1.48(127)	1.44
L2d	86	3308	2.09	1.21	1.31	2.09(113)	1.71
L2e	178	7113	2.00	1.16	1.22	1.58(279)	1.40
L2f	53	2290	1.72	1.19	1.07	1.94(54)	1.66
Total	1888	68222	1.90	1.09	1.19	1.65(2309)	1.46

All units cm

Table A.9. ICESat SLR Residuals by Stations for Final POD

Station	Pass #	Data #	RMS	Range Bias	Radial	RMS (data #) > 60°	Range Bias > 60°
Zimmerwald-I	205	5612	2.33	1.14	1.47	1.97(187)	1.19
Zimmerwald-V	253	8181	2.01	0.89	1.25	1.47(261)	1.14
McDonald	86	1147	2.08	1.60	1.23	n/a	n/a
McDonald2	17	316	2.98	2.15	1.70	n/a	n/a
Yarragadee	555	24847	1.58	1.07	0.97	1.62(697)	1.49
Greenbelt	134	5629	1.88	1.21	1.08	1.76(111)	1.27
Monument Peak	144	5072	1.76	1.20	1.15	1.71(213)	1.14
Haleakala	27	916	1.58	1.23	1.02	2.64(6)	0.00
Graz	227	9186	1.95	0.88	1.14	1.37(257)	0.94
Herstmonceux	171	5729	2.02	1.05	1.45	1.68(523)	1.38
Arequipa	23	265	1.68	1.15	1.14	2.48(9)	2.58
Hartebeesthoek	46	1322	3.70	0.98	2.32	2.04(45)	1.60
Total	1888	68222	1.90	1.09	1.19	1.65(2309)	1.46

All units cm

Appendix B: 2011 POD Reprocessing

In 2011, GPS data for all the campaign periods during ICESat mission was reprocessed to ensure consistency within ICESat POD products among each campaign period and to reflect POD model advancements since the Final POD standard had been selected. Table B.1 summarizes the changes made for this reprocessing from Final POD.

Table B.1. Changes in 2011 POD Reprocessing

- POD hardware platform and OS:
    - HP Workstation => Workstation with Intel CPU and Linux OS
- POD Fortran compiler:
    - HP Fortran Compiler => Intel Fortran Compiler
- MSODP version:
    - MSODP 2003.1 => MSODP 2009.1 (EPHEVL and ROTATE from 2003.1)
- Reference frame:
    - IGS GPS ephemeris products: IGS final => IGS repro1 (L1 ~ L3i)
    - GPS ground station network: 42 common, 10 deleted, 3 added
    - GPS ground station location: IGS00 => IGS05 (L1 ~ L3f), ITRF2005 => IGS05 (L3g ~ L2f)
    - EOPDAT: EOPDAT_C to EOPDAT_C_05 (L1 ~ L3h)
- Gravitational models:
    - Geopotential field: GGM01C => GGM03C
    - Ocean tide model: CSR TOPEX 4.0 => FES2004
    - Solid Earth tide model: IERS 1996 => IERS 2003
- Observation models:
    - Ground antenna phase center offset: igs_01.pcv => igs05.atx
    - GPS transmitter phase center variation: to igs05.atx
    - Updated GPS yaw table: for L1 ~ L2d
- Estimated parameters:
    - Cross-track COM correction parameter added

B.1 POD Environment

Final POD processing was performed using an HP workstation. Reprocessing was performed on a workstation with Intel CPU and Linux OS. The primary software for POD used in Final POD was MSODP version 2003.1 compiled with HP FORTRAN compiler. In reprocessing, MSODP version 2009.1 compiled with Intel FORTRAN compiler was used.

B.2 Reference Frame

IGS reprocessed all the data prior to 2008 using IGS05 [*Gendt*, 2006], and generated "repro1" products [*Ferland*, 2010], and the reprocessing used these products for L1a through L3i campaigns.

For Final POD, ground station network coordinates information was taken from the file IGS00 [*Weber*, 2001] for L1a through L3f campaigns and from the file ITRF2005 for L3g through L2f campaigns, respectively. In reprocessing, that information for all the campaigns was taken from the file IGS05.

GPS ground station network was updated for reprocessing. Ten stations were deleted and three stations were added to the station network that was used for Final POD. There were 42 common stations between the old and the new station network.

Concerning the Earth orientation file EOPDAT, for campaigns from L1a to L3h, the file EOPDAT_C was used in Final POD. In reprocessing for these campaigns, EOPDAT_C_05, which is consistent with ITRF 2005 reference frame,

was used. For campaigns from L3i to L2f, the file EOPDAT_C_05 was used in Final POD as well as in reprocessing.

B.3   Gravitational Models

Gravity field was updated from GGM01C to GGM03C [*Tapley et al.*, 2007] and ocean tide model was updated from CSR TOPEX_4.0 to FES2004 [*Lyard et al.*, 2006] for the reprocessing. Solid Earth tide model was based on IERS 1996 [*McCarthy (eds.)*, 1996] standard for Final POD, and this model was updated using IERS 2003 [*McCarthy and Petit (eds.)*, 2004] standard for reprocessing. This change was introduced by the MSODP update from version 2003.1 to version 2009.1.

B.4   Observation Models

The ground antenna phase center offset information was taken from the file "igs_01.pcv" for Final POD. In reprocessing, that information was taken from the file "igs05.atx". GPS transmitter phase center variation was not modeled in Final POD, but it was modeled based on "igs05.atx" file for reprocessing.

B.5   Estimated Parameters

In Final POD, the radial component of center-of-mass offset correction parameter for the operating ICESat GPS antenna was estimated once per each estimation arc. In reprocessing, the cross-track component as well as the radial component was estimated once per each estimation arc.

B.6   Reprocessed POD Accuracy Assessment

Table B.2 summarizes the mean orbit differences between the Final POD and the reprocessed POD. Note that there was a period where there was no GPS tracking data due to the orbit event at the end of L1a campaign, and this period was excluded for the orbit comparison. Mean radial differences were about 6 mm, and the mean 3D-RSS differences were about 1.4 cm.

Table B.2. Orbit Difference between Final POD and the reprocessed POD

Campaign	R	T	N	3D-RSS
L1a	0.59	1.26	0.70	1.56
L2a	0.49	1.00	0.64	1.29
L2b	0.55	1.19	0.60	1.45
L2c	0.60	1.24	0.71	1.56
L3a	0.50	1.07	0.62	1.33
L3b	0.61	1.20	0.63	1.49
L3c	0.57	1.25	0.67	1.53
L3d	0.59	1.27	0.65	1.55
L3e	0.58	1.19	0.64	1.47
L3f	0.74	1.43	0.71	1.76
L3g	0.50	0.94	0.64	1.24
L3h	0.57	1.07	0.68	1.39
L3i	0.56	1.22	0.66	1.50
L3j	0.63	1.18	0.63	1.48
L3k	0.50	1.01	0.66	1.31
L2d	0.52	1.03	0.55	1.28
L2e	0.58	1.11	0.56	1.38
L2f	0.49	1.15	0.60	1.39
Mean	0.57	1.16	0.64	1.44

All units cm

Table B.3 compares the mean double-differenced RMS between the Final POD and the reprocessed POD. There was slight improvement in DD RMS for reprocessed POD in sub-millimeter level. Table B.4 compares the mean orbit

overlaps between the Final POD and the reprocessed POD. There was similar improvement in the mean orbit overlaps in sub-millimeter level for the reprocessed POD.

Table B.3. Mean DD-RMS

Campaign	Final POD	2011 Reprocessing
L1a	1.01	1.00
L2a	1.02	1.01
L2b	1.01	0.99
L2c	1.04	1.03
L3a	1.00	0.98
L3b	1.00	0.98
L3c	1.01	1.00
L3d	1.02	1.01
L3e	1.01	0.99
L3f	1.07	1.05
L3g	1.02	0.99
L3h	1.03	1.01
L3i	1.03	1.00
L3j	1.01	0.97
L3k	1.01	0.97
L2d	1.05	1.01
L2e	1.05	1.02
L2f	1.10	1.04
Mean	1.03	1.00

All units cm

Table B.5 summarizes the SLR residual statistics for the reprocessed POD. The overall RMS was 1.75 cm, which is 1.5 mm smaller than the overall RMS for Final POD. The "radial" RMS was 1.09 cm, 1 mm improvement over the Final POD case, and the high elevation (above 60 degree) RMS was 1.58 cm, which is 0.7 mm smaller than the Final POD case.

Table B.6 summarizes the SLR residual statistics by the tracking stations for the reprocessed POD. The overall RMS for the reprocessed POD reduced for all stations, except Haleakala and Hartebeesthoek. Among all stations, Yarragadee performed the best with 1.47 cm RMS and 0.91 cm "radial" RMS.

Table B.4. Mean Overlap Statistics

Campaign	Final POD				2011 Reprocessing			
	R	T	N	3D RSS	R	T	N	3D RSS
L1a	0.63	1.03	0.68	1.42	0.58	0.88	0.56	1.22
L2a	0.79	1.36	0.67	1.77	0.78	1.23	0.57	1.62
L2b	0.71	1.01	0.69	1.46	0.62	0.82	0.48	1.17
L2c	0.63	1.01	0.70	1.41	0.74	1.09	0.65	1.49
L3a	0.63	1.02	0.69	1.41	0.62	0.83	0.53	1.18
L3b	0.54	0.89	0.76	1.32	0.61	0.87	0.65	1.27
L3c	0.74	0.94	0.48	1.32	0.71	0.94	0.40	1.28
L3d	0.59	0.96	0.57	1.29	0.55	0.92	0.49	1.20
L3e	0.59	0.89	0.54	1.21	0.51	0.75	0.41	1.02
L3f	0.66	1.11	0.78	1.53	0.75	1.22	0.66	1.61
L3g	0.53	0.85	0.60	1.19	0.53	0.82	0.58	1.15
L3h	0.55	0.88	0.73	1.29	0.59	0.92	0.67	1.31
L3i	0.64	0.90	0.54	1.24	0.47	0.76	0.50	1.05
L3j	0.51	0.87	0.62	1.22	0.46	0.71	0.53	1.02
L3k	0.51	0.73	0.45	1.03	0.56	0.78	0.37	1.05
L2d	0.61	0.95	0.56	1.28	0.50	0.85	0.50	1.13
L2e	0.63	0.97	0.64	1.35	0.58	0.88	0.56	1.21
L2f	0.58	1.10	0.51	1.36	0.63	1.04	0.41	1.30
Mean	0.62	0.97	0.62	1.34	0.60	0.91	0.54	1.24

All units cm

Table B.5. ICESat SLR Residuals for 2011 Reprocessing POD

Campaign	Pass #	Data #	RMS	Range Bias	Radial	RMS (data #) > 60°	Range Bias > 60°
L1a	22	330	1.31	1.01	0.80	n/a	n/a
L2a	8	272	1.78	1.03	1.11	1.82(10)	0.53
L2b	3	37	2.34	0.22	1.26	n/a	n/a
L2c	23	250	1.57	0.96	1.07	1.32(2)	n/a
L3a	6	48	1.35	0.78	0.85	n/a	n/a
L3b	37	999	1.55	0.97	0.90	1.50(13)	0.76
L3c	68	1860	1.83	0.90	1.13	1.52(51)	1.16
L3d	191	6278	1.66	1.06	1.03	1.56(142)	1.43
L3e	85	3146	1.74	1.20	1.08	1.60(65)	1.82
L3f	216	7741	2.16	1.15	1.37	1.75(311)	1.52
L3g	241	8803	1.91	1.08	1.21	1.88(346)	1.52
L3h	222	8561	1.45	0.89	0.91	1.45(304)	1.38
L3i	235	8270	1.76	1.01	1.09	1.42(267)	1.09
L3j	115	5103	1.72	1.05	1.09	1.57(225)	1.37
L3k	99	3813	1.28	1.01	0.83	1.48(127)	1.44
L2d	86	3308	1.85	1.21	1.16	2.09(113)	1.71
L2e	178	7113	1.73	1.16	1.04	1.58(279)	1.40
L2f	53	2290	1.65	1.19	1.03	1.94(54)	1.66
Total	1888	68222	1.75	1.04	1.09	1.58(2309)	1.40

All units cm

Table B.6. ICESat SLR Residuals by Stations for 2011 Reprocessing POD

Station	Pass #	Data #	RMS	Range Bias	Radial	RMS (data #) > 60°	Range Bias > 60°
Zimmerwald-I	205	5612	2.11	1.10	1.33	1.85(187)	1.23
Zimmerwald-V	253	8181	1.73	0.89	1.08	1.40(261)	1.17
McDonald	86	1147	1.89	1.36	1.12	n/a	n/a
McDonald2	17	316	2.71	1.50	1.55	n/a	n/a
Yarragadee	555	24847	1.47	0.98	0.91	1.64(697)	1.42
Greenbelt	134	5629	1.76	1.04	1.01	1.43(111)	1.05
Monument Peak	144	5072	1.65	1.00	1.08	1.48(213)	0.98
Haleakala	27	916	1.67	1.24	1.07	2.55(6)	0.00
Graz	227	9186	1.82	0.94	1.06	1.36(257)	0.99
Herstmonceux	171	5729	1.70	0.98	1.24	1.61(523)	1.30
Arequipa	23	265	1.48	1.11	1.02	2.56(9)	2.68
Hartebeesthoek	46	1322	3.88	0.80	2.42	1.84(45)	1.14
Total	1888	68222	1.75	1.04	1.09	1.58(2309)	1.40

All units cm

BIBLIOGRAPHY

Altamimi, Z., Sillard, P., and Boucher, C., "ITRF2000: A new release of the International Terrestrial Reference Frame for earth science applications," *J. Geophys. Res.*, 107(B10), 2214, doi:10.1029/2001JB000561, 2002.

Altamimi, Z., Collilieux, X., Legrand, J., Garayt, B., and Boucher, C., "ITRF2005: A new release of the International Terrestrial Reference Frame based on time series of station positions and Earth Orientation Parameters," *J. Geophys. Res.*, 112, B09401, doi:10.1029/2007JB004949, 2007.

Anderle, R. J., Geodetic Analysis Through Numerical Integration, *Proceedings of the International Symposium on the Use of Artificial Satellites for Geodesy and Geodynamics*, Athens, Greece, 1973.

Antreasian, P. G. and G. W. Rosborough, Prediction of Radiant Energy Forces on the TOPEX/POSEIDON Spacecraft, *J. Spacecraft and Rockets*, Vol. 29, No. 1, 81-90, 1992.

Atlshuler, E. E., and P. M. Kalaghan, Tropospheric range error corrections for the NAVSTAR system, Air Force Cambridge Research Laboratories, *AFCRL-TR-74-0198*, April 1974.

Axelrad, P., K. Gold, P. Madhani, ICESat Observatory Multipath Effect, Final Report, Colorado Center for Astrodynamics Research, University of Colorado, March, 1999.

Barlier, F., C. Berger, J. L. Falin, G. Kockarts, and G. Thuiller, A Thermospheric Model Based on Satellite Drag Data, *Aeronomica Acta*, Vol. 185, 1977.

Bertiger, W. I., Y. E. Bar-Sever, E. J. Christensen, E. S. Davis, J. R. Guinn, B. J. Haines, R. W. Ibanez-Meier, J. R. Jee, S. M. Lichten, W. G. Melbourne, R. J. Mullerschoen, T. N. Munson, Y. Vigue, S. C. Wu, T. P. Yunck, B. E. Schutz, P. A. M. Abusali, H. J. Rim, M. M. Watkins, and P. Willis, GPS Precise Tracking of TOPEX/POSEIDON: Results and Implications, *J. Geophys. Res.*, 99, C12, 24449-24464, 1994.

Beutler, G., E. Brockmann, U. Gurtner, L. Hugentobler, L. Mervart, M. Rothacher, and A. Verdun, Extended Orbit Modeling Techniques at the CODE Processing Center of the International GPS Service for Geodynamics (IGS): Theory and the Initial Results, *Manuscripta Geodaetica, 19*, 367-386, 1994.

Bruinsma, S. L., and G. Thuillier, A Revised DTM Atmospheric Density Model: Modeling Strategy and Results, EGS XXV General Assembly, Session G7, Nice, France, 2000.

Byun, S. H., Satellite Orbit Determination Using GPS Carrier Phase in Pure Kinematic Mode, Dissertation, Department of Aerospace Engineering and Engineering Mechanics, The University of Texas at Austin, December, 1998.

Cartwright D. E. and R. J. Tayler, New Computations of the Tide Generating Potential, *Geophys. J. Roy. Astron. Soc.,* Vol. 23, 45-74, 1971.

Cartwright D. E. and A. C. Edden, Corrected Tables of Tidal Harmonics, *Geophys. J. Roy. Astron. Soc.,* Vol. 33, 253-264, 1973.

Cassoto, S., Ocean Tide Models for Topex Precise Orbit Determination, Dissertation, Department of Aerospace Engineering and Engineering Mechanics, The University of Texas at Austin, December 1989.

Chao, C. C., The Tropospheric Calibration Model for Mariner Mars 1971, *Technical Report 32-1587*, 61-76, JPL, Pasadena, California, March, 1974.

Christensen, E. J., B. J. Haines, K. C. McColl, and R. S. Nerem, Observations of Geographically Correlated Orbit Errors for TOPEX/Poseidon Using the Global Positioning System, *Geophys. Res. Let.*, *21(19)*, 2175-2178, Sep. 15, 1994.

Ciufolini, I., Measurement of the Lense-Thirring Drag on High-Altitude Laser-Ranged Artificial Satellites, *Phys. Rev. Let.*, *56*, 278, 1986.

Clynch J. R. and D. S. Coco, Error Characteristics of High Quality Geodetic GPS Measurements: Clocks, Orbits, and Propagation Effects, in *Proceedings of the 4th International Geodetic Symposium on Satellite Positioning*, Austin, Texas, 1986.

Colombo, O. L., Ephemeris Errors of GPS Satellites, *Bull. Geod., 60*, 64-84, 1986.

Colombo, O. L., The Dynamics of Global Positioning System Orbits and the Determination of Precise Ephemerides, *J. Geophys. Res.*, 94, B7, 9167-9182, 1989.

Davis, G. W., GPS-Based Precision Orbit Determination for Low Altitude Geodetic Satellites, *CSR-96-1*, May 1996.

Demarest, P. and B. E. Schutz, Maintenance of the ICESat Exact Repeat Ground Track, *Proc. AAS/AIAA Astrodynamics Specialist Conference*, Paper AAS 99-391, Girdwood, Alaska, August 16-19, 1999.

DeMets, C., R. G. Gordon, D. F. Argus, and S. Stein, Current Plate Motions, *Geophys J. R. Astron. Soc.*, 1990.

Dow, J. M., Ocean Tide and Tectonic Plate Motions from Lageos, Dissertation, Beim Fachbereich 12 - Vermessungswesen, der Technishen Hochshule Darmstadt, Munchen, 1988.

Eanes, R. J., B. E. Schutz, and B. D. Tapley, Earth and Ocean Tide Effects on Lageos and Starlette, *Proceedings of the Ninth International Symposium on Earth Tides* (Ed. J. T. Kuo), 239-249, 1983.

Eanes, R. J. and S. Bettadpur, The CSR 3.0 Global Ocean Tide Model Diurnal and Semi-diurnal Ocean Tides from TOPEX/Poseidon Altimetry, *CSR-TM-95-06*, 1995.

Engelkemier, B. S., Lagrangian Interpolation to an Ordered Table to Generate a Precise Ephemeris, Thesis, The University of Texas at Austin, 1992.

Elyasberg, P., B. Kugaenko, V. Synitsyn, and M. Voiskovsky, Upper Atmosphere Density Determination from the COSMOS Satellite Deceleration Results, *Space Research*, Vol. XII, 1972.

Ferland, Rémi, "Availability of "repro1" products," IGSMAIL-6136, 2010.

Feulner, M. R., The Numerical Integration of Near Earth Satellite Orbits Across SRP Boundaries Using the Method of Modified Back Differences, Thesis, Department of Aerospace Engineering and Engineering Mechanics, The University of Texas at Austin, August 1990.

Finn, A. and J. Matthewman, A Single-Frequency Ionospheric Refraction Correction Algorithm for TRANSIT and GPS, in *Proceedings of the 5th International Geodetic Symposium on Satellite Positioning*, Las Cruces, New Mexico, March 13-17, 1989.

Fliegel H. F., T. E. Gallini, and E. R. Swift, Global Positioning System Radiation Force Model for Geodetic Applications, *J. Geophys. Res.*, *97,* 559-568, 1992.

Gendt, Gerd, "IGS switch to absolute antenna model and ITRF2005," IGSMAIL-5438, 2006.

Gibson, L. R., A Derivation of Relativistic Effect in Satellite Tracking, *Technical Report 83-55*, NSWC, Dahlgren, Virginia, April, 1983.

Goad, C. C. and L. Goodman, A Modified Hopfield Tropospheric Refraction Correction Model, presented at the AGU Fall Meeting, San Francisco, Calif., December 1974.

Goad, C. C., Gravimetric Tidal Loading Computed from Integrated Green's Functions, *J. Geophys. Res.*, *85*, 2679-2683, 1980.

Hanson, R. and Haskell, K., "Algorithm 587: Two Algorithms for the Linearly Constrained Least Squares Problem," ACM Transactions on Mathematical Software, Vol. 8, No. 3, September 1982, pp. 323-333.

Hedin, A. E., Extension of the MSIS Thermosphere and Exosphere with Empirical Temperature Profiles, *J. Geophys. Res.*, 96, 1159-1172, 1991.

Hedin, A. E., E. L. Fleming, A. H. Manson, F. J. Schmidlin, S. K. Avery, R. R. Clark, S. J. Franke, G. J. Fraser, T. Tsuda, F. Vidal, and R. A. Vincent, Empirical Wind Model for the Upper, Middle and Lower Atmosphere, *J. Atmos. Terr. Phys.*, 58, 1421-1447, 1996.

Heiskanen, W. A. and H. Moritz, *Physical Geodesy*, W. H Freeman and Company, London, 1967.

Herring, T. A., B. A. Buffett, P. M. Mathews, and I. I. Shapiro, Forced Nutations of the Earth: Influence of Inner Core Dynamics 3. Very Long Interferometry Data Analysis, *J. Geophys. Res.*, *96*, 8259-8273, 1991.

Herring, T. A., Modeling Atmospheric Delays in the Analysis of Space Geodetic Data, in *Refraction of Transatmospheric Signals in Geodesy*, J. De Munck and T. Spoelstra (ed.), Netherland Geodetic Commission Publications in Geodesy, 36, 157-164, 1992.

Hofmann-Wellenhof, B., H. Lichtenegger, and J. Collins, *GPS Theory and Practice*, Springer-Verlag Wien, New York, 1992.

Holdridge, D. B., An Alternate Expression for Light Time Using General Relativity, *JPL Space Program Summary 37-48*, III, 2-4, 1967.

Huang, C. and J. C. Ries, The Effect of Geodesic Precession in the Non-Inertial Geocentric Frame, *CSR-TM-87-04*, Center for Space Research, The University of Texas at Austin, December, 1987.

Huang, C., J. C. Ries, B. D. Tapley, and M. M. Watkins, Relativistic Effects for Near-Earth Satellite Orbit Determination, *Celestial Mechanics*, Vol. 48, No. 2, 167-185, 1990.

Iacometti, J., ICESat Critical Spatial Information and Tolerance, SER No. 3257-MEC-092, Ball Aerospace & Technologies Corp., 2002.

IGS, International GPS Service for Geodynamics: Resource information, 1998.

Jacchia, L. G., Revised Static Models of the Thermosphere and Exosphere with Empirical Temperature Profiles, *Smith. Astrophys. Obs. Spec. Rep.*, 332, 1971.

Jacchia, L. G., Thermospheric Temperature Density, and Composition: New Models, *Smith. Astrophys. Obs. Spec. Rep.*, 375, 1977.

Kaula, W. M., *Theory of Satellite Geodesy*, Blaisdell, Waltham, Mass., 1966.

Knocke, P. C. and J. C. Ries, Earth Radiation Pressure Effects on Satellites, University of Texas Center for Space Research Technical Memorandum, *CSR-TM-87-01*, September, 1987.

Knocke, P. C., Earth Radiation Pressure Effects on Satellite, Dissertation, Department of Aerospace Engineering and Engineering Mechanics, The University of Texas at Austin, May, 1989.

Kouba, J., Y. Mireault, G. Beutler, T. Springer, and G. Gendt, A Discussion of IGS Solutions and Their Impact on Geodetic and Geophysical Applications, *GPS Solutions*, Vol. 2, No. 2, 3-15, Fall 1998.

Lambeck, K., *The Earth's Variable Rotation: Geophysical Causes and Consequences*, Cambridge University Press, 1980.

Lawson, C. L. and R. J. Hanson, *Solving Least Squares Problems*, Prentice-Hall Inc., Englewood Cliffs, New York, 1974.

Lemoine, F. G., E. C. Pavlis, S. M. Klosko, N. K. Pavlis, J. C. Chan, S. Kenyon, R. Trimmer, R. Salman, R. H. Rapp, and R. S. Nerem, Latest Results from the Joint NASA GSFC and DMA Gravity Model Project, *EOS Transactions, AGU, 77(17)*, p. S41, 1996.

Lieske, J. H., T. Lederle, W. Fricke, and B. Morando, Expressions for the precession quantities based upon the IAU (1976) System of Astronomical Constants, *Astronomy and Astrophysics*, Vol. 58, 1-16, 1977.

Lieske, J. H. Precession matrix based on IAU (1976) system of astronomical constants, *Astronomy and Astrophysics*, Vol. 73, 282-284, 1979.

Lundberg, J. B., Numerical Integration Techniques for Satellite Orbits, Univ. of Texas at Austin, Department of Aerospace Engineering and Engineering Mechanics, *IASOM-TR-81-1*, 1981.

Lundberg, J. B., Computational Errors and their Control in the Determination of Satellite Orbits, Report *CSR-85-3*, The Center for Space Research, The University of Texas at Austin, 1985.

Lyard, F., F. Lefèvre, T. Letellier and O. Francis. Modelling the global ocean tides: a modern insight from FES2004, *Ocean Dynamics*, 56, 394-415, 2006.

Marini, J. W. and C. W. Murray, Correction of Laser Range Tracking Data for Atmospheric Refraction at Elevations above 10 Degrees, *Rep. X-591-73-351*, Goddard Space Flight Center, Greenbelt, Maryland, November 1973.

Marshall, J. A., S. B. Luthcke, P. G. Antreasian, and G. W. Rosborough, Modeling Radiation Forces Acting on TOPEX/Poseidon for Precise Orbit Determination, *NASA Technical Memorandom 104564*, June 1992.

McCarthy J. J. and T. V. Martin, A Computer Efficient Model of Earth Albedo Satellite Effects, NASA Goddard Space Flight Center, Planetary Sciences Department Report No. 012-77, June, 1977.

McCarthy D. D. (Ed.), IERS Conventions (1996), *IERS Tech. Note 21*, Obs. de Paris, July 1996.

McCarthy D. D. and G. Petit (Ed.), IERS Conventions (2003), IERS Technical Note No. 32, Frankfurt am Main: Verlag des Bundesamts für Kartographie und Geodäsie, 2004. 127 pp., paperback, ISBN 3-89888-884-3 (print version).

Melbourne, W. G., E. S. Davis, T. P. Yunck, and B. D. Tapley, The GPS Flight Experiment on TOPEX/Poseidon, *Geophys. Res. Let.*, Vol. 21, No. 19, 2171-2174, Sep. 15, 1994.

Milani, A., Non-Gravitational Perturbations and Satellite Geodesy, Adam Hilger, 1987.

Milliken, R. J. and C. J. Zoller, Principle of Operation of NAVSTAR and System Characteristics, *Navigation*, Vol. 25, 95-106, 1978.

Minster, J. B., and T. H. Jordan, Present Day Plate Motions, *J. Geophys. Res.*, *83*, 5331-5354, 1978.

Moyer, T. D., Transformation from Proper Time on Earth to Coordinate Time in Solar System Barycentric Space-Time Frame of Reference. Part 1 & Part 2, *Celestial Mechanics*, Vol. 23, 33-56, 57-68, 1981.

Nerem, R. S., B. F. Chao, A. Y. Au, J. C. Chan, S. M. Klosko, N. K. Pavlis, and R. G. Williamson, Time Variations of the Earth's Gravitational Field from Satellite Laser Ranging to LAGEOS, *Geophys. Res. Lett., 20(7)*, 595-598, 1993.

Nerem, R. S., F. J. Lerch, J. A. Marshall, E. C. Pavlis, B. H. Putney, B. D. Tapley, R. J. Eanes, J. C. Ries, B. E. Schutz, C. K. Shum, M. M. Watkins, S. M. Klosko, J. C. Chan, S. B. Luthcke, G. B. Patel, N. K. Pavlis, R. G. Williamson, R. H.

Rapp, R. Biancale, and F. Nouel, Gravity Model Development for TOPEX/POSEIDON: Joint Gravity Models 1 and 2, *J. of Geophys. Res., 99*, 24421-24447, 1994.

Remondi, B. W., Using the Global Positioning System (GPS) Phase Observable for Relative Geodesy: Modeling, Processing, and Results, Dissertation, Department of Aerospace Engineering and Engineering Mechanics, The University of Texas at Austin, May, 1984.

Ries, J. C., C. Huang, and M. M. Watkins, Effect of General Relativity on a near-Earth satellite in the geocentric and barycentric reference frames, *Phys. Rev. Lett., 61*, 903, 1988.

Ries, J. C., Simulation of an Experiment to Measure the Lense-Thirring Precession Using a Second Lageos Satellite, Dissertation, Department of Aerospace Engineering and Engineering Mechanics, The University of Texas at Austin, December, 1989.

Ries, J. C., C. Huang, M. M. Watkins, and B. D. Tapley, Orbit Determination in the Relativistic Geocentric Reference Frame, *J. Astron. Sci., 39(2)*, 173-181, 1991.

Ries, J. C., R. J. Eanes, C. K. Shum, and M. M. Watkins, Progress in the Determination of the Gravitational Coefficients of the Earth, *Geophys. Res. Lett., 19(6)*, 529-531, 1992a.

Ries, J. C. and D. Pavlis, TOPEX/POSEIDON Project, Software Intercomparison Results - Phase I and II, The University of Texas Center for Space Research, March 1992b.

Ries, J., Personal communication, 2003.

Rim, H. J., B. E. Schutz, P. A. M. Abusali, and B. D. Tapley, Effect of GPS Orbit Accuracy on GPS-determined TOPEX/Poseidon Orbit, *Proc. ION GPS-95*, 613-617, Palm Springs, California, Sep. 12-15, 1995.

Rim, H. J., G. W. Davis, and B. E. Schutz, Dynamic Orbit Determination for the EOS Laser Altimeter Satellite (EOS ALT/GLAS) Using GPS Measurements, *J. Astron. Sci., 44(3)*, 409-424, 1996.

Rim, H. J., C. Webb, and B. E. Schutz, Analysis of GPS and Satellite Laser Ranging (SLR) Data for ICESat Precision Orbit Determination, *Proc. AAS/AIAA Space Flight Mechanics Meeting*, Paper 99-146, Breckenridge, Colorado, February 7-10, 1999.

Rim, H. J., C. Webb, S. Byun, and B. E. Schutz, Comparison of GPS-Based Precision Orbit Determination Approaches for ICESat, *Proc. AAS/AIAA Space Flight Mechanics Meeting*, Paper AAS-00-114, Clearwater, Florida, Jan. 24-26, 2000a.

Rim, H. J., C. Webb, and B. E. Schutz, Effect of GPS Orbit Errors on ICESat Precision Orbit Determination, *Proc. AIAA/AAS Astrodynamics Specialist Conference*, Paper AIAA-2000-4234, Denver, Colorado, Aug. 14-17, 2000b.

Rim, H. J., S. Yoon, and B. E. Schutz, Effect of GPS Orbit Accuracy on CHAMPPrecision Orbit Determination, AAS/AIAA Space Flight Mechanics Meeting,Paper AAS 02-213, San Antonio, Texas, Jan. 27-30, 2002a.

Rim. H. J., Y. C. Kim, and B. E. Schutz, Atmospheric Drag Modeling for CHAMP Precision Orbit Determination, *Proc. AIAA/AAS Astrodynamics Specialist Conference*, Paper No. 2002-4737, Monterey, CA, Aug. 5-8, 2002b.

Rim, H., Webb, C., Yoon, S., and Schutz, B. E., "Radiaion Pressure Modeling for ICESat Precision Orbit Determination," AIAA/AAS Astrodynamics Specialist Conference, paper AIAA 2006-6666, Keystone, CO, Aug. 21-24, 2006.

Schutz, B. E., and B. D. Tapley, Utopia: University of Texas Orbit Processor, Department of Aerospace Engineering and Engineering Mechanics, The University of Texas at Austin, *TR 80-1*, 1980a.

Schutz, B. E., and B. D. Tapley, Orbit Accuracy Assessment for Seasat, *J. Astron. Sci.,* Vol. XXVIII, No. 4, 371-390, October-December, 1980b.

Schutz, B. E., B. D. Tapley, R. J. Eanes, and M. M. Watkins, Earth Rotation from Lageos Laser Ranging, *Bureau International De L'Heure (BIH) Annual Report,* D51-D56, July, 1988.

Schutz, B. E., B. D. Tapley, P. A. M. Abusali, and H. J. Rim, Dynamic Orbit Determination Using GPS Measurements from TOPEX/Poseidon, *Geophys. Res. Let.*, *21(19),* 2179-2182, Sep. 15, 1994.

Schutz, B.E.; Zwally, H.J.; Shuman, C.A.; Hancock, D.; DiMarzio, J.P. Overview of the ICESat Mission. *Geophysical Research Letters* **2005**, 32, L21S01 (DOI:10.1029/2005GL024009).

Seidelmann, P. K., 1980 IAU Theory of Nutation: The Final Report of the IAU Working Group on Nutation, *Celestial Mechanics*, Vol. 27, 79-106, 1982.

Shum, C. K., J. C. Ries, B. D. Tapley, P. Escudier, and E. Delaye, Atmospheric Drag Model for Precise Orbit Determination, *CSR-86-2*, Center for Space Research, The University of Texas of Austin, 1986.

Spilker, J. J., Jr., GPS Signal Structure and Performance Characteristics, *Navigation*, Vol. 25, 121-146, 1978.

Springer, T. A., G. Beutler and M. Rothacher, A New Solar Radiation Pressure Model for the GPS Satellites, IGS Workshop Proceedings, Darmstadt, Germany, ESOC, 1998.

Standish, E. M., JPL Planetary and Lunar Ephemerides DE405/LE405, *JPL Interoffice Memorandum, IOM 312.F-98-048*, Aug. 26, 1998 (Ephemerides available on CD-ROM).

Stephens G. L., G. G. Campbell, and T. H. Vonder Haar, Earth Radiation Budgets, *J. Geophys. Res.*, *86, C10*, 9739-9760, October, 1981.

Tapley, B. D., Statistical Orbit Determination Theory, *Advances in Dynamical Astronomy*, 396-425, B. D. Tapley and V. Szebehely, Eds., D. Reidel Publ. Co. Holland, 1973.

Tapley, B. D., B. E. Schutz, and R. J. Eanes, Station Coordinates, Baselines and Earth Rotation From Lageos Laser Ranging: 1976-1984, *J. Geophys. Res.*, *90*, 9235-9248, 1985.

Tapley, B. D. and J. C. Ries, Orbit Determination Requirements for TOPEX, *Proc. AAS/AIAA Astrodynamics Specialist Conference*, Paper 87-429, Kalispell, Montana, August 10-13, 1987.

Tapley, B. D., J. C. Ries, G. W. Davis, R. J. Eanes, B. E. Schutz, C. K. Shum, M. M. Watkins, J. A. Marshall, R. S. Nerem, B. H. Putney, S. M. Klosko, S. B. Luthcke, D. Pavlis, R. G. Williamson, and N. P. Zelensky, Precision Orbit Determination for TOPEX/POSEIDON, *J. Geophys. Res., 99*, 24383-24404, 1994.

Tapley, B. D., M. M. Watkins, J. C. Ries, G. W. Davis, R. J. Eanes, S. Poole, H. J. Rim, B. E. Schutz, C. K. Shum, R. S. Nerem, F. J. Lerch, E. C. Pavlis, S. M. Klosko, N. K. Pavlis, and R. G. Williamson, The JGM-3 Gravity Model, *J. Geophys. Res.*, *101(B12)*, 28029-28049, 1996.

Tapley, B. D., Chambers, D. P., Cheng, M. K., Kim, M. C., Poole, S., and Ries, J. C., "The TEG-4 Earth Gravity Model," 25th European Geophysical Society General Assembly, Nice, France, April 25-29, 2000.

Tapley, B. D., S. Bettadpur, D. Chambers, M. Cheng, B. Gunter, Z. Kang, J. Kim, P. Nagel, J. Ries, H. Rim, P. Roesset, and I. Roundhill, Gravity Field Determination from CHAMP Using GPS Tracking and Accelerometer Data:

Initial Results, *EOS Trans. AGU, 82(47)*, Fall Meet. Suppl., Abstract G51A-0236, 2001.

Tapley, B. D., Bettadpur, S., Watkins, M., and Reigber, C., "The gravity recovery and climate experiment: Mission overview and early results," *Geophysical Research Letters*, 31:9607-+, doi:10.1029/2004GL019920, 2004.

Tralli, D. M., T. H. Dixon, and S. A. Stephens, The Effect of Wet Tropospheric Path Delays on Estimation of Geodetic Baselines in the Gulf of California Using the Global Positioning System, *J. Geophys. Res.*, *93*, 6545-6557, 1988.

Wakker, K. F., Report by the subcommittee on intercomparison and merging of geodetic data, *Rep. LR-638*, Delft Univ. of Technol., May 1990.

Watkins, M. M., Tracking Station Coordinates and Their Temporal Evolution as Determined from Laser Ranging to The Lageos Satellite, Dissertation, Department of Aerospace Engineering and Engineering Mechanics, The University of Texas at Austin, May, 1990.

Wahr, J. M., Body Tides on An Elliptical, Rotating Elastic and Oceanless Earth, *Geophys. J. R. Astron. Soc.*, Vol. 64, 677-703, 1981a.

Wahr, J. M., The forced nutations of an elliptical, rotating, elastic, and oceanless earth, *Geophys. J. R. Astron. Soc.*, Vol. 64, 705-727, 1981b.

Webb, C., Rim, H., and Schutz, B. E., "Radiation Force Modeling for ICESat Precision Orbit Determination," *Advances in the Astronautical Sciences*, Vol. 109, 2001, pp. 501-518.

Webb, C., Radiation Force Modeling for ICESat Precision Orbit Determination, PhD Dissertation, Department of Aerospace Engineering and Engineering Mechanics, The University of Texas at Austin, 2007.

Weber, Robert, "Towards ITRF2000," IGSMAIL-3605, 2001.

Wu, S. C., T. P. Yunck and C. L. Thornton, Reduced-Dynamic Technique for Precise Orbit Determination of Low Earth Satellite, *Proc. AAS/AIAA Astrodynamics Specialist Conference*, Paper AAS 87-410, Kalispell, Montana, August, 1987.

Yoon, S., H. Rim, and B. E. Schutz, Effects of On-Board GPS Antenna Phase Center Variations on CHAMP Precision Orbit Determination, AAS/AIAA Space Flight Mechanics Meeting, Paper AAS 02-214, San Antonio, Texas, Jan. 27-30, 2002a.

Yoon, S., H. Rim, B. E. Schutz, Multipath Effect Detection and Mitigation in Precision Orbit Determination, *Proc. AIAA/AAS Astrodynamics Specialist Conference*, Paper No. 2002-4986, Monterey, CA, Aug. 5-8, 2002b.

Yuan, D. N., The Determination and Error Assessment of The Earth's Gravity Field Model, Dissertation, Department of Aerospace Engineering and Engineering Mechanics, The University of Texas at Austin, May, 1991.

Yunck, T. P. and S. C. Wu, Non-Dynamic Decimeter Tracking of Earth Satellites Using the Global Positioning System, Paper AIAA-86-0404, *AIAA 24th Aerospace Sciences Meeting*, Reno, Nevada, January, 1986.

Yunck, T. P., W. I. Bertiger, S. C. Wu, Y. E. Bar-Server, E. J. Christensen, B. J. Haines, S. M. Lichten, R. J. Muellerschoen, Y. Vigue, and P. Willis, First Assessment of GPS-based Reduced Dynamic Orbit Determination on TOPEX/Poseidon, *Geophys. Res. Let.*, *21(7)*, 541-544, April 1, 1994.